FRACTURE OF THERMOSETTING POLYMERS:

EXPERIMENTS AND MODELING

A Senior Scholars Thesis

by

BRAD EVIN BURGESS

Submitted to the Office of Undergraduate Research
Texas A&M University
in partial fulfillment of the requirements for the designation as

UNDERGRADUATE RESEARCH SCHOLAR

April 2009

Major: Aerospace Engineering

FRACTURE OF THERMOSETTING POLYMERS:

EXPERIMENTS AND MODELING

A Senior Scholars Thesis

by

BRAD EVIN BURGESS

Submitted to the Office of Undergraduate Research
Texas A&M University
in partial fulfillment of the requirements for the designation as

UNDERGRADUATE RESEARCH SCHOLAR

Approved by:

Research Advisor: Amine Benzerga
Associate Dean for Undergraduate Research: Robert C. Webb

April 2009

Major: Aerospace Engineering

ABSTRACT

Fracture of Thermosetting Polymers: Experiments and Modeling. (April 2009)

Brad Evin Burgess
Department of Aerospace Engineering
Texas A&M University

Research Advisor: Dr. Amine Benzerga
Department of Aerospace Engineering

Aircraft are becoming extremely complex in the modern age. Fueled by the advent of new technology, a modern plane's makeup and structure are changing considerably. Recently the idea to utilize a greater amount of composite materials in creating the next generation of aircraft has surfaced, creating a demand for detailed analysis of these materials. Specifically, the composite fan blade cases on turbofan engines, which protect the greater structure of the aircraft, have come under scrutiny. The cases consist of a carbon fiber resin matrix. The resin can be any one of a number of epoxies, most germane of which is E862. This resin has the effect of strengthening the overall casing structure, but the full nature of its use has yet to be acquired. This information would drastically improve the overall understanding of the uses and implications of E862 in an aerospace environment. During the summer of 2008, extensive tensile testing was conducted on notched E862 specimens at NASA Glenn Research Center in Cleveland, Ohio. It was discovered that the behavior of E862 in tension and fracture was drastically affected by the temperature of the specimen as well as the presence of thermal aging.

Specifically, the specimens tested at higher temperatures appeared to yield at lower stress levels, and the aged specimens yielded at higher stress levels. While this testing and analysis exposed a number of interesting material parameters and behaviors, more research must be accomplished before a full understanding can be achieved. The specific fracture mechanics of the resin E862 is a major area of research which must still be considered. This research involves SEM analysis of the fracture surfaces of the test specimens as well as advanced modeling of the fracture using Abacus software and FEM analysis. Once completed, this vital research will serve as a basis through which a more thorough understanding of the fan blade case structure can be gained, and therefore a safer, more structurally sound aircraft will be attainable.

DEDICATION

I dedicate this thesis to my parents.

ACKNOWLEDGMENTS

I would like to thank my advisor, Dr. Amine Benzerga, and his graduate student Anthony De Castro for all of their efforts in helping me to succeed in my research and for their continued support as I finish my undergraduate degree at Texas A&M University. I would also like to thank our associates at NASA Glenn for their help in completing the testing necessary for this research, and for their continued experimental and financial support to this project.

NOMENCLATURE

BCC	Blade Containment Case
E862	Resin E862
FEA	Finite Element Analysis
FEM	Finite Element Modeling
GRC	NASA Glenn Research Center
MMC	Metal-Matrix Composite
PMC	Polymer Matrix Composite
r	Current radius of specimen gage section during tensile test
r_0	Initial radius of specimen gage section before tensile test
φ	r_0/r
Epsilon Bar	$\ln(\varphi)$

TABLE OF CONTENTS

Page

LIST OF FIGURES

LIST OF TABLES

CHAPTER I

INTRODUCTION

Of the many safety features offered by all aircraft today, one of the most essential is the turbofan blade containment case (BCC), which surrounds the fan blades of the engine. One challenge in jet engine design is to contain a fan blade thrown from the blade axel within the engine so that any threat to passengers or airframe is eliminated. The structure of the BCC must withstand the blade impact and remain structurally sound during engine shutdown. Made of metal in the past, these life-saving structures have become much more complex. Specifically, new BCC designs are being explored which use advanced polymer matrix composite materials (PMCs). These composites serve as a superior substitute for metal, due to their light weight and unprecedented strength. The specific goal of this research is to experimentally determine the fracture behavior of a resin known as epoxy E862, which is a polymer resin currently explored by NASA researchers, and then model this behavior using FEM.

In the early 1990's, successful computational methodologies for modeling fracture of metal-matrix composites (MMCs) were developed (Llorca et al, 1991; Paley and Aboudi, 1992), mostly driven by aerospace applications. Although PMCs are

---

This thesis follows the style of Journal of Petroleum Science and Engineering.

technologically more important today, little has been done to develop a similar methodology using physics- based polymer models. In Dr. Benzerga's group efforts are underway to develop a new computational methodology for modeling fracture in PMCs. The main departure from existing methodologies is a macromolecular polymer model that accounts for temperature and strain-rate effects (Chowdhury et al., 2008b;Boyce et al, 1988). The polymer model is supplemented by a matrix cracking model (Chowdhury et al., 2008a) and a de-bonding model (Chowdhury et al., 2008c).

The goal of this project is to contribute to the understanding of the fracture behavior and mechanisms in a class of thermosetting polymers used in BCC composites. These polymers are usually toughened or un-toughened epoxies. More specifically, preliminary experiments have been conducted on E862 as part of a previous research experience at NASA Glenn Research Center.

A hypothesis has been formulated and states that fracture of epoxies is strongly dependent upon the hydrostatic stress. This project will test this hypothesis through experimentation and development of a computer simulation model to mimic the fracture process realized experimentally. To achieve this goal the following objectives have been set:

1. Analyze experimental data on round tensile notched bars.
2. Carry out microscopic observations of the fracture surfaces of the specimens.

3. Construct a finite element model of the specimens and simulate their fracture behavior using a macromolecular polymer model supplemented by a fracture model.

Experimental data for an E862 was generated last summer at NASA Glenn Research Center (GRC). The amount of pressure was varied through the notch acuity. The fractography study is important because accurate material parameters cannot be identified without a notion of where fracture initiated. Some fracture surfaces will be observed using SEM technology, which allows for a much higher resolution of rough surfaces. Preliminary imaging has already been performed using a low power microscope.

Testing at NASA Glenn Research Center

The tests conducted at NASA Glenn Research Center utilized a new method for measuring displacement and strain of materials. This new method used a software program known as Aramis, which is described later. All tensile tests were performed on E862 notched bar Resin Specimens, cured at 350 F. See Fig. 1 below for an example of the type of specimens tested. Three different notch radii were tested, at three different displacement rates, at three different temperatures. Each specific test was also performed twice to ensure accuracy. Thermal aging was also taken into account.

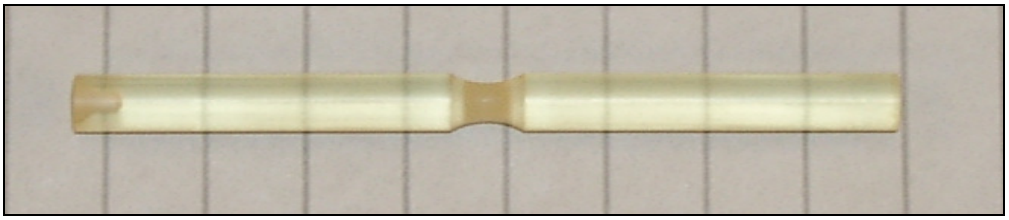

Fig. 1. Example of a generic test specimen used at GRC.

Post processing of data and initial fractography work

Once the testing at GRC was completed the data generated for each test was post processed and plots of stress vs. strain, force vs. displacement, and other important parameters were generated. A low powered microscope was also used to take pictures of the fracture surfaces in order to determine the nature of the majority of the fractures. Fig. 2 and Fig. 3 below demonstrate the two types of fractures that were observed during the testing. Fig. 2 depicts an internal fracture initiation in which failure began within the specimen. This type of initiation is desirable because it indicates that the data obtained for this specimen at fracture is indicative of true material properties. Fig. 3 depicts an external fracture initiation in which failure started on the surface of the specimen. This type of behavior is undesirable because it was most likely caused by a microscopic surface defect and thus the data obtained might not reflect the actual material characteristics.

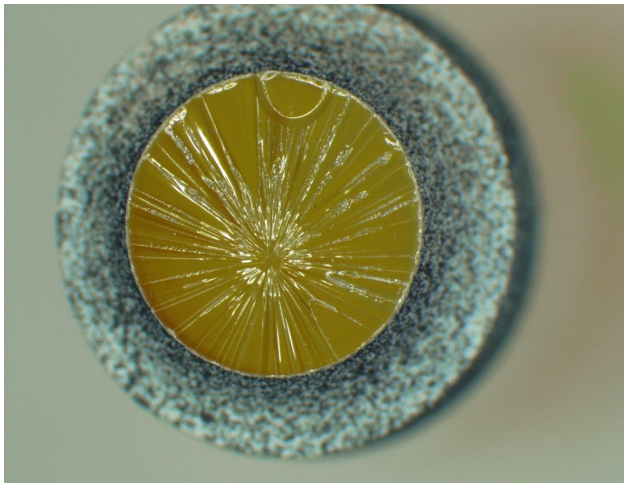

Fig. 2. Example of an internal failure initiation.

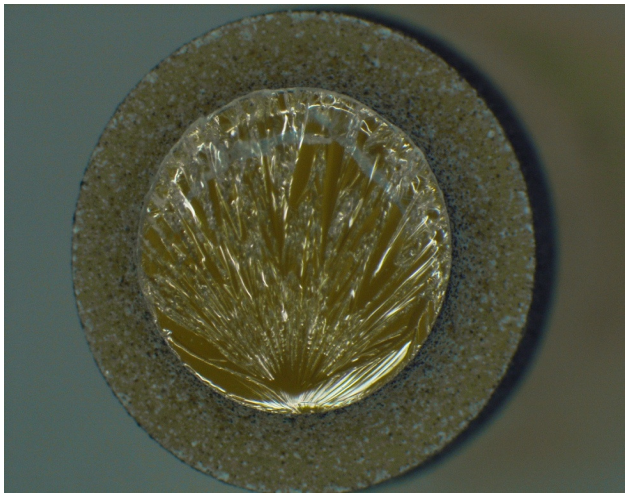

Fig. 3. Example of a surface initiated failure

A detailed description of the tests and analysis performed at GRC can be found in Chapter II.

CHAPTER II

TEST AND ANALYSIS DONE AT GLENN RESEARCH CENTER

At NASA Glenn Research Center during the summer of 2008 the effects of temperature, aging, notch geometry, and displacement rate on E862 were explored, using a special procedure for testing resin specimens. This procedure utilized NASA Glenn's MTS 858 Table Top System and the Aramis Optical Strain Measurement software. These experiments are a vital part of the modeling process. They provide data imperative to analytical models developed to predict impact behavior. The tests conducted using this method were all tensile tests performed on E862 notched bar Resin Specimens, cured at 350 F. Three different notch radii were tested, at three different displacement rates, at three different temperatures. The slow rate tests (1e-5 in/s) were only conducted at room temperature, due to safety considerations. Each specific test was also performed twice to ensure accuracy. Thus 42 tests were completed. However, thermal aging was also taken into account. Another 42 specimens were placed in a thermal aging chamber for 90 min. each day, for an average of 3 days a week over a six month period. Each cycle reached a maximum temperature of 250 F. The specimens were also soaked in a humid atmosphere for which the same schedule was utilized. These specimens were then tested in the same manner, bringing the grand total of tests to 84. See Table 1 below for a detailed description of the different specimen parameters. The test sections of the specimens were all of diameter 0.1535 in. See Appendix A, Fig. A-16, A-17, and A-18 for the specific

geometry of each specimen. First a detailed procedure of the tests performed at room temperature will be given along with post-processing information, followed by a detailed procedure of the tests performed at different temperatures. A presentation and synopsis of the results will follow.

Table 1
Specimen Parameters

Parameter	1	2	3
Notch Radius (in.)	0.0307	0.0614	0.1535
Displacement Rate (in/s.)	1e-1	1e-3	1e-5
Temperature (C)	23	50	80

Testing procedure at room temperature

It was most advantageous to begin by testing the bars of notch radius 0.1535 in., and then tackle the smaller notches, due to the fact that it was not known whether or not Aramis would have to be recalibrated for the smaller notches. Initially the Aramis system was calibrated, a detailed description of which can be found in the Aramis User's Manual (GOM, 2007). Once calibrated, the system was prepared for testing. The first step was to paint the specimen. Aramis is an Optical Strain Measurement program which tracks the movement of small particles on the surface of the test specimen in order to determine strain. A detailed description of the features and setup of Aramis can be found in Littell, etal (Littell et al., 2007). Consequently, this requires that the test specimen be imprinted with some sort of random speckled patter so that strain can be calculated. For this method, basic flat spray paint was used, due to the fact that it performed the best in similar tests. A smooth, thin layer of white paint was then sprayed on the test section of

the specimen, after which the specimens were misted with black spray paint. The specimens now appeared a light shade of gray. It must be stressed that the layers of both paints were thin so that the speckled pattern produced an accurate indication of the material's behavior below. There should be a visible contrast between light and dark on the surface. It was found that if the specimens were held near the top of the spray stream and rotated at a constant rate, optimum results could be obtained, due to the fact that heavier droplets of paint appeared to congregate at the bottom of the spray stream. Fig. 4 shows a properly painted specimen.

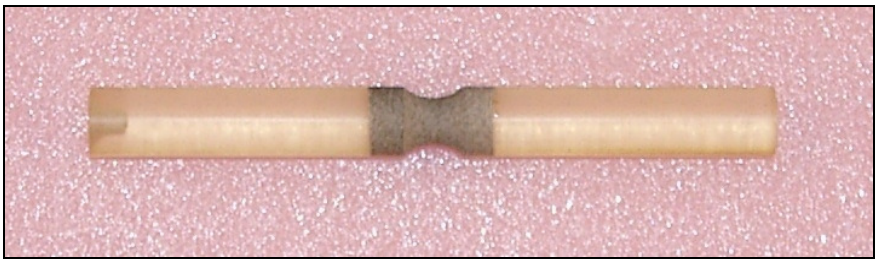

Fig. 4. Properly painted specimen

The next step in this method was the mounting of the specimen in the test apparatus, and the initializing of the Aramis software. This method utilized the 858 Table Top System, a material test apparatus used for tensile, compressive, and shear tests (see Appendix A, Fig. A-12). The computer system that operated the 858 was considered first. A new specimen was defined and the mode of operation was set as displacement, in unlocked configuration. The program "ramp up to failure" was selected, and the displacement rate as well as the data collection rate was input. The end of the specimen was then placed in the bottom grip. The grip pressure was set to approximately 3.8 MPa, an ideal pressure

for the E862 resin specimens. The upper grip was then moved into position using the manual hydraulics controls on the attached computer system. Upon closing the upper grip, the force was auto zeroed using the computer controls, and the mode of operation was then set as Force. The apparatus was then allowed to auto zero itself in Force Mode. See Appendix A, Fig. A-12 and A-13 for a visual description of this setup. While this was taking place, the Aramis system was initialized.

A new project was created in the user directory with the same name as the specimen name given in the 858's computer control, and the system was then set to camera mode. The lighting was checked to ensure that the picture was not overexposed or underexposed, and the shutter time was adjusted as necessary. With the timer disabled, two pictures were taken of the unstrained specimen. These served as the base to which the computer would compare all other configurations. Camera mode was then exited, and a start point for the specimen was set. This was done by zooming in on the specimen and picking a point with good contrast near the middle of the specimen. The point selected on the left image should match that on the right camera image, though it should if calibration was completed successfully. This point was then used by the computer to establish all other points on the speckled surface, thereby forming a virtual 3D model of the specimen. Multiple start points can be selected across the surface to ensure that Aramis "sees" the entire surface. This was done for the smallest notch size (radius of 0.0307) because Aramis would not pick up the area around the notch edges. Once the computer has established the virtual surface, camera mode was brought up again, and the

timer was enabled. The Aramis collection rate was then established. The collection rate depended solely upon the displacement rate. Table 2 below shows all of the collection rates used in this method. See Appendix A, Fig. A-11 for a visual description of the Aramis setup. Aramis was now ready to begin the test.

Table 2
Aramis Collection Rates

Displacement Rate	Aramis Collection Rate
1e-1 (in/s.)	9-10 (pictures/1 s.)
1e-3 (in/s.)	1 (picture/3 s.)
1e-5 (in/s)	1 (picture/360 s.)

Every test performed was recorded in a journal; each entry consistently defined the following:

- Resin Type – E862 Aged or Un-Aged
- Test Type – Tension, compression, or shear
- Temperature – Room Temperature, 50 C, or 80 C
- Notch Radius – 0.0307 in., 0.0614 in., or 0.1535 in.
- Measured Test Section Diameter – Usually 0.154 in.
- Displacement Rate – 1e-1 in/s, 1e-3 in/s, or 1e-5 in/s
- Machine Grip Pressure – Always 3.8 MPa
- Aramis Collection rate – See table 2
- Aramis Facet – Always 13 Size, 9 Step
- Filtering – Always 0 run, 3 Size, Median Type

- Load Channel – Always AD0
- Specimen number – 1 or 2

Any notable occurrences, behaviors, or errors were also recorded. The Aramis facet size and step indicate the number of pixels (similar to nodes in finite element analysis) per region, and the number of these pixels between regions, respectively. Filtering could be used to refine the data, effectively smoothing out the stress-strain curve. The run parameter indicated the number of refinements, the size parameter indicated the range of the refinement, and the type parameter indicated which value was ultimately plotted. Given the nature of these specimens, though, filtering was not necessary (hence the 0 run), and results were obtained without it. For a more avid description of filtering and its implications, see the Aramis User's Manual (GOM, 2007). Finally, the load channel indicates through what channel the 858's computer will provide the loading data, in volts.

The 858 was then prepared for testing. While still in force control it was verified that the force experienced by the specimen was close to zero, and then displacement was auto zeroed. The mode of operation was then changed to Displacement, and it was verified that this was approximately zero. The apparatus was then taken off manual control and locked into place, after which the experiment was initialized. The test would proceed until the specimen fractured, at which point the experiment was manually stopped. The 858 was immediately unlocked and manual operation was enabled. Fig. 5 below depicts a pretest specimen along with a post-test specimen.

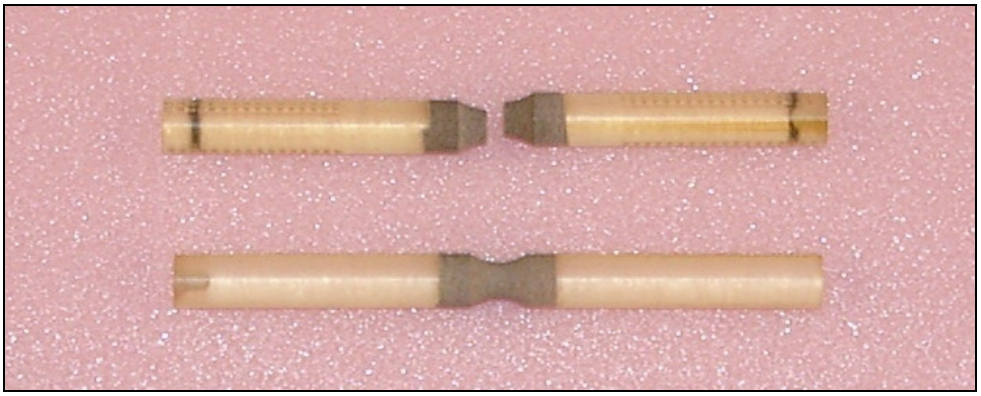

Fig. 5. Post-test specimen (above). Pre-test specimen (below)

The specimen was subsequently removed from the grips, and Aramis was then used to post-process the raw data. Camera mode was abandoned, and start point(s) were defined again (the same points used before the test are the best bet). The computer then calculated the movement of all subsequent points around the start point, thereby producing highly accurate strain measurements throughout all of the stages of the test. Once this was completed, the virtual model of the surface was observed in order to determine (by color coding) the region of maximum or saturation stress. A point was placed on or near this area by control clicking on the image in the desired area. A small graph in the lower right hand side of the screen displayed the stress vs. strain curve for this point. A cylinder was then constructed around this point using the "select on surface" option and a script code found under "Macros," entitled "resin analysis round". This circular cylinder was used to model the circular test section of the specimen, and provided a real time cross sectional area measurement. However the cylinder would often behave erratically by moving out of plane or bulging in one direction. In such cases, a three point circle was formed using the "primitives" option, by selecting three

points on the specimen's surface. The exported file of the resulting circle data would provide the radius of the cross section just as the cylinder would. This was the preferred method, as it was more accurate and efficient. Fig. 6 and Fig. 7 below show the cylinder and the circle, respectively. See Appendix A, Fig. A-11 for a visual description of the computer modes. Excel was used to generate the following for the defined point and region in each stage:

- Strain in the x-direction (transverse)
- Strain in the y-direction (axial)
- Shear Strain
- True Stress
- Engineering Stress
- Load
- Displacement
- Area
- Radius

Strain was measured in % while stress was given in MPa. Load was provided in pounds, while displacement and radius were given in inches, and area in in.^2.

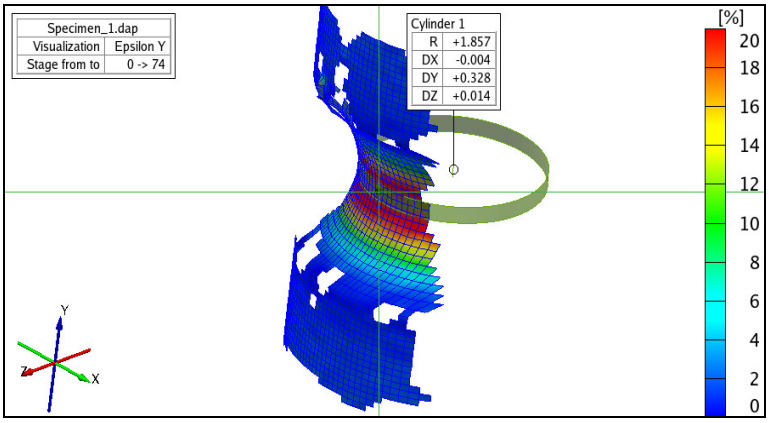

Fig. 6. Specimen fitted with a cylinder

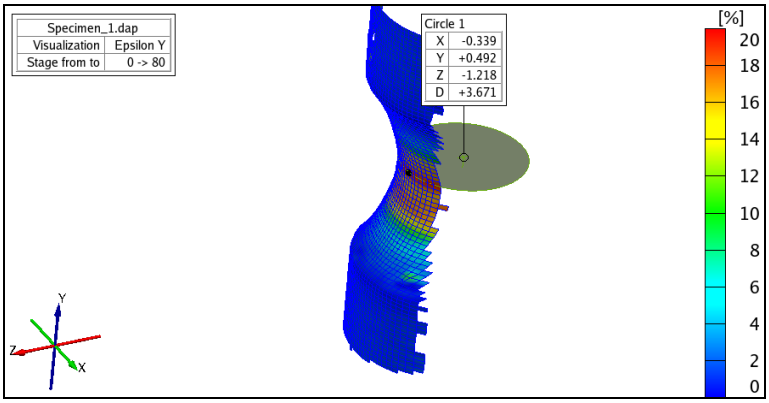

Fig. 7. Specimen fitted with a circle

Testing procedure at higher temperatures

A temperature chamber was installed on the 858 Table Top System in order to accommodate the tests at higher temperatures. This apparatus consisted of the following components:

- A metal stand
- A clear borosilicate glass, rectangular test chamber
- Special grips fitted with thermal couples

- A hose connected to an air source, also fitted with a thermal couple
- A temperature control box with multiple thermal couples
- 4 metal blocks to stand the metal stand on

See Appendix A, Fig. A-14 and Fig. A-15 for detailed pictures of this setup. To install this system, a stand was set over a special modified lower grip, and the hose was connected to an air supply. The special grips were then inserted into the 858's vice grips, and locked into place. Finally the clear test chamber was set on the stand, the grips were positioned, and the thermal couples were all installed. Two were placed around the top and bottom grips, in order to ensure that they would efficiently heat the specimen to the correct temperature. Another was attached to the metal strut where the hose connected to the metal stand, so that airflow into the chamber would be at the desired temperature. The final two couples were attached to wires, which served to indicate the temperature in the chamber and the temperature very near the specimen. All couples were then attached to a blue temperature control box, which allowed the user to set the desired temperature in the chamber.

Each test at 50 C and 80 C were slightly more complex then at room temperature and consequently took more time. The tests at 50 C were conducted first, though the procedure for those at 80 C was identical. Initially, tests proceeded similarly to those at room temperature. The specimens were painted as described before, and both the 858 and Aramis were initialized as described previously. However the grips used with the temperature chamber had to be manually tightened using an Allen wrench. This was

done using a torque wrench with an Allen adaption, in order to ensure uniformity in grip pressure. The back of the clear chamber was removed and the specimen was initially placed in the bottom grip which was tightened to approximately 35 in-lbs in a uniform manner. Two pictures were then taken to ensure that there was no glare from the chamber, and that the shutter time was ideal. The upper grip was then lowered using the manual controls on the computer, and tightened on the specimen in the same manner as the lower ones. The back of the chamber was then screwed back into place, and the 858 was set to force control. The air was then turned on, as was the temperature control box. The desired temperatures for the upper and lower grips, as well as the air coming in were set, and then the heat was initialized. After waiting approximately 12 minutes to allow the specimen to reach the desired temperature, two pictures were taken to establish the base case and the start point(s). The test was then conducted as above. After the specimen fractured, the temperature control was turned off, and the air was allowed to cool the chamber. The back panel was removed from the chamber, and the specimen was taken out, after which the process was repeated. Data was acquired and processed as previously discussed.

Results and analysis of the tests

The tests described previously were designed to explore multiple material characteristics of E862 resin, and to allow comparison between different procurement, structural, and test scenarios. Consequently, the discussion of the results obtained is separated into multiple comparison scenarios, and each has been supplemented by its own appendix.

These appendices are presented in the same order as the discussion of the results, and are referenced accordingly throughout. The parameter φ was calculated according to the formula given within the nomenclature section of this report. Once φ was calculated, the natural log of this parameter was calculated for each data point taken during the tensile test. This new quantity is Epsilon Bar (see the nomenclature section), and it was placed on the x axis of each plot, while stress was placed on the y axis. Epsilon Bar is an average strain in the radial direction calculated using the initial radius and instantaneous radius of the specimen, and thus accurately reflects the behavior of the material. It should be noted that some of the plots display erratic behavior at the initial phases of the test; specifically, the data points appear to jump forward and backward. While the general trend remains the same, these jumps were discovered to be related to the so-called "noise level" of the Aramis Software and cameras. At the beginning of some of the tests (especially those occurring at high displacement rates) the image movement would be extremely fine and thus the cameras had a hard time picking up the movement of the facets. Put plainly, the camera's imaging abilities were at their lower limit and could not pick up the movement of the specks accurately. However given that the general trend remained constant, there is no reason to believe that the data is completely useless, and thus it has been provided for further study.

No aging vs. aged (Appendix B)

The first and foremost comparison involved the specimens that did not receive thermal aging and those that did. The data for these comparisons can be found in Appendix B.

The effects of aging surfaced most prominently in the tests conducted at 50 C and 80 C, while minimal effects were observed on room temperature tests. These effects were also prominent in the longer displacement rate tests (those conducted at 1e-3 in/s and 1e-5 in/s). It was discovered that the aged specimen almost always yielded at a higher stress then the un-aged in these situations, indicating that the thermal aging process actually served to harden the epoxy by providing extra curing.

Notch radius comparison (Appendix C)

An analysis of the behavior of the different notch radii was then conducted, the data for which can be found in Appendix C. The bars of notch radius 0.0307 in. almost always failed at a higher stress then the other two, followed by the bars of radius 0.0614 in. and finally the bars of radius 0.1535 in. almost always failed at the lowest stress. Concerning yield stress (saturation stress), all three notch diameters would usually hit this point around the same magnitude of stress, though on several occasions all three would yield at different points. See Appendix C for specific values and comprehensive plots.

Temperature comparison (Appendix D)

Another very relevant analysis was conducted on the effects of temperature, the details of which are located in Appendix D. It was discovered that the tests conducted at room temperature and at 50 C showed little divergence from one another, which indicates that the behavior of E862 at these temperatures is strikingly similar. The thermally aged

specimen consistently beat out the un-aged at 50 C, while there existed little difference between the corresponding two at room temperature. The effects of temperature were adamantly observed in the tests conducted at 80 C. These specimens consistently yielded and failed at lower stresses, indicating that E862 becomes weaker at this high temperature. Interestingly, the aged specimen always yielded at a higher stress then the un-aged, shortly after which it would fail, whereas the un-aged specimen would continue to yield and fail sometime after. This salient contrast strengthens the hypothesis that the thermally aged specimens became harder, which would cause them to yield at a higher stress, but fracture more quickly after this point. A full range of comparison data can be found in Appendix D.

Displacement rate comparison (Appendix E)

Finally the different displacement rates at which these tests were conducted were compared in Appendix E. These results bear testament to the accuracy and precision with which each test was conducted. The higher rate (1e-1 in/s) consistently failed at a higher stress, followed by the middle rate (1e-3 in/s), and finally the low rate (1e-5 in/s). There was not one instance where this order was disrupted, although at the higher temperatures, there was no low rate to compare with. Thus the expected outcome of this comparison was indeed observed, indicating that E862 fails at higher stresses when subjected to higher displacement rates, and at lower stresses when subjected to low displacement rates. Details are located in Appendix E.

Ultimately the goal of these tests was achieved. A massive quantity of data was gathered and processed, which serves to enhance our understanding of the material properties of resin E862, and its behavior at all manner of conditions. With this vast array of knowledge, we can confidently build and refine excellent material and structural models, which will undoubtedly unlock the answers to a multitude of imperative questions. All of the tested specimens were transported back to Texas A&M for further analysis. Specifically, SEM technology will be used to observe the fracture surfaces of these specimens, which will yield insight into fracture initiation and failure mode. A finite elements model of the failure will then be constructed using a macromolecular polymer model supplemented by a fracture model. The next chapters will be dedicated to a description and analysis of these processes.

CHAPTER III

INITIAL SEM TRAINING AND ANALYSIS

To expand the understanding of how E862 fractures and to make possible the development of a finite element model of this resin, Scanning Electron Microscopy was utilized. The process began with initial training and certification on the Scanning Electron Microscope.

Training and certification

At Texas A&M University, within the Microscopy and Imaging Center (MIC) in the Biological Sciences Building, the JSM-6400 SEM is housed. This microscope is used to image materials ranging from insect wings to metal composites, and provides superior close-up pictures of the material surface. Extensive training and practice is required on this machine before a user can operate it at their leisure. Initially one is required to read Chapter 7 of *Electron Microscopy: Principles and Techniques for Biologists*, which discusses the elementary methods of electron microscopy and provides an overall account of how the machine works (Bozzola and Russell, 1999). Once this chapter was memorized sufficiently, a short exam was administered at the Microscopy and Imaging Center. Upon successful completion of the exam the training began. For approximately one month, meetings would be held in the lab during which one could practice preparing and imaging specimens. To aid in studying a pamphlet was provided entitled “JSM-6400 General Operating Instructions” which provided specific details for the operation of the

JSM-6400 (MIC, 1993). Finally a usage test was administered in which the trainee demonstrated their knowledge of how to use the microscope without the aid of the trainer. Upon successful completion of this test, a certificate was issued permitting the student to use the microscope at their leisure.

Initial imaging

With the training completed, several trial runs were made on the actual resin specimens in order to gauge their behavior under the scope. The very first of these runs involved placing an uncoated specimen in the specimen chamber and attempting to resolve the image. Most specimens require some type of coating before being placed in the imaging chamber, to prevent the buildup of charge on the surface. This charging makes the image blurry and appear to glow, and thus is unacceptable when attempting to retrieve a usable image. It was discovered that without coating, the fracture surfaces of the resin specimens could not be resolved. Thus the next runs were conducted with argon-coated specimens using a sputter coating technique provided by the MIC. Fig. 8 and Fig. 9 Below show two images of the same specimen. They both depict the point of fracture initiation, located in this case at the surface of the specimen. This specimen was of no great interest due to the fact that the fracture occurred at the surface, indicating a defect.

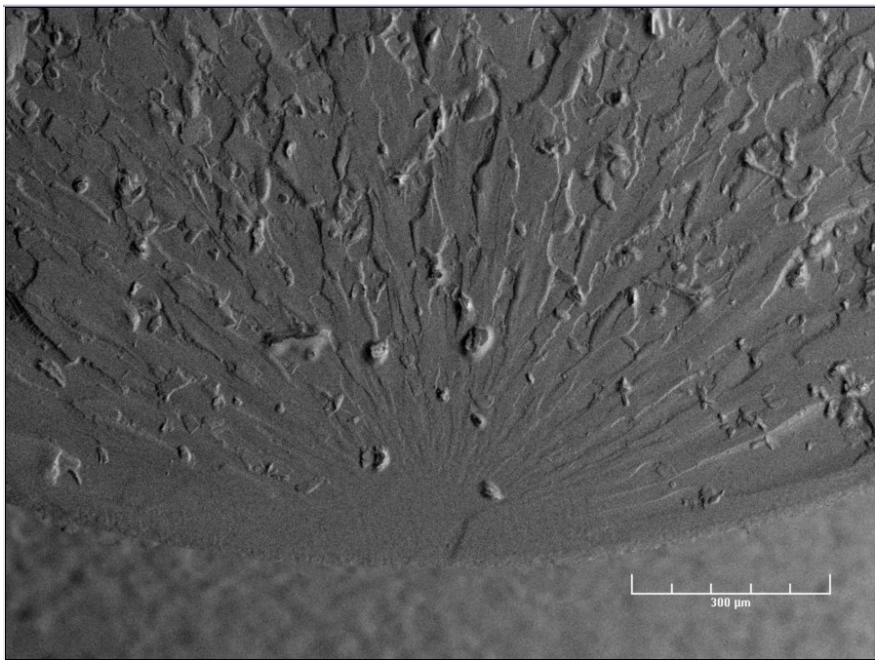

Fig. 8. Specimen imaged using SEM and coating

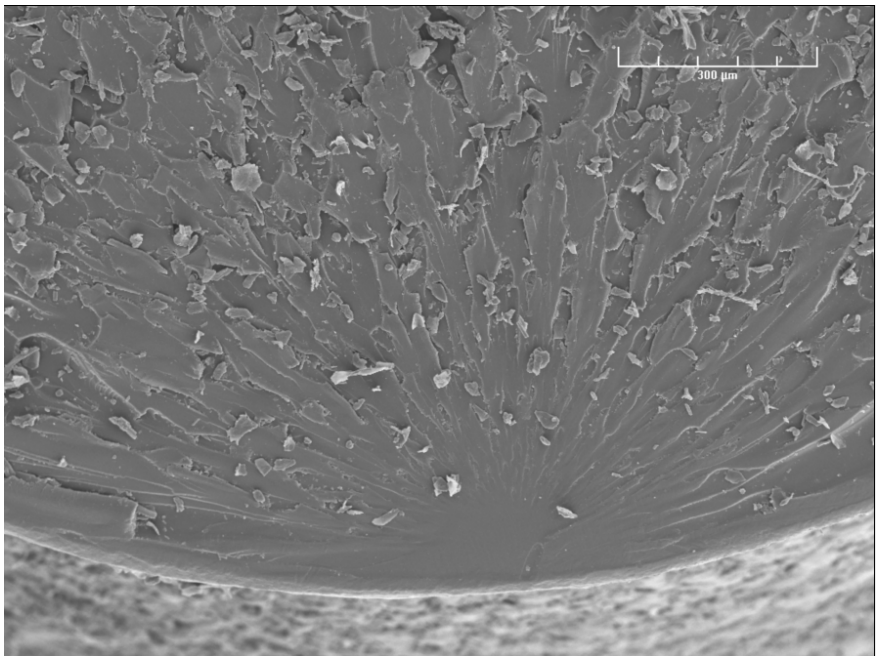

Fig. 9. Close-up of specimen imaged using SEM and coating

However the extremely intricate detail shown by the SEM appears quite spectacular compared to the low powered images made previously. Once these images were obtained it was decided that coating is an absolute necessity if clear images are to be obtained. A problem that arose with this necessity though; once coated the specimens become unusable after approximately two weeks and thus the fracture surfaces will not be observable by any means following this time period.

Results of preliminary imaging

SEM technology proved to be an extremely valuable asset to this research project. The images are pristine and revealing, and can be obtained relatively quickly with minimal effort. It is now possible to gage the nature of the fracture more thoroughly and determine exactly which fractures depict accurate material properties. The direction and propagation of the fracture can now be distinguished, two factors which will allow the creation of an accurate material model.

SEM technology has also given rise to new questions. Fig. 10 below shows a fascinating feature of crack propagation. It is hypothesized that the rib-like structures seen in the upper half of the image are shear planes which formed as the initial fracture worked its way through the interior of the specimen. The process of fracture begins with the build up of stress (called a stress concentration) at a certain point within the material. In the case shown above, the concentration formed around a small defect in the surface of the notched bar. Once this concentration reaches a maximum (termed saturation stress),

fracture is initiated. As the crack propagates through the primary structure, it tends to follow the path of least resistance, and these paths are normally referred to as shear planes (Chowdhury et al., 2008c). The actual fracture initiation point (not shown) is below the image presented here, which helps to validate this hypothesis though it is not yet for certain.

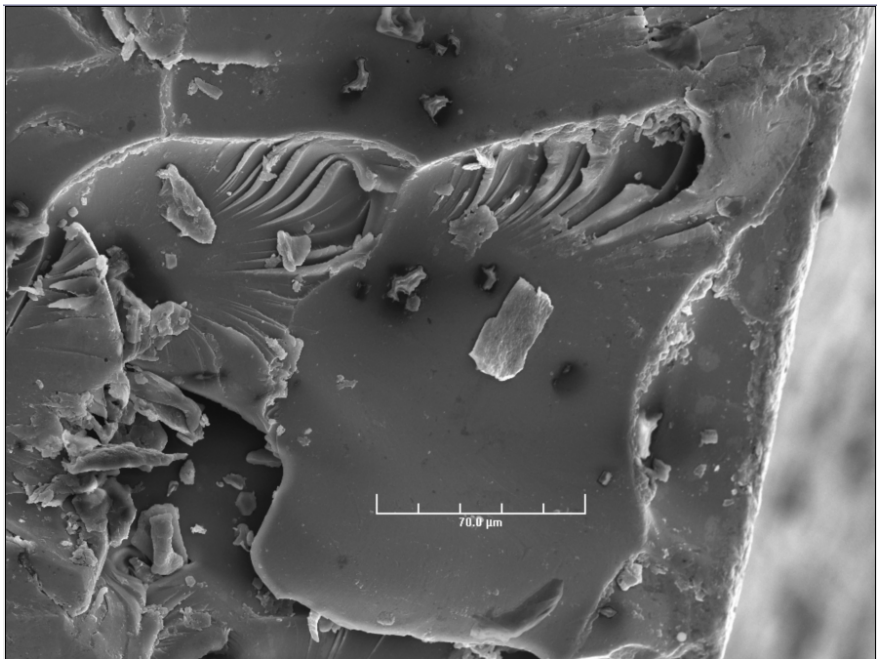

Fig. 10 Possible shear planes on fracture surface

With the ability to image the fracture surfaces of the specimens at extremely high magnifications, new possibilities have presented themselves, and exploration becomes inevitable. Once an ultimate understanding of the nature of these fractures is attained, the modeling process can begin.

CHAPTER IV

SUMMARY AND FUTURE WORK

At this time, no further progress was made towards the final goal of modeling the fracture of the resin specimens using Finite Element Methods. A more detailed analysis of the fracture surfaces using SEM technology is necessary before an accurate model can be derived. Regrettably, the analysis takes a great deal of time, and will continue to do so until a better understanding of the crack propagation and cause is reached. However once this milestone is attained, an accurate model will almost certainly be created soon after. Science is oftentimes fickle and thus it is always hard to accurately predict how much time will be necessary to complete an experiment or conclude an analysis.

Summary of work completed

While the research set out to accomplish was not completed fully, a great deal of work and analysis were performed during this year and during the summer of 2008. These efforts have produced a strong basis from which future work can evolve.

Test and analysis at NASA Glenn Research Center

The first milestone of the project was completed during the summer of 2008 at NASA Glenn Research Center. An extremely large amount of tensile tests were performed on E862 notched bar specimens. These experiments were completed over a range of different specimen notch radii, different displacement rates, and different temperatures.

Aging was also explored given that E862 is a thermosetting polymer, and should therefore become stronger as temperature increases. A vast amount of data was compiled and processed, the majority of which can be found in the appendices. Gathering this data was an extremely vital part of this project. The data provided a great deal of material parameters necessary to characterize E862 fully, and a means to obtain a deeper understanding of how the resin would behave in high tension. Given that this resin will be infused into composite matrices which will then be used in the creation of fan blade cases, this data will allow for an elementary analysis of the structure's behavior at the most basic level.

SEM training and analysis

Once the data was processed and briefly analyzed for accuracy and content, the second phase of the project commenced. A more superior understanding of the exact nature of the individual fractures was desired, and thus SEM technology became the main focus. Before this technology could be implemented, training was necessary given the sensitivity and importance of the equipment and processes involved. The training took approximately one and a half months, during which a multitude of practice sessions and evaluations occurred to ensure confidence and efficiency when utilizing the machinery and extracting clear, concise images. Once the training was completed, several SEM sessions were conducted during which the fracture surfaces of the actual specimens were imaged using different coating techniques to determine which would expose the most detail. It was discovered that the process of sputter coating, in which the specimen is

coated with a metallic argon mixture, served as the most effective method. The only undesirable characteristic of this coating procedure was that the specimens prepared with it become useless thereafter. The coating on the fracture surface makes it impossible to reimage the specimen. However pristine images can be obtained with it as shown in Chapter III and thus this procedure will most likely be the one of choice for future imaging. With the use of SEM technology a greater insight into how the resin behaves during fracture can be gained and thus a more complete model can be developed.

Future work

While a great deal of work has already been done, there still exists a substantial amount of research and work still to be completed. Preliminary imaging has already been completed, but there are still a substantial number of specimens to be imaged. There are specific fracture propagation characteristics that are the target of this imaging process, some of which have not been fully developed yet and thus the exact nature of what exactly needs to be imaged must still be determined. However once a complete database of images has been compiled, the next phase of research can move forward.

The final product of this research project is a complete model of the fracture of E862 resin. More specifically, a model of the behavior of this resin under extreme tension and fracture is of the highest concern. As of now the specimen geometry will be imported into Abacus, a finite elements software program designed to model all types of materials under a variety of loads and stresses. Once fracture models for the different specimen

geometries and test conditions have been completed, they will be used to create a generalized model for E862. At this point, the universal model can be added to the model for the entire fan blade case, and the final product will be complete. This will undoubtedly lead to a safer, more efficient composite fan blade case, which will most likely become the case of choice for turbofan engines in general.

REFERENCES

Boyce, M. C., Parks, D.M., Argon, A. S., 1988. Large Inelastic Deformation of Glassy Polymers, Part I: Rate Dependent Constitutive Model. Mechanics of Materials, 7, 15-33.

Bozzola, J. J., Russell, L.D., 1999. Electron Microscopy: Principles and Techniques for Biologists. Jones and Bartlett Publishers, Inc., Sudbury, MA.

Chowdhury, K. A., Benzerga, A. A., Talreja, R., 2008a. An Analysis of Impact-Induced Deformation and Fracture Modes in Amorphous Glassy Polymers. Engineering Fracture Mechanics, 75, 3328-3342.

Chowdhury, K. A., Benzerga, A. A., Talreja, R., 2008b. A Computational Framework for Analyzing the Dynamic Response of Glassy Polymers. Computational Methods Appl. Mech. Engrg.

Chowdhury, K. A., Benzerga, A. A., Talreja, R., 2008c. Effects of Manufacturing-Induced Voids on Local Failure in Polymer-Based Composites. Journal of Engineering Material Technology, 130, 021010.

GOM, 2007. Aramis Opperational Manual. GOM Optical Measuring Techniques. Munich, Germany.

Littell, J. D., Ruggeri, C.R., Goldberg, R. K. Roberts, G. D., Binienda, W. K., 2007. Measurement of Epoxy Resin Tension, Compression, and Shear Stress-Strain Curves Over a Wide Range of Strain Rates Using Small Test Specimens. NASA In House Publication, Cleveland, OH.

Llorca, J., Needleman, A., Suresh, S., 1991. An Analysis of the Effects of Matrix Void Growth on Deformation and Ductility in Metal Ceramic Composites. Acta Metall. Mater., 39, 2317-2335.

Microscopy and Imaging Center (MIC), T., 1993. JSM-6400 General Operating Instructions. Texas A&M University, College Station, Tex.

Paley, M., Aboudi, J.A., 1992. Micromechanical Analysis of Composites by the Generalized Cells Model. Mechanics of Materials, 14, 127-139.

APPENDICES

The following appendices contain images and data taken and processed at NASA Glenn Research Center during the summer of 2008. It should be stressed that these appendices do not contain all of the data accumulated during the testing at Glenn, but rather the most prominent and useful parts. To include all of the data would be unnecessary and inefficient.

The appendices are organized and separated according to the testing parameters introduced in Chapter II. Rather then provide each image and plot with a lengthy caption, the appendices have been separated in a chapter-like fashion in order to make referencing and locating data simpler and user-friendly. Each figure is however labeled in numerical succession for referencing purposes. The plots in each appendix come in pairs; both engineering and true stress are provided for the same range of data for each test parameter. To avoid any confusion, the series in each plot are labeled clearly, and each label ends with either “true” or “eng” indicating that that series is showing true stress or engineering stress, respectively. Each plot title is either “Engineering Stress” or “True Stress” which also aids in avoiding confusion. All plots are made with respect to Epsilon Bar; for the meaning of this parameter see the nomenclature section.

APPENDIX A

DIAGRAMS

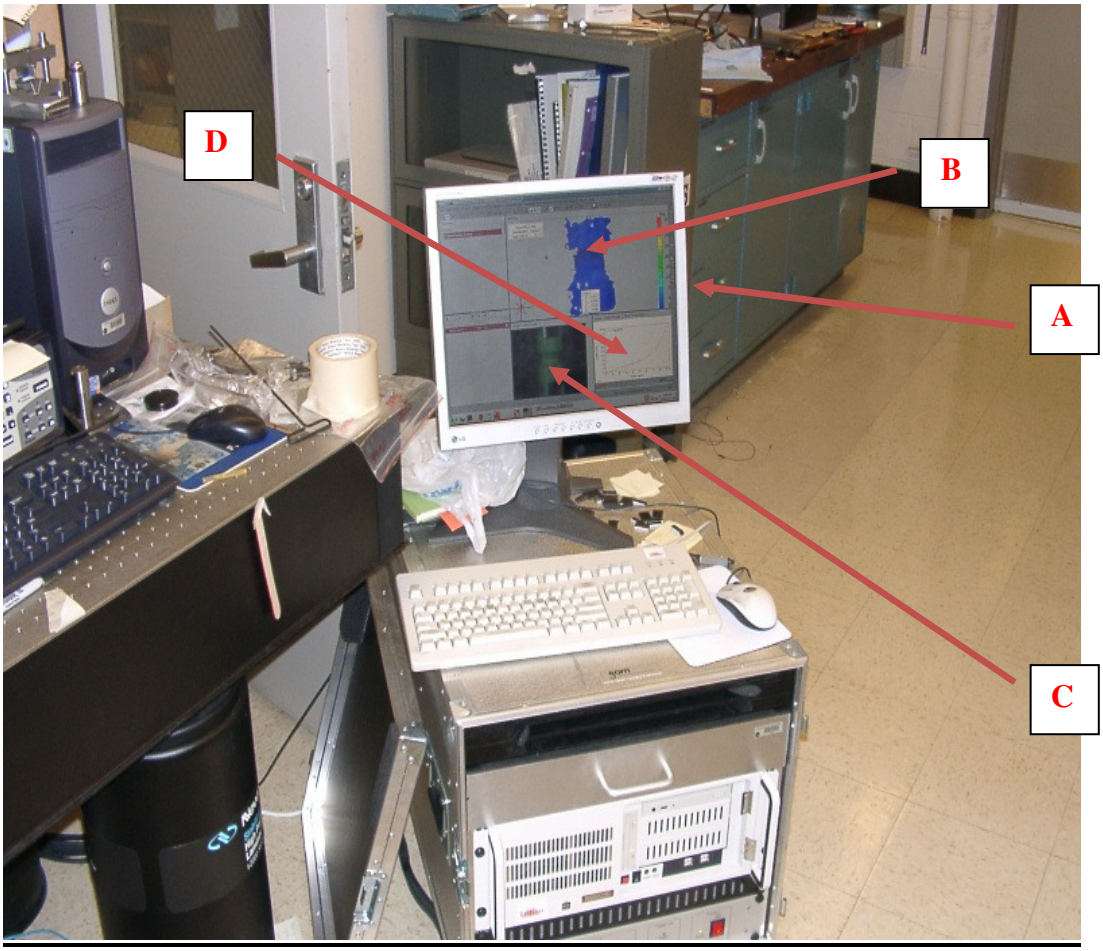

Fig. A-11 Aramis computer system

A) Monitor
B) 3D Model of Specimen
C) Camera View of Specimen
D) Stress vs. Strain Plot for Selected Point

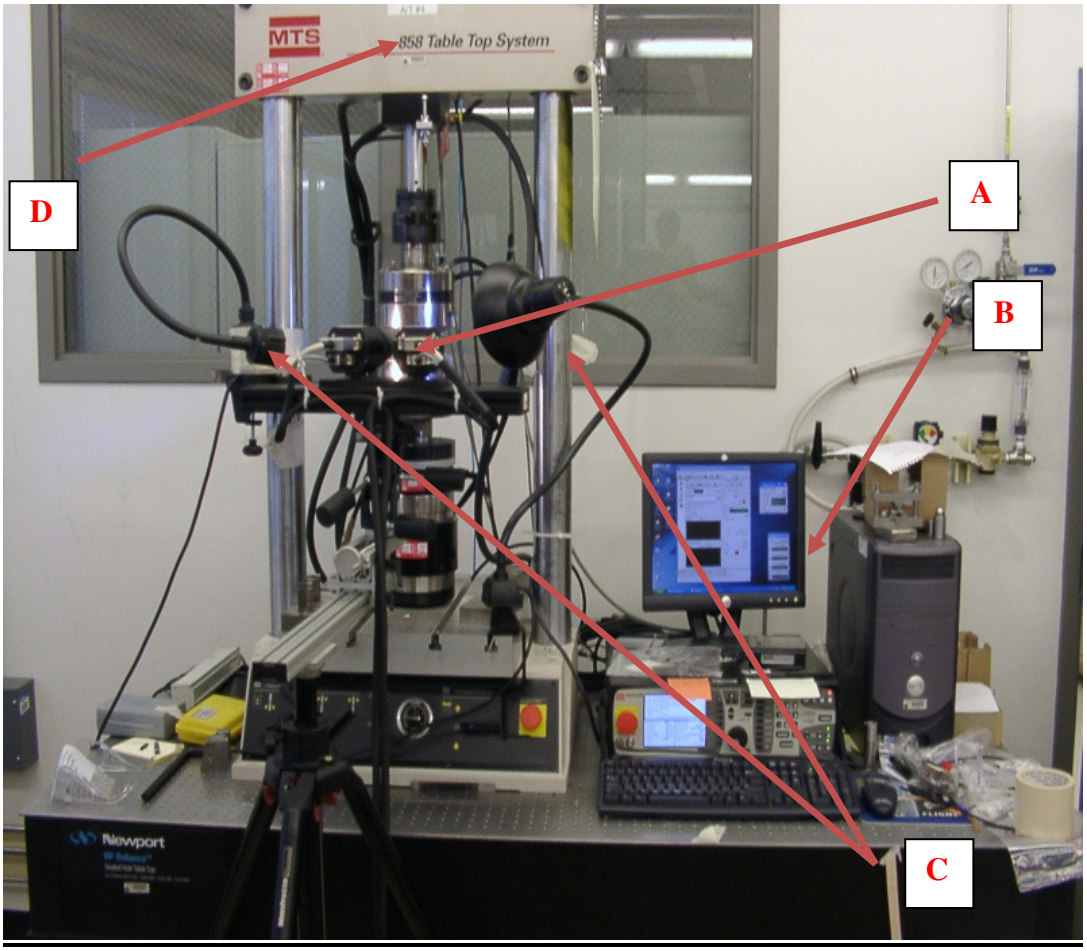

Fig. A-12 Room temperature setup

A) Aramis Cameras
B) MTS 858 Table Top System Computer Control
C) Lamps
D) MTS 858 Table Top System

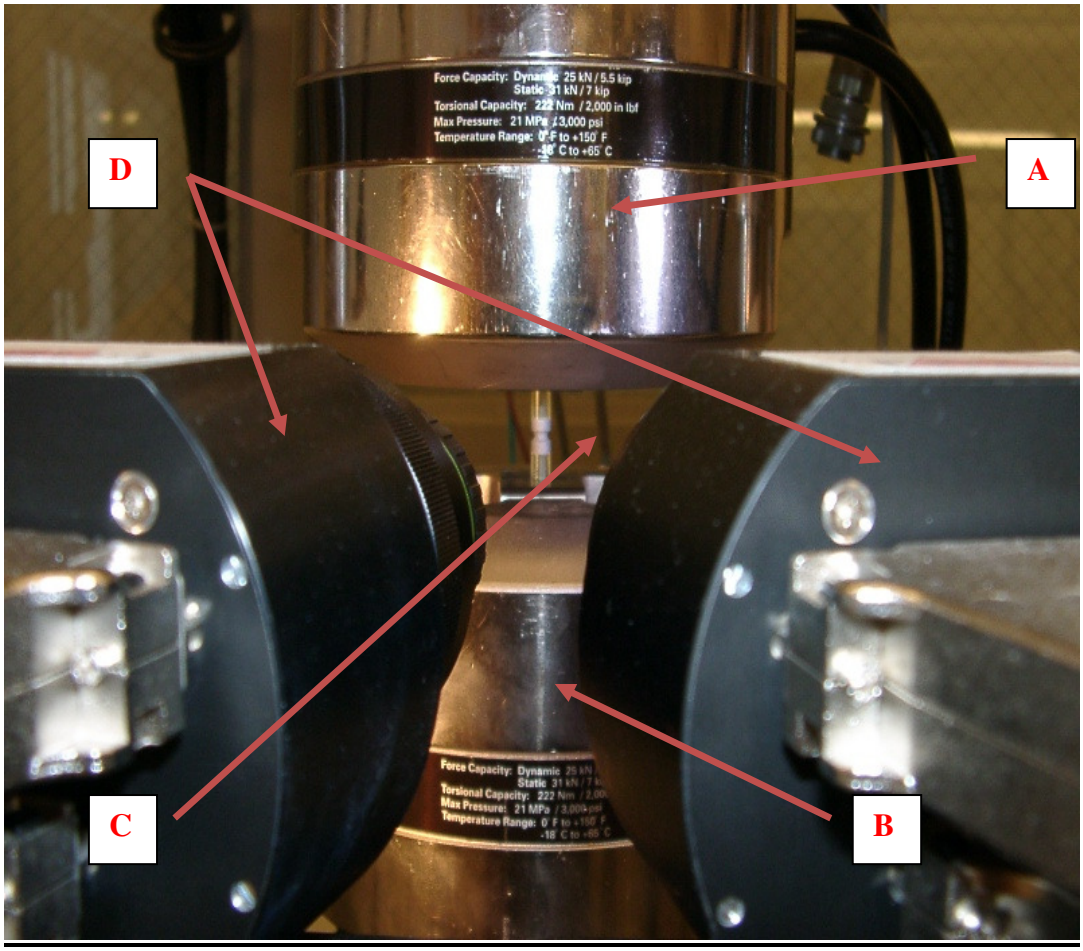

Fig. A-13 Room temperature test section

A) Upper Grip
B) Lower Grip
C) Test Specimen
D) Aramis Cameras

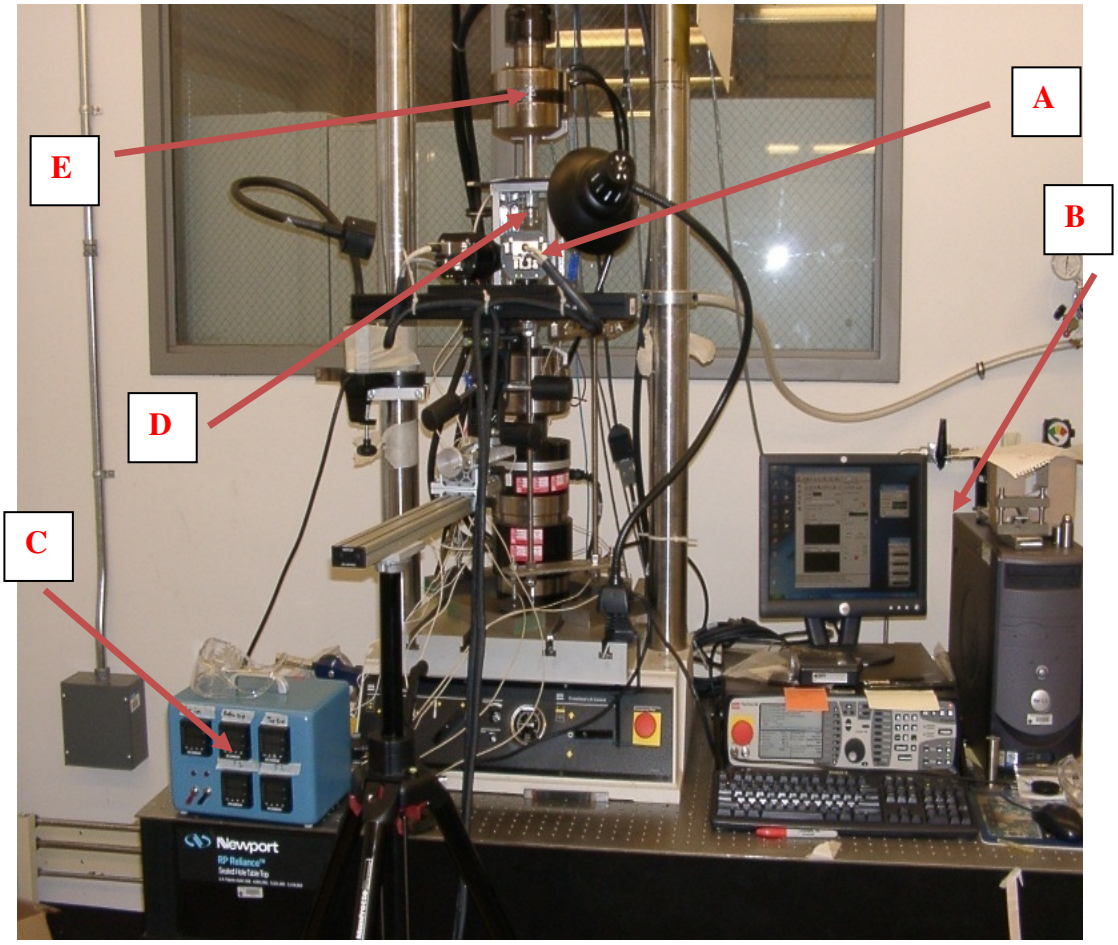

Fig. A-14 50 C and 80 C configuration

A) Aramis Cameras
B) MTS 858 Table Top System Computer Control
C) Temperature Control Box
D) Test Chamber
E) MTS 858 Table Top System

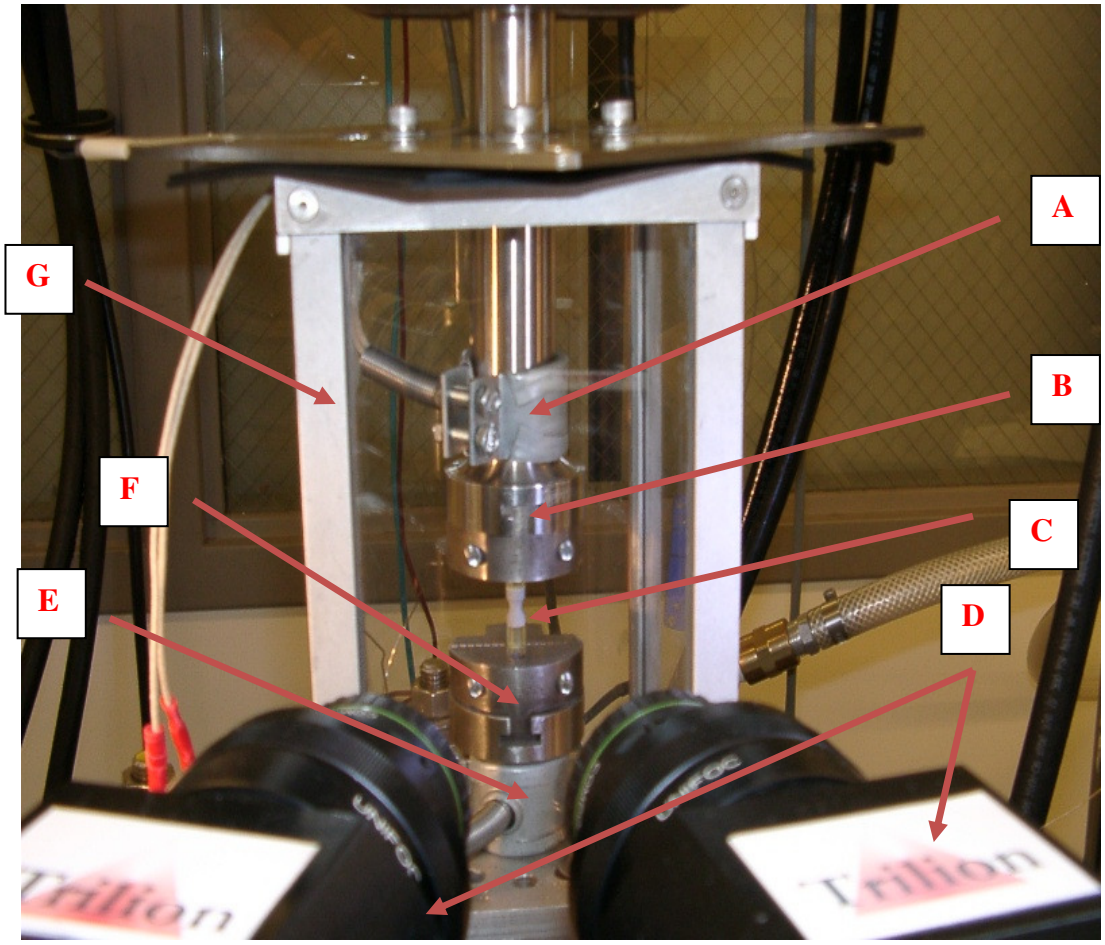

Fig. A-15 Temperature test chamber

A) Upper Grip Thermal Couple
B) Upper Grip
C) Test Specimen
D) Aramis Cameras
E) Lower Grip Thermal Couple
F) Lower Grip
G) Temperature Chamber

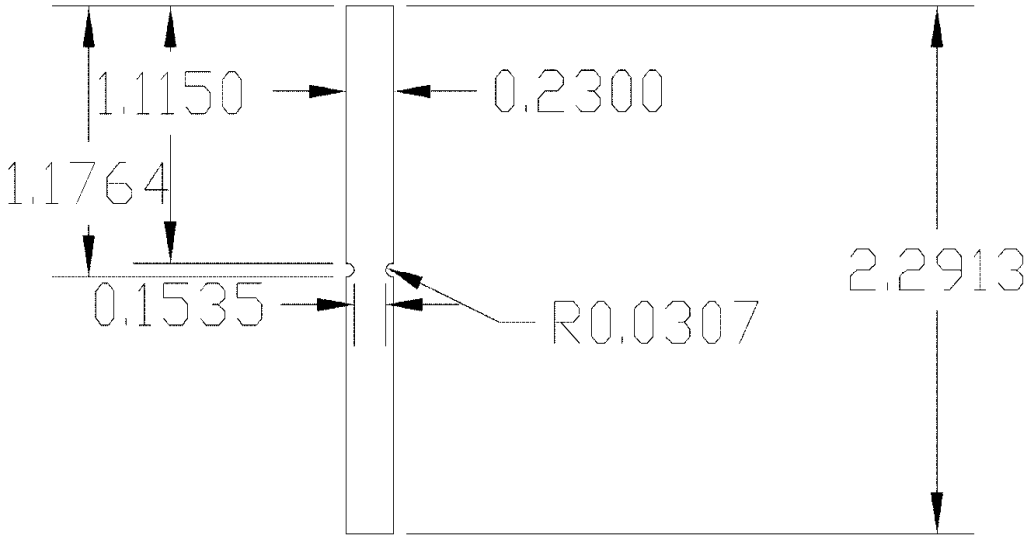

Fig. A-16 Specimen of notch radius 0.0307 in.

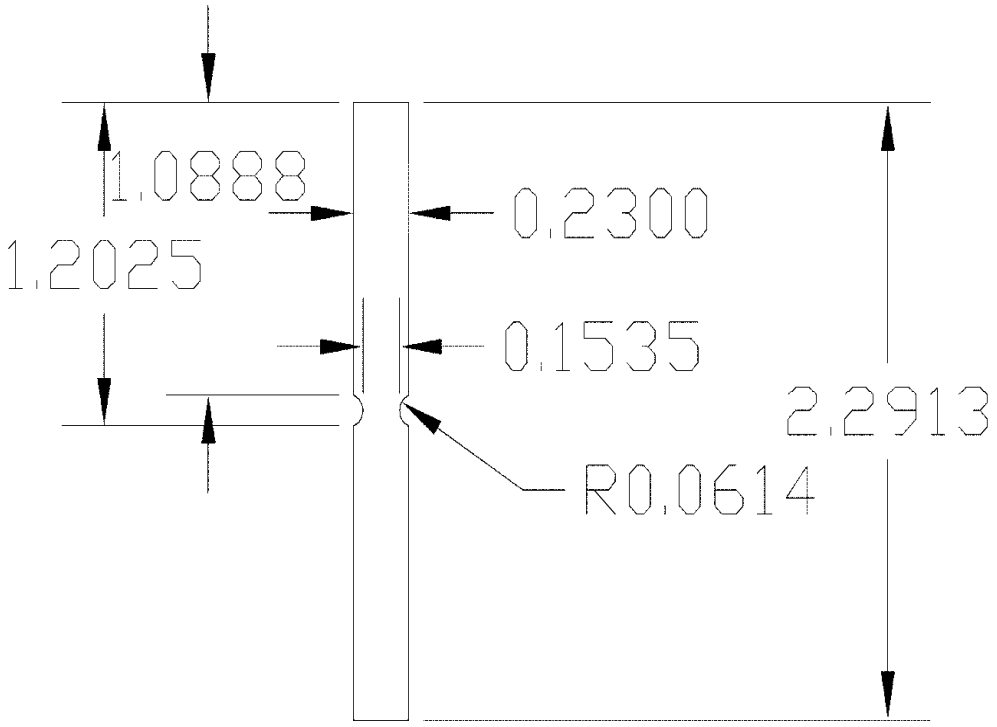

Fig. A-17 Specimen of notch radius 0.0614 in.

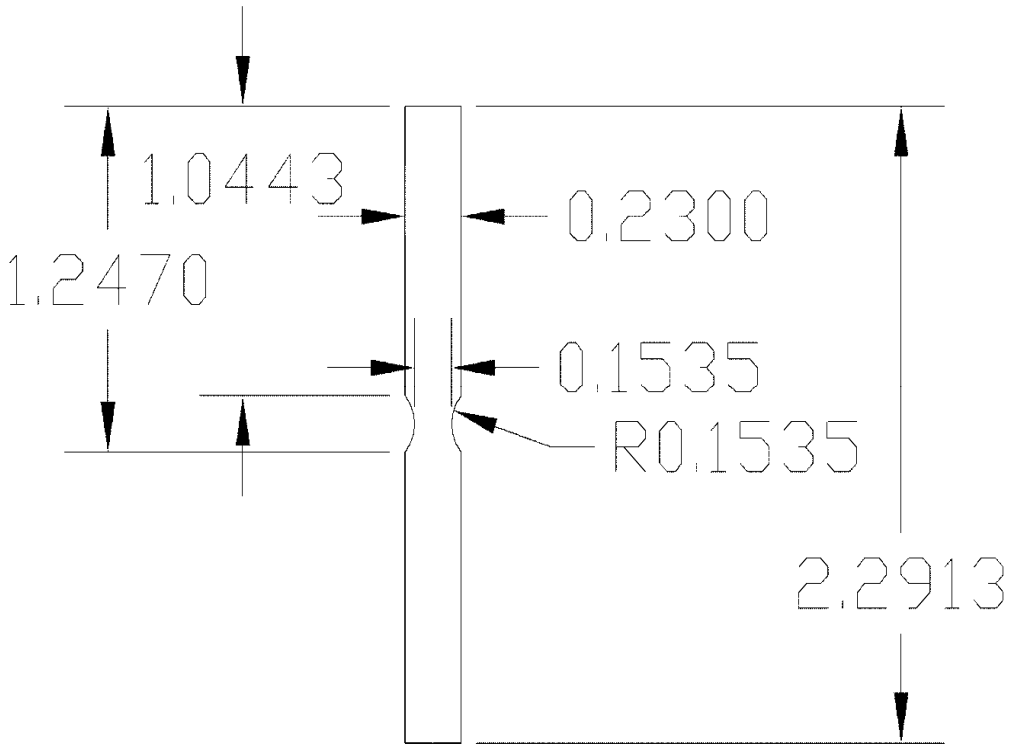

Fig. A-18 Specimen of notch radius 0.1535 in.

APPENDIX B

NO AGING VS. AGED DATA

I. Room Temperature
   a. Notch Radius 0.0307 in.
      i. Displacement Rate 1e-1 in/s

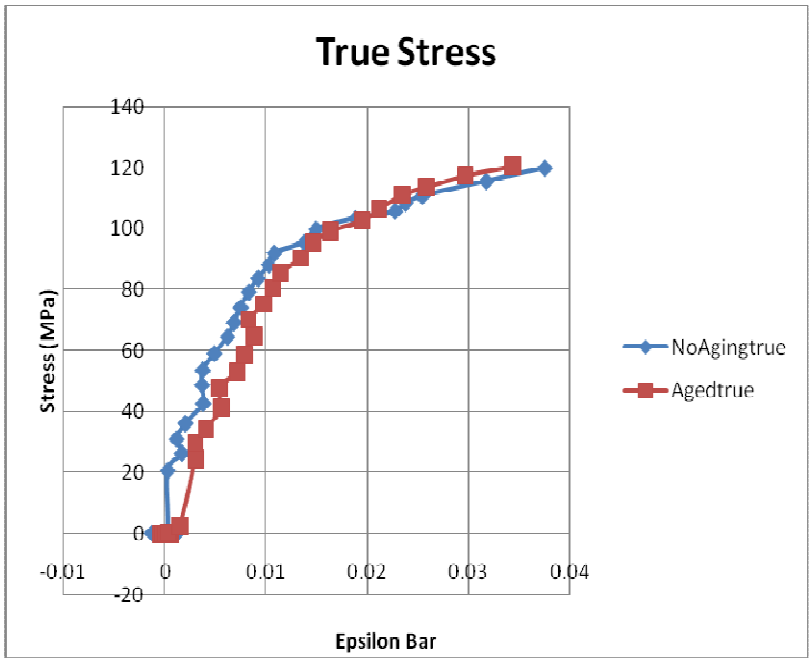

Fig. B-19

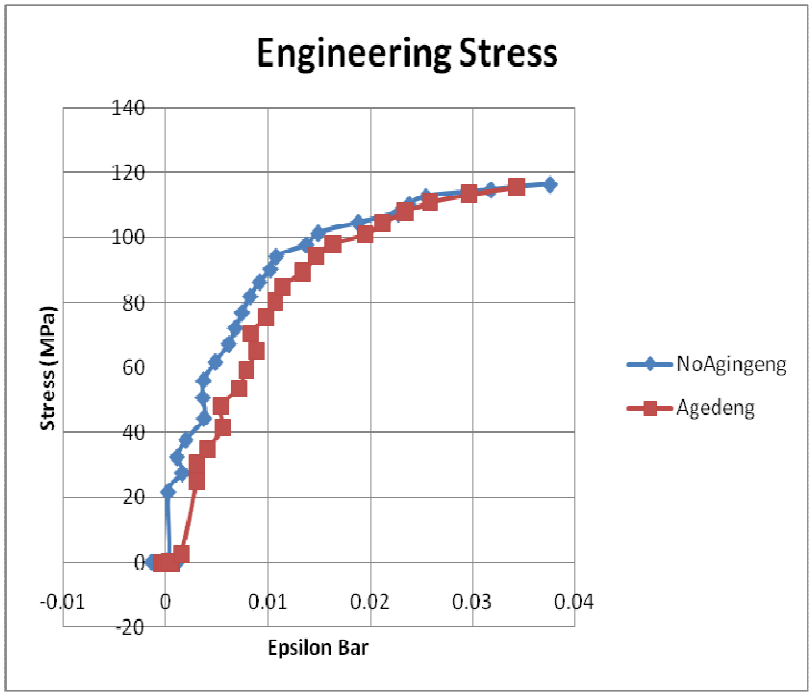

Fig. B-20

ii. Displacement Rate 1e-3 in/s

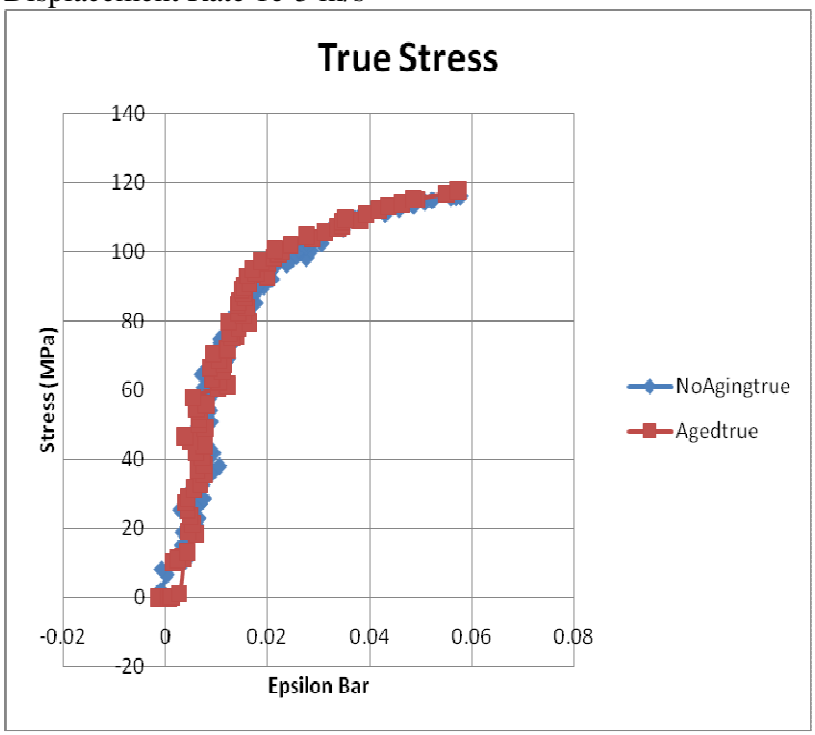

Fig. B-21

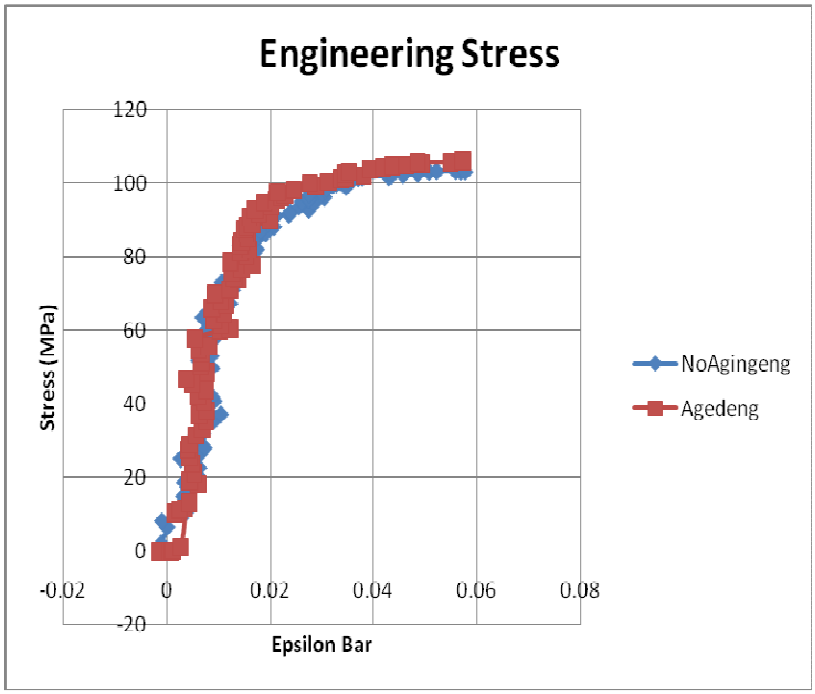

Fig. B-22

iii. Displacement Rate 1e-5 in/s

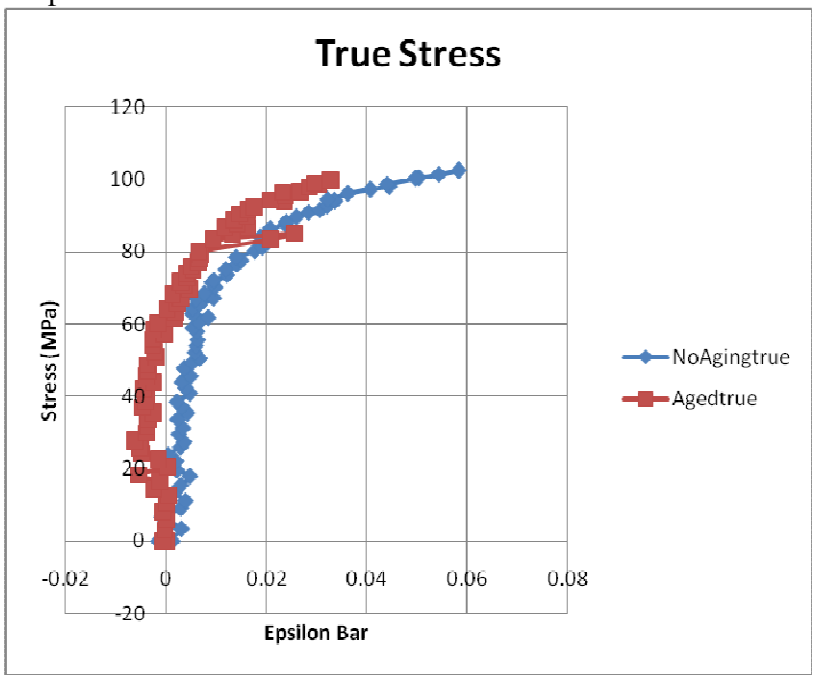

Fig. B-23

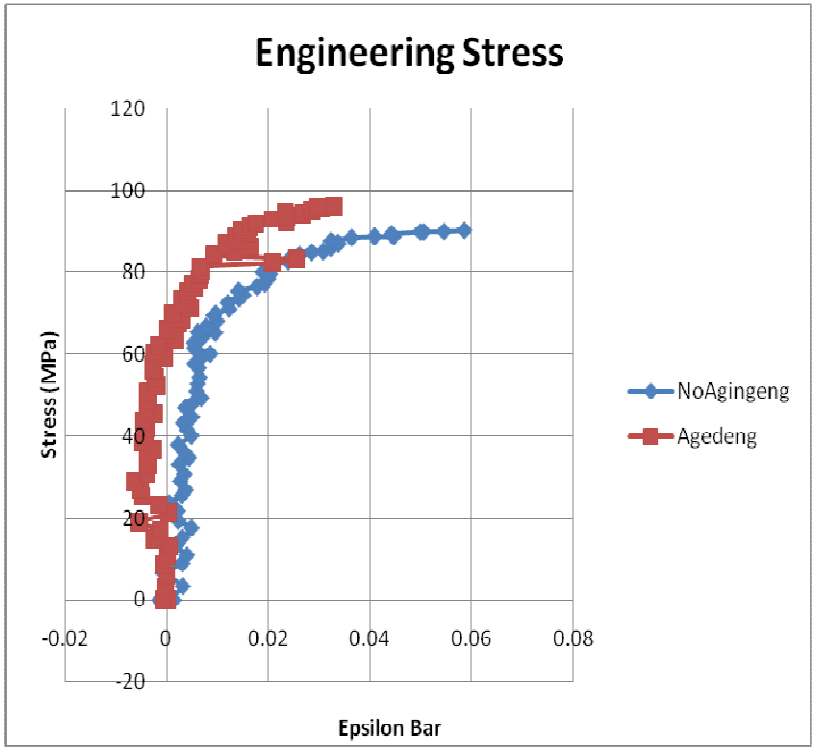

Fig. B-24

b. Notch Radius 0.0614 in.
    i. Displacement Rate 1e-1 in/s

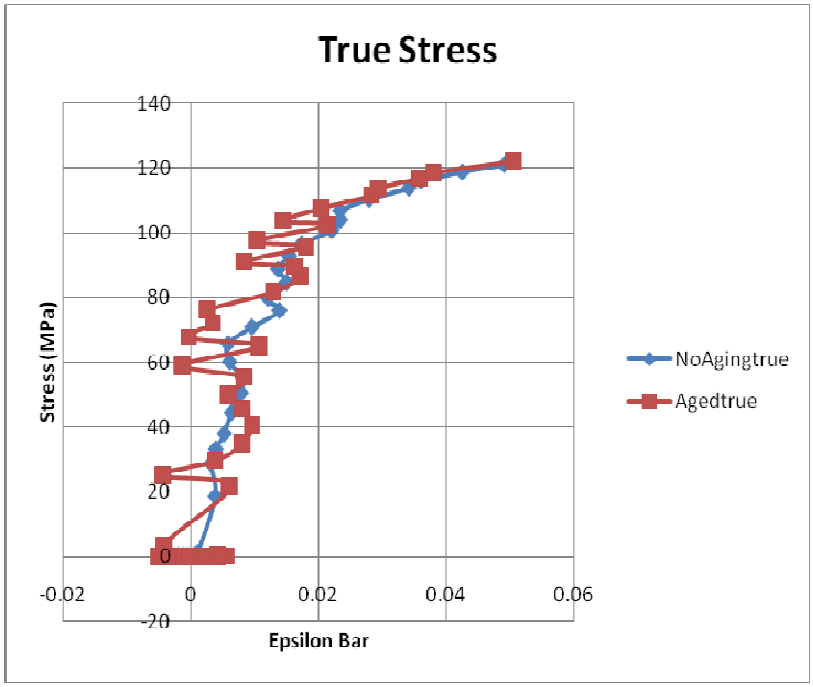

Fig. B-25

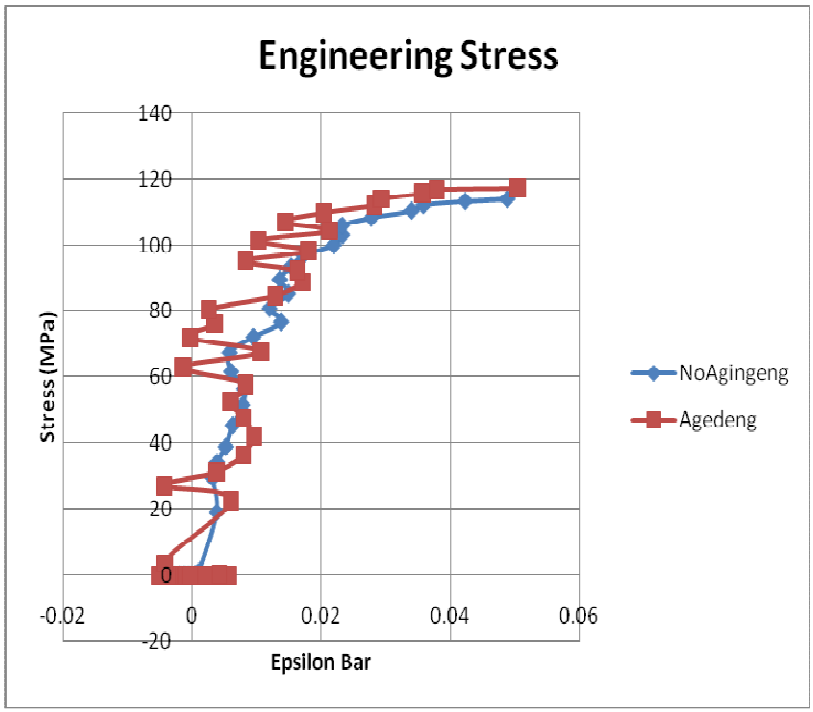

Fig. B-26

ii. Displacement Rate 1e-3 in/s

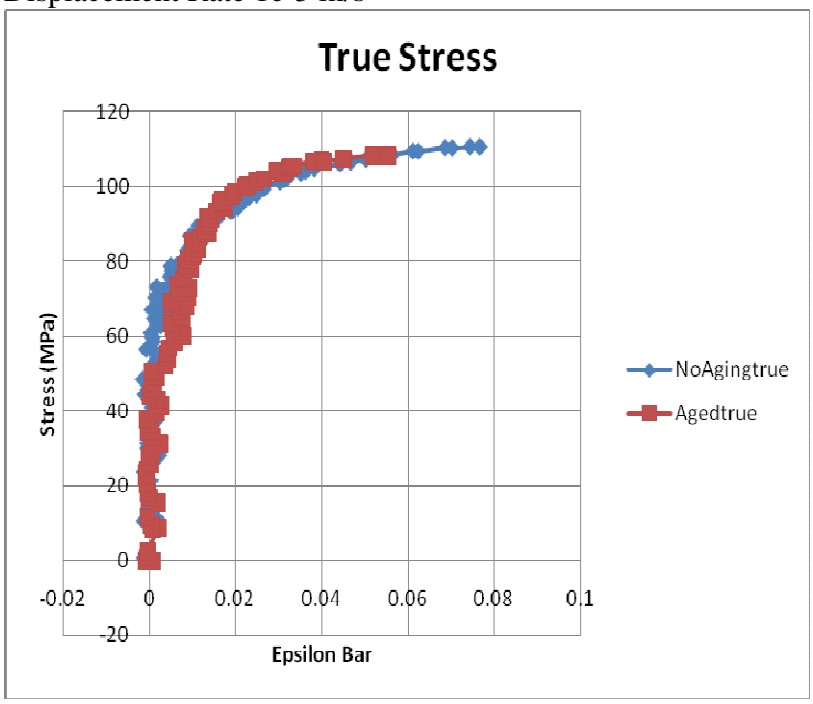

Fig. B-27

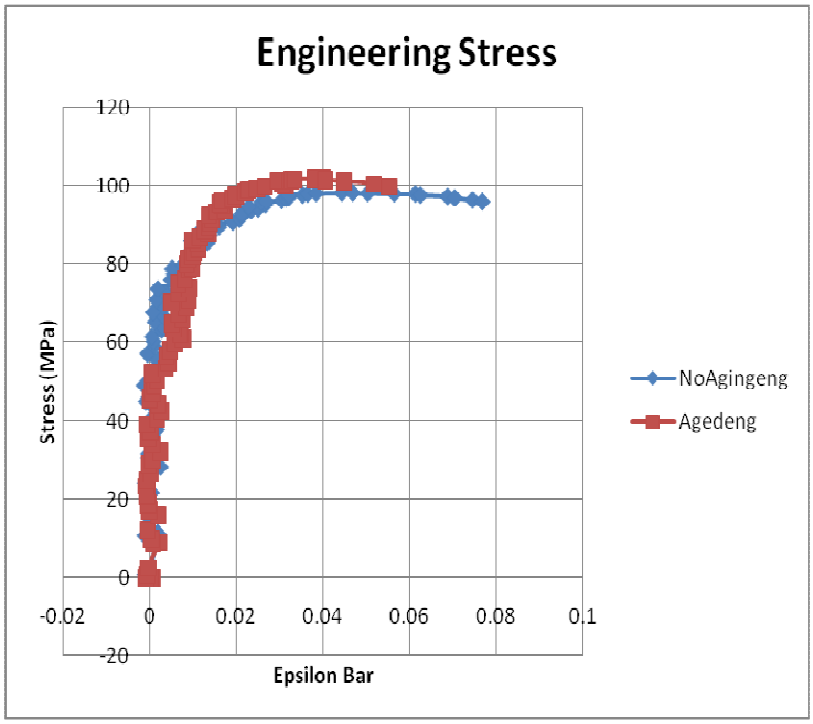

Fig. B-28

iii. Displacement Rate 1e-5 in/s

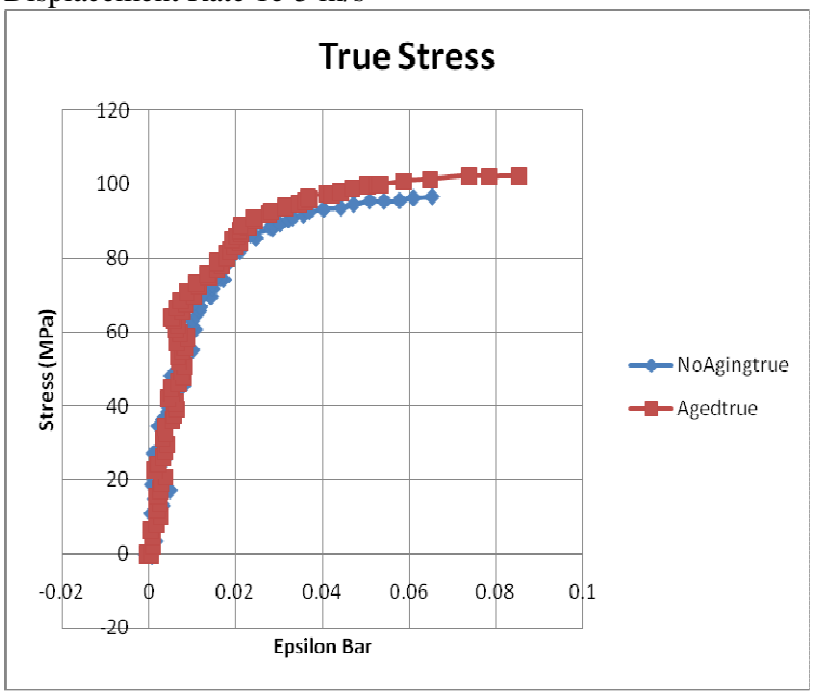

Fig. B-29

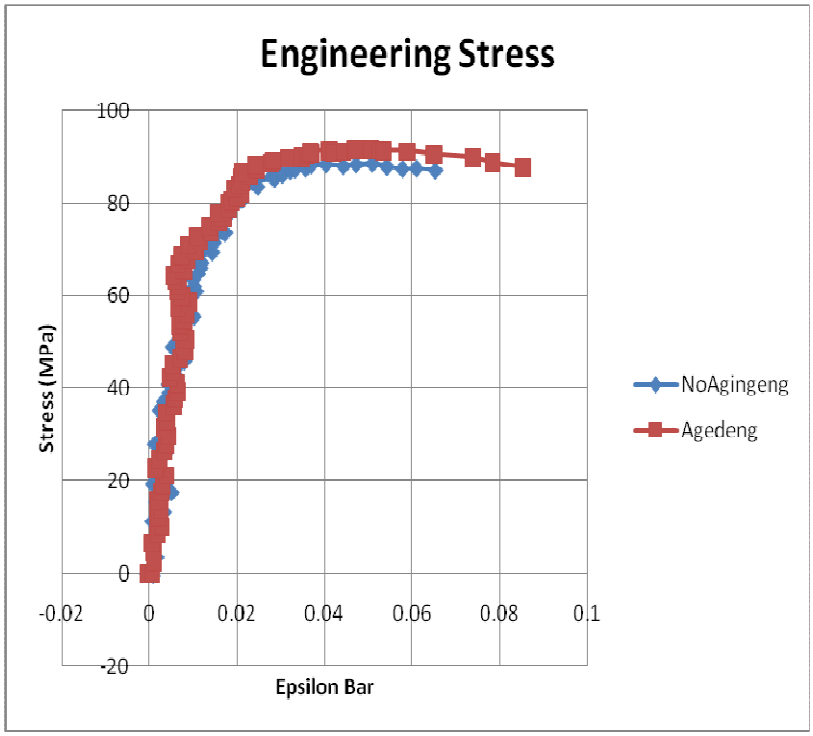

Fig. B-30

c. Notch Radius 0.1535 in.
   i. Displacement Rate 1e-1 in/s

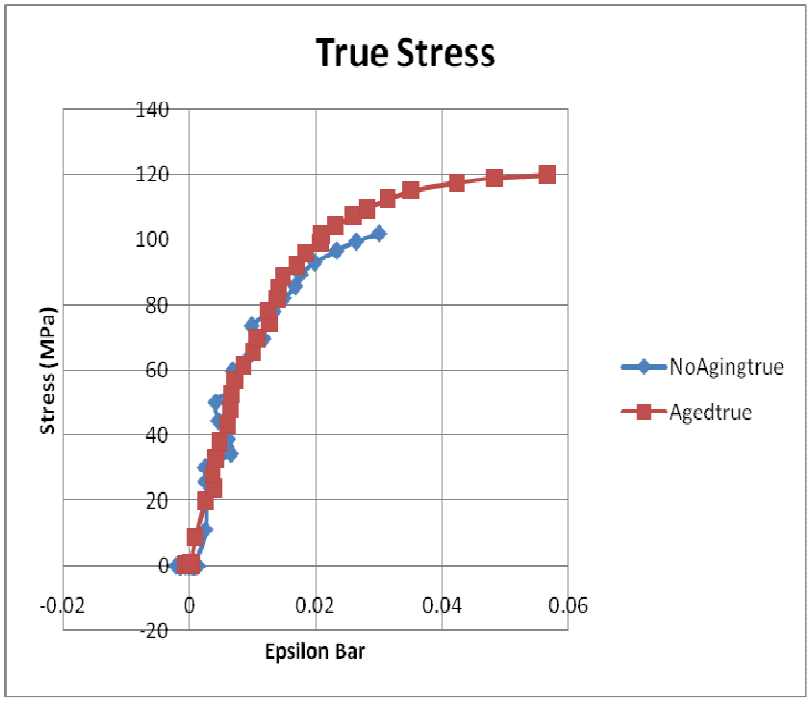

Fig. B-31

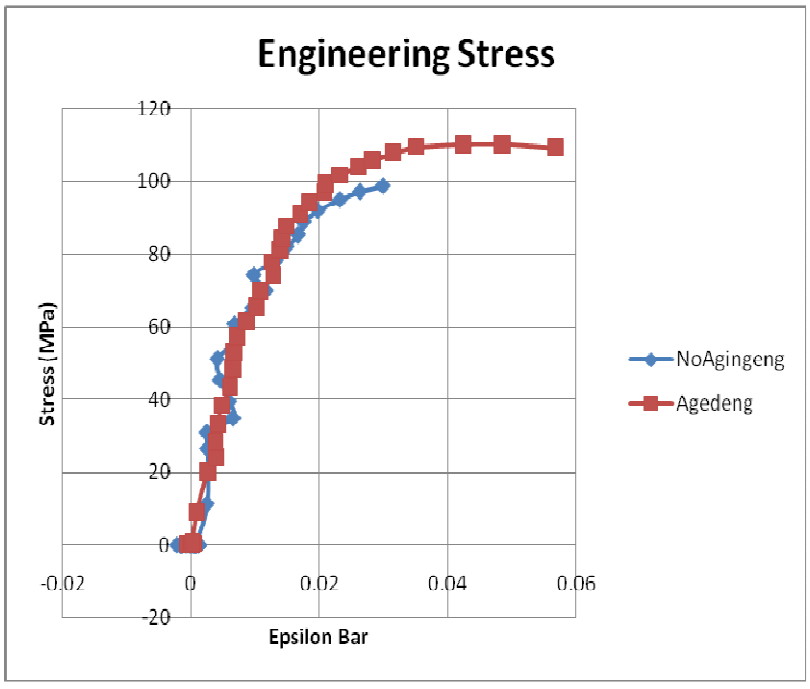

Fig. B-32

ii. Displacement Rate 1e-3 in/s

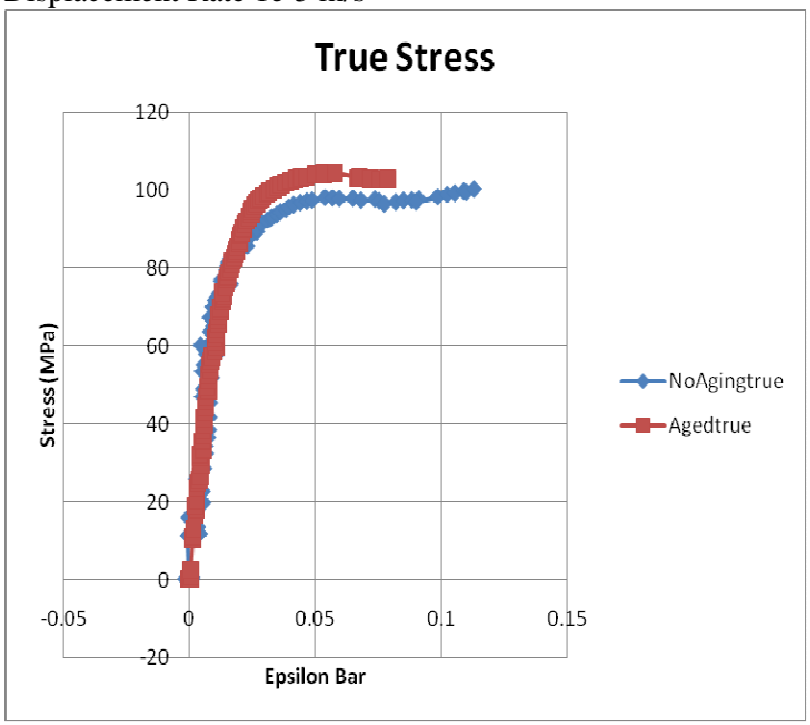

Fig. B-33

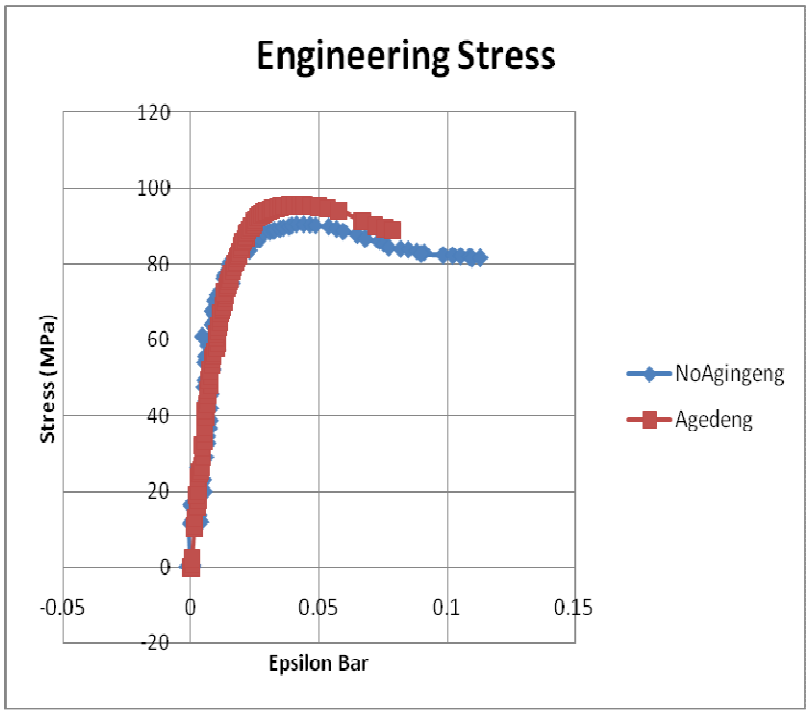

Fig. B-34

iii. Displacement Rate 1e-5 in/s

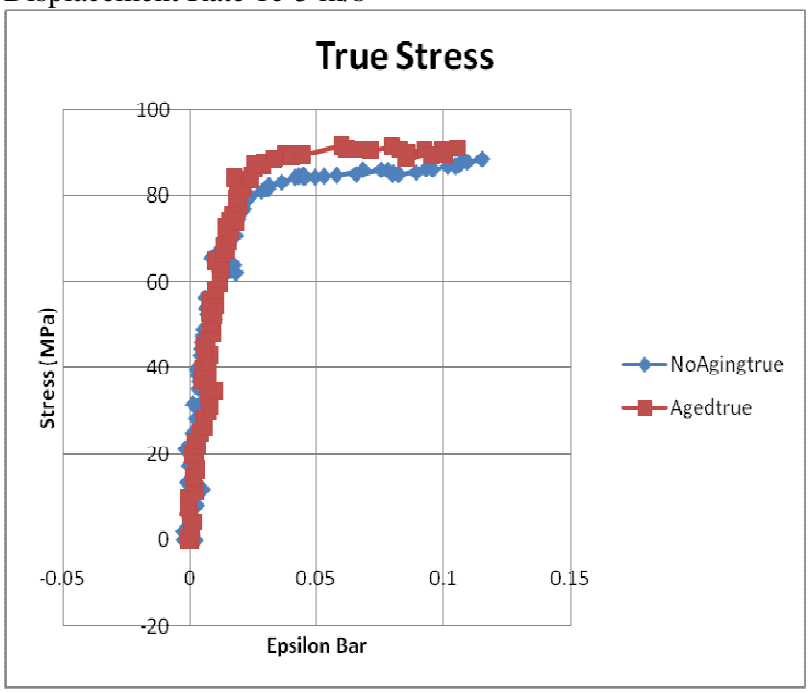

Fig. B-35

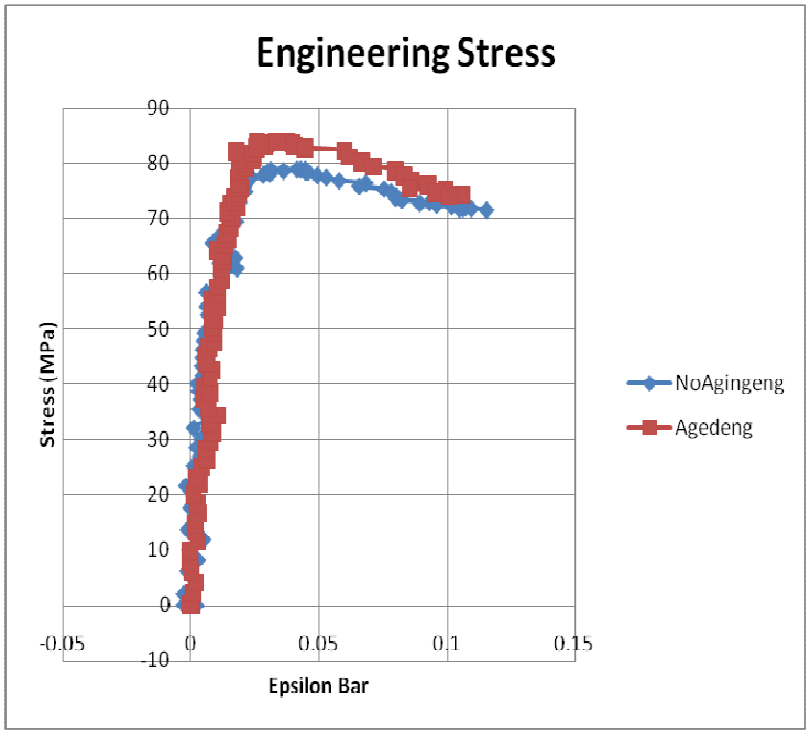

Fig. B-36

II. 50 C
   a. Notch Radius 0.0307 in.
      i. Displacement Rate 1e-1 in/s

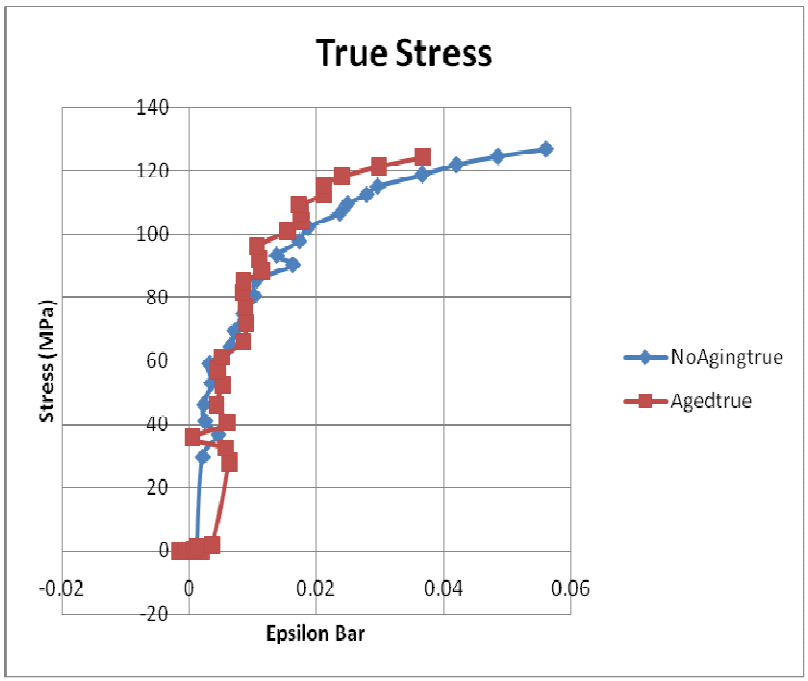

Fig. B-37

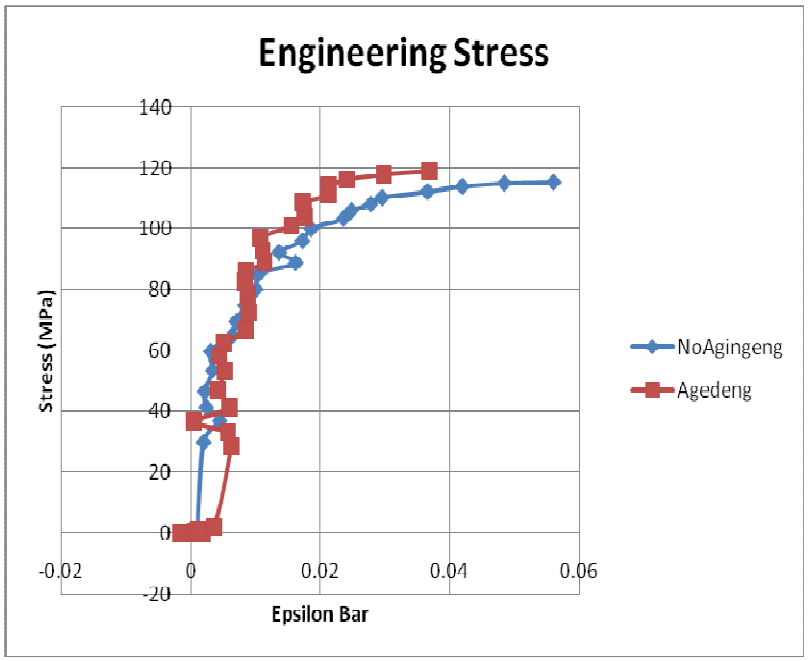

Fig. B-38

ii. Displacement Rate 1e-3 in/s

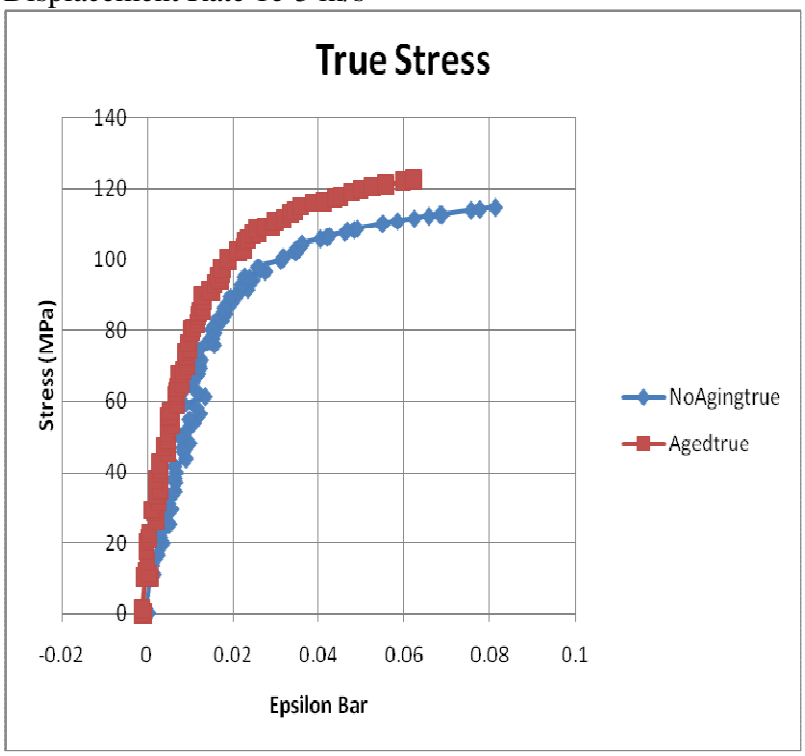

Fig. B-39

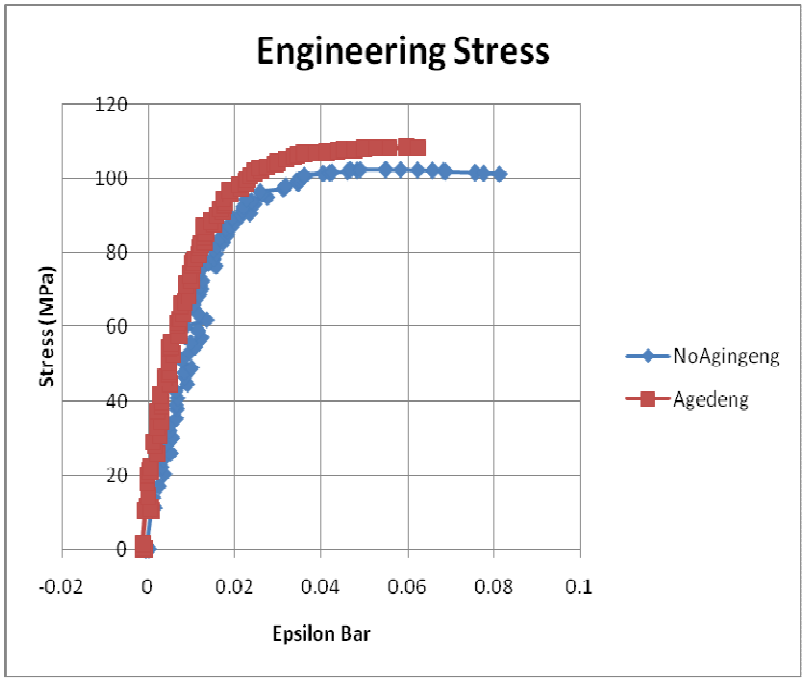

Fig. B-40

b. Notch Radius 0.0614 in.
    i. Displacement Rate 1e-1 in/s

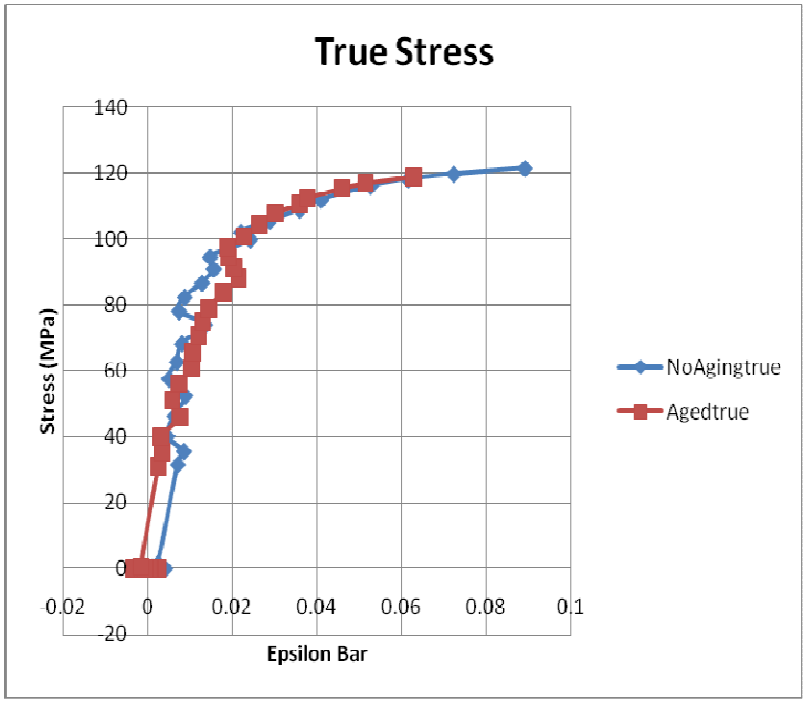

Fig. B-41

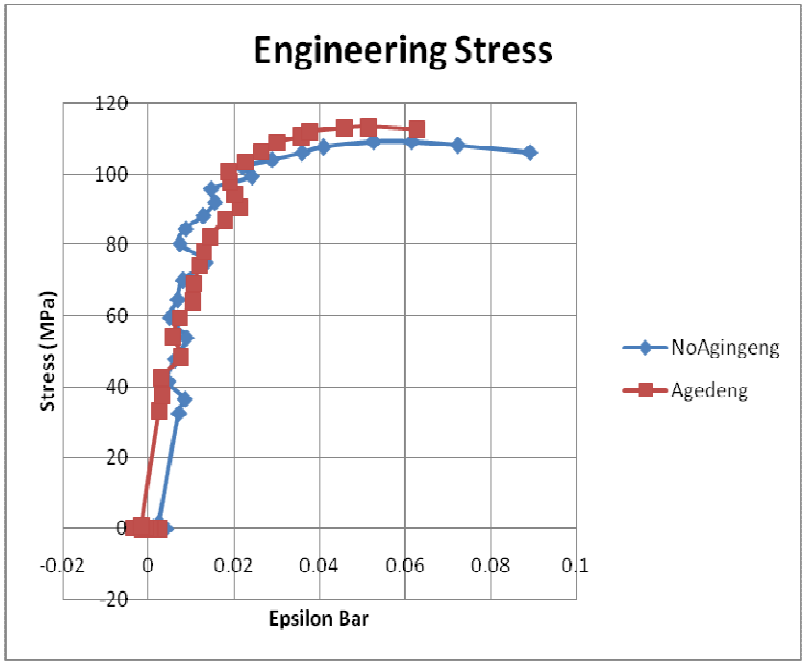

Fig. B-42

ii. Displacement Rate 1e-3 in/s

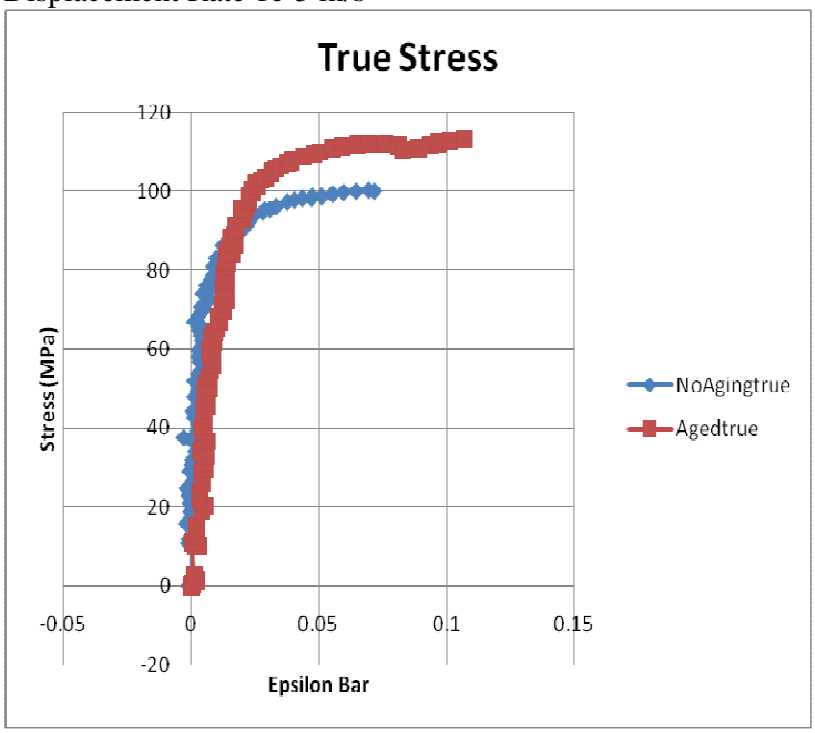

Fig. B-43

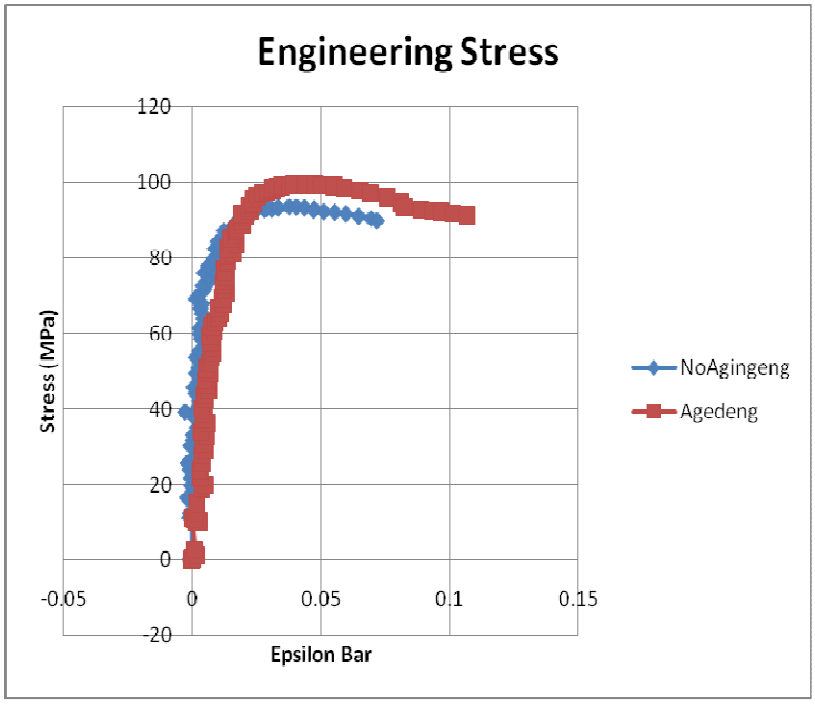

Fig. B-44

c. Notch Radius 0.1535 in.
   i. Displacement Rate 10e-1 in/s

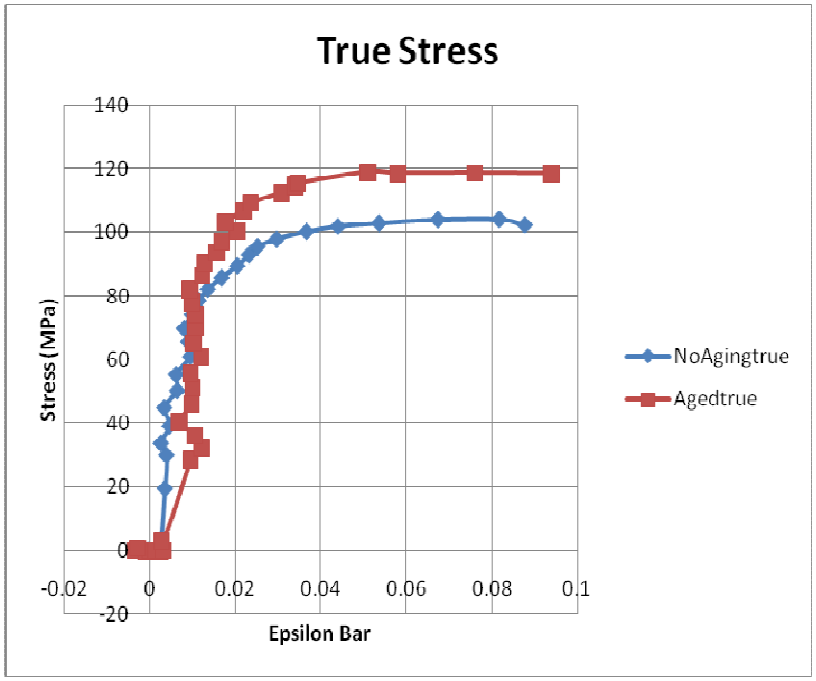

Fig. B-45

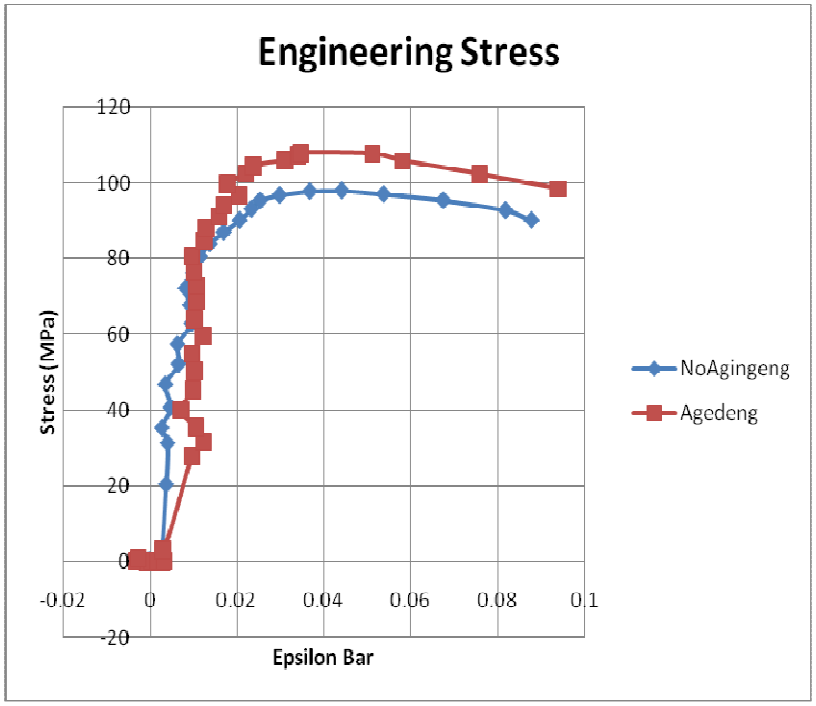

Fig. B-46

ii. Displacement Rate 1e-3 in/s

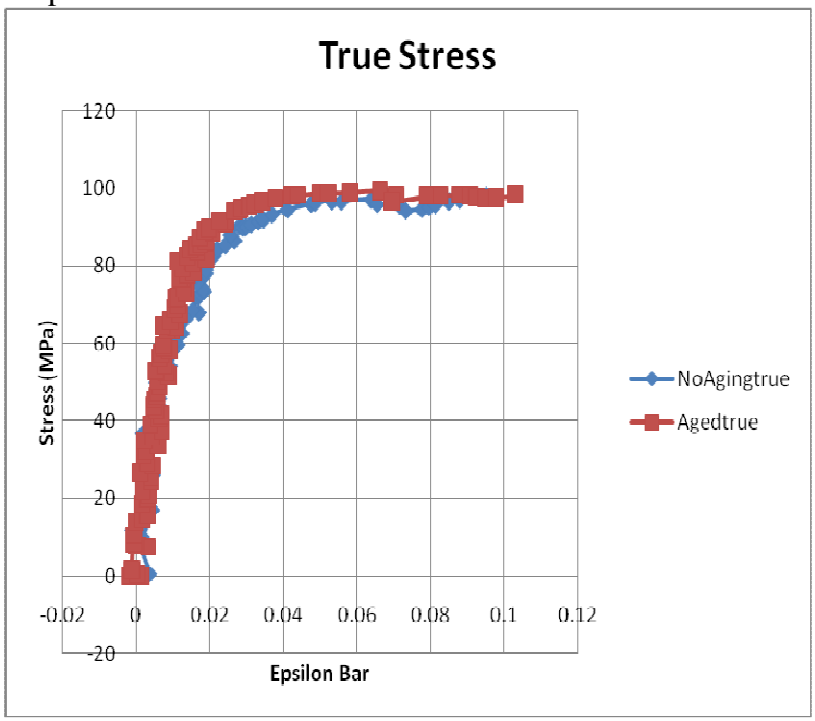

Fig. B-47

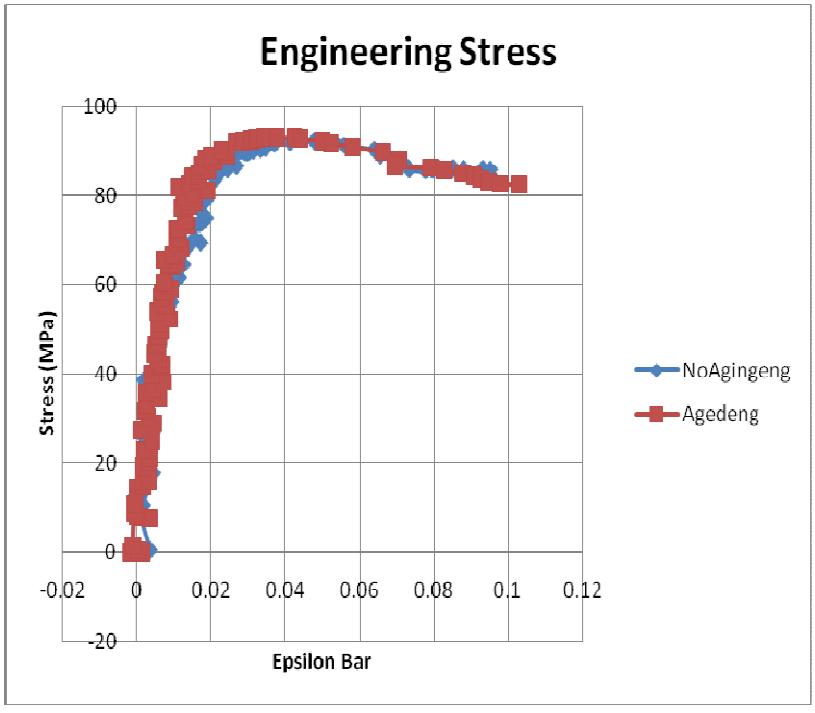

Fig. B-48

III. 80 C

a. Notch Radius 0.0307 in.

i. Displacement Rate 1e-1 in/s

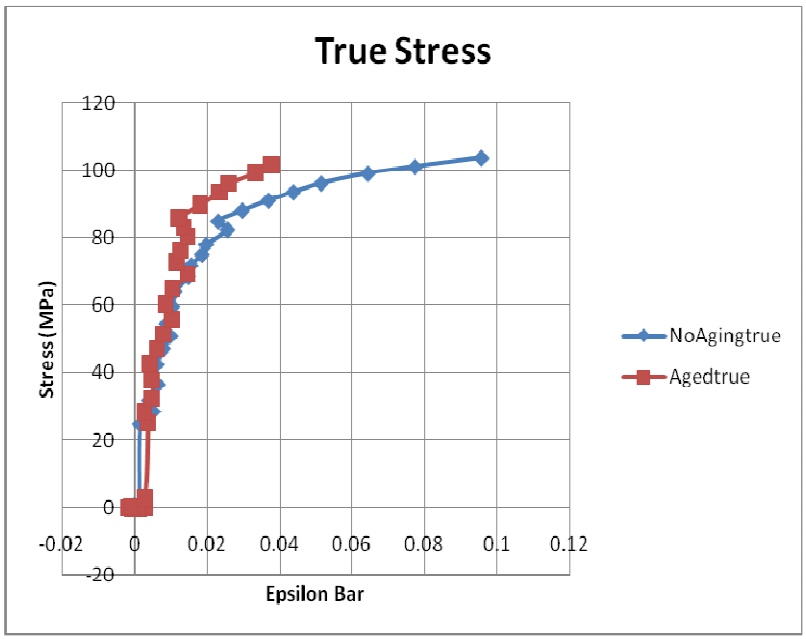

Fig. B-49

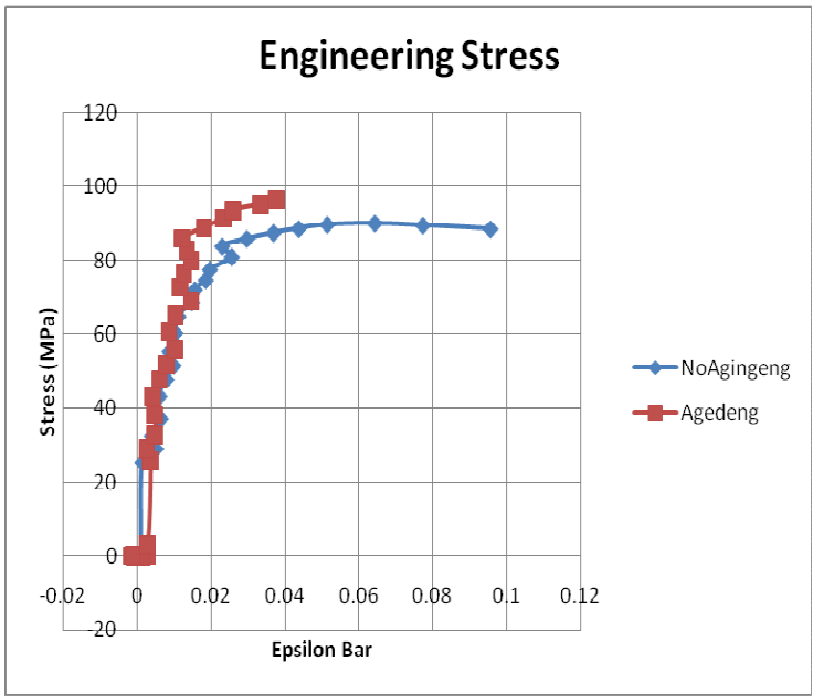

Fig. B-50

ii. Displacement Rate 1e-3 in/s

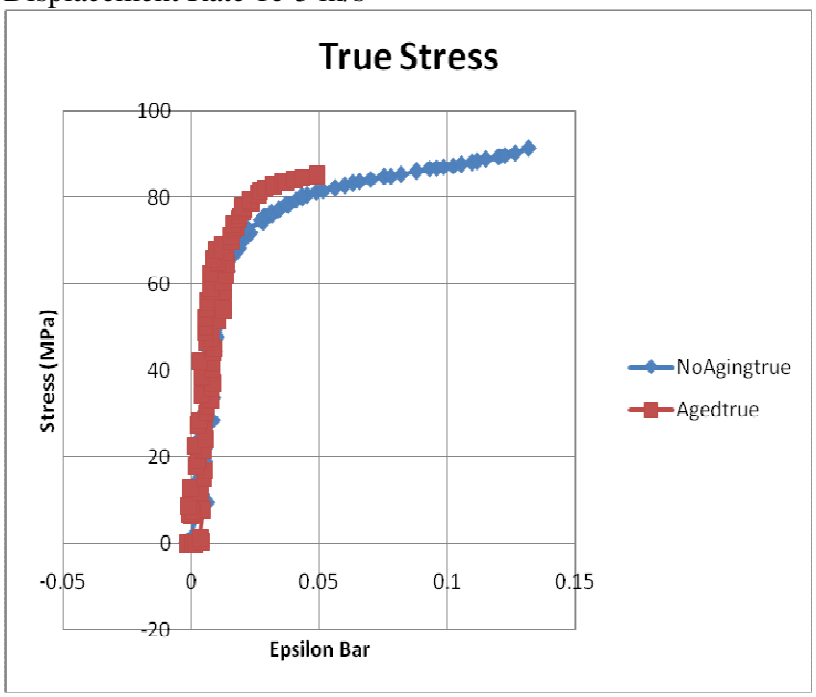

Fig. B-51

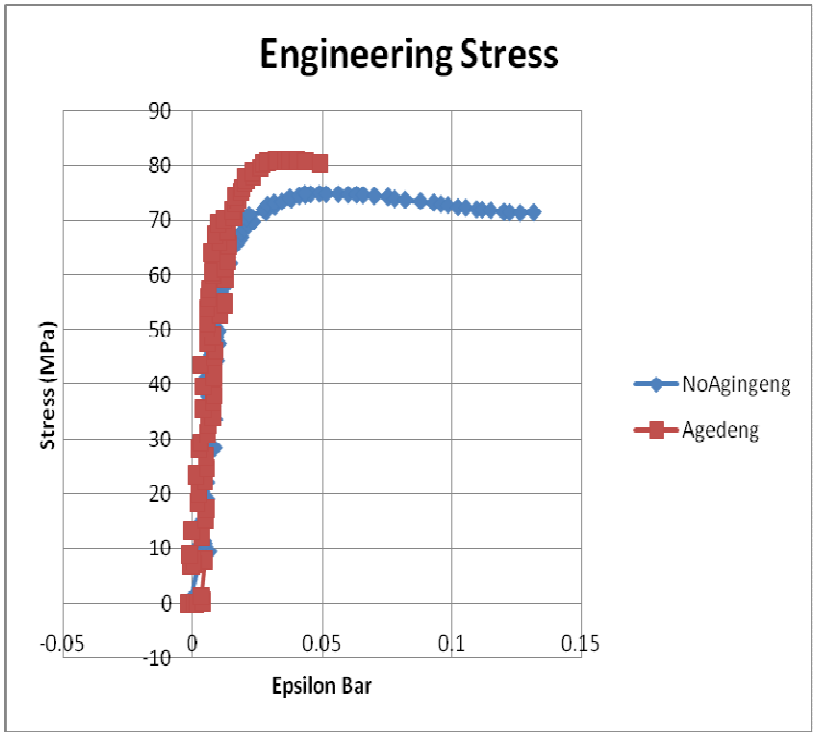

Fig. B-52

b. Notch Radius 0.0614 in.
    i. Displacement Rate 1e-1 in/s

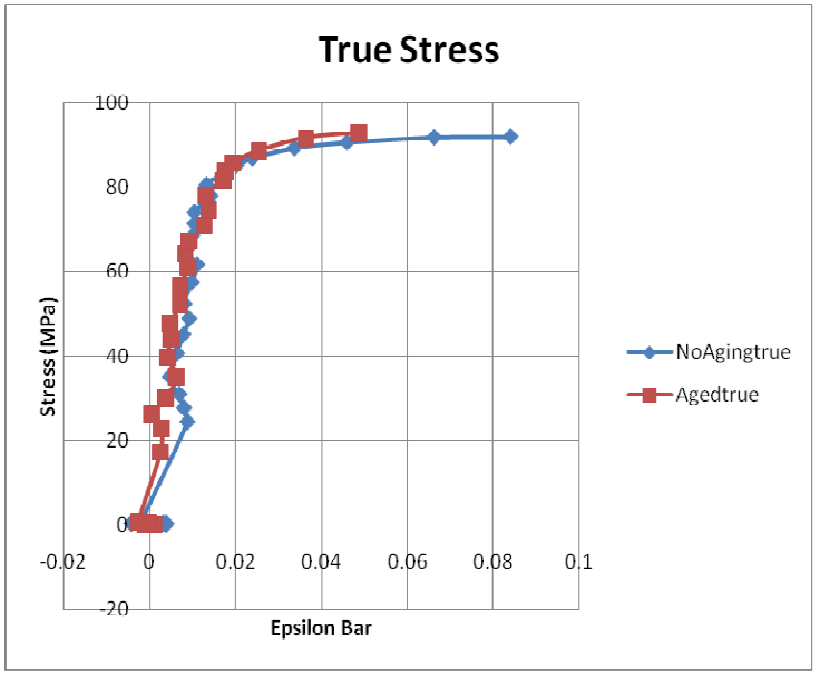

Fig. B-53

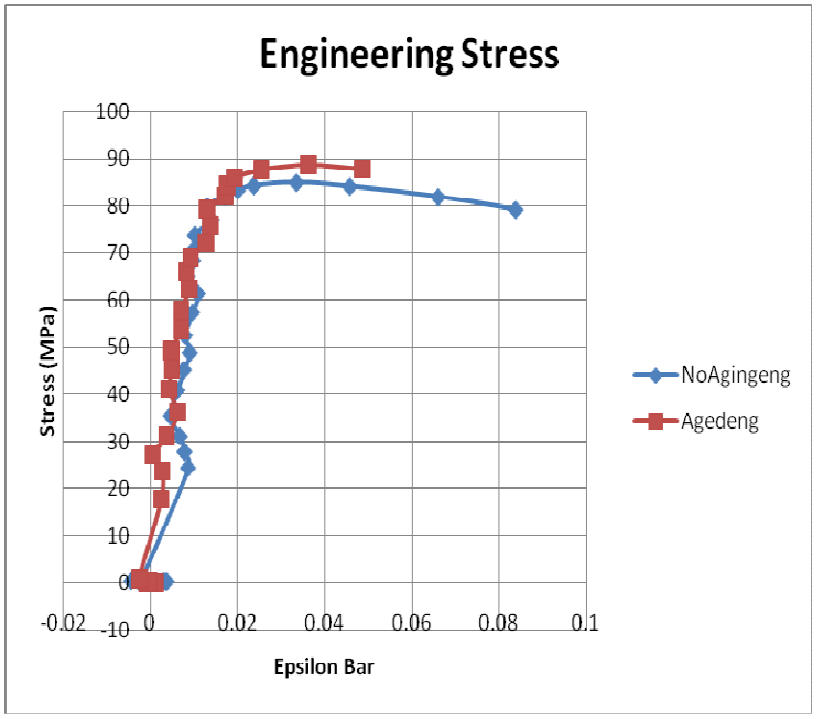

Fig. B-54

ii. Displacement Rate 1e-3 in/s

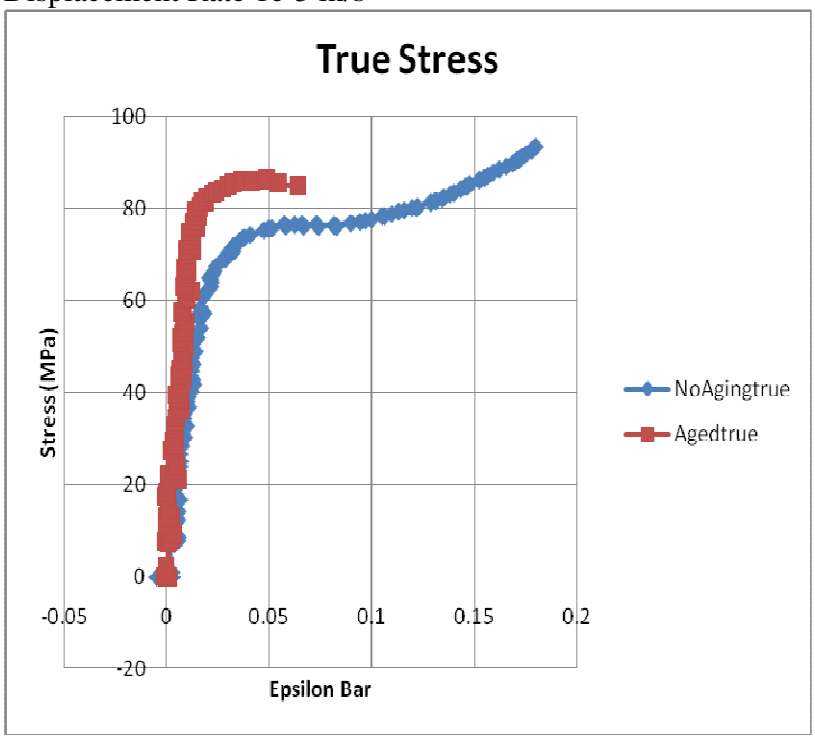

Fig. B-55

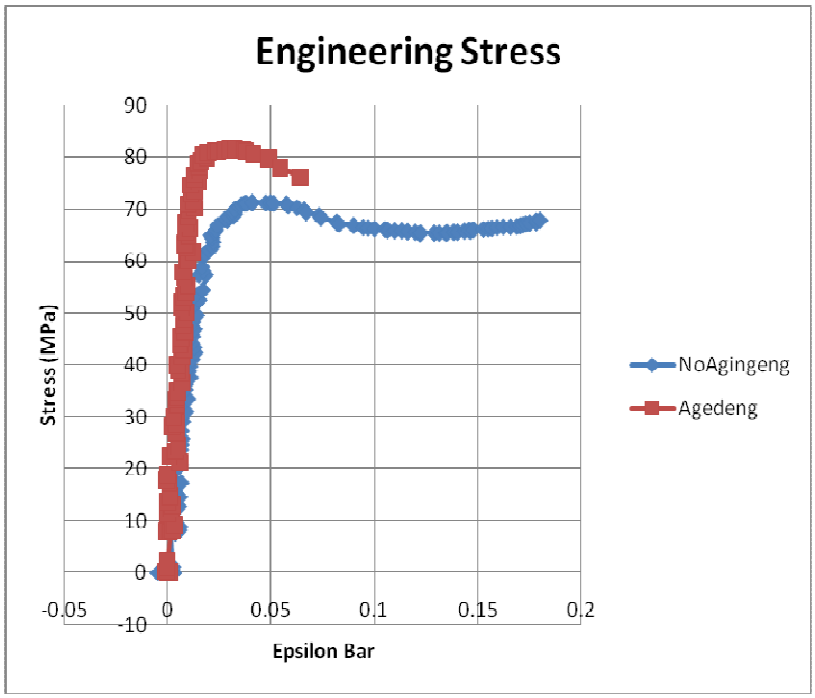

Fig. B-56

c. Notch Radius 0.1535 in.
   i. Displacement Rate 1e-1 in/s

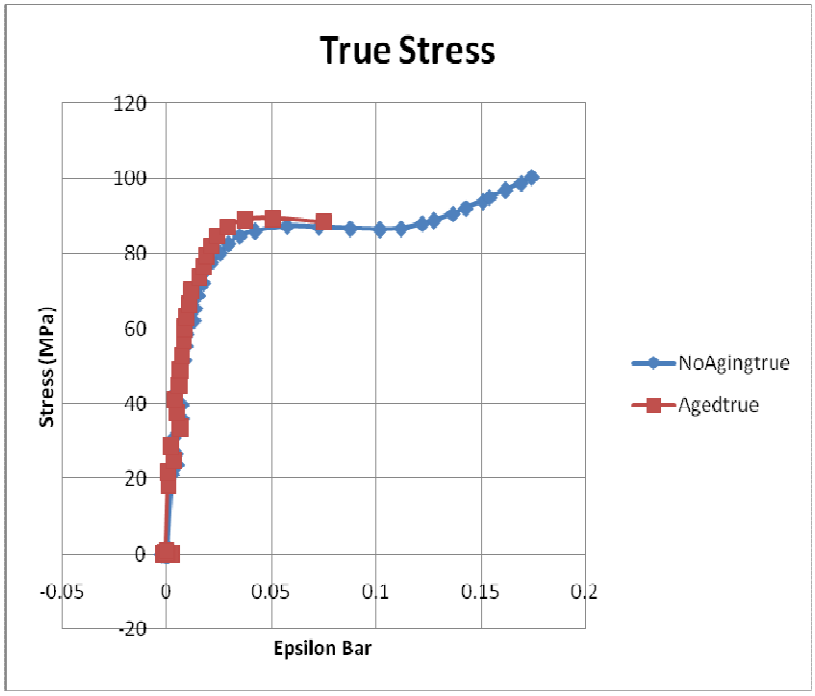

Fig. B-57

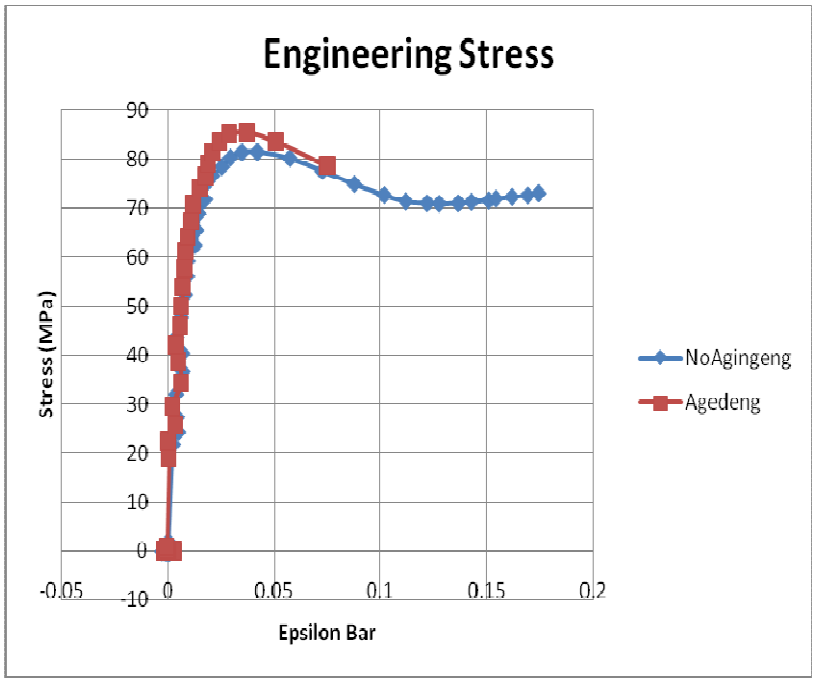

Fig. B-58

ii. Displacement Rate 1e-3 in/s

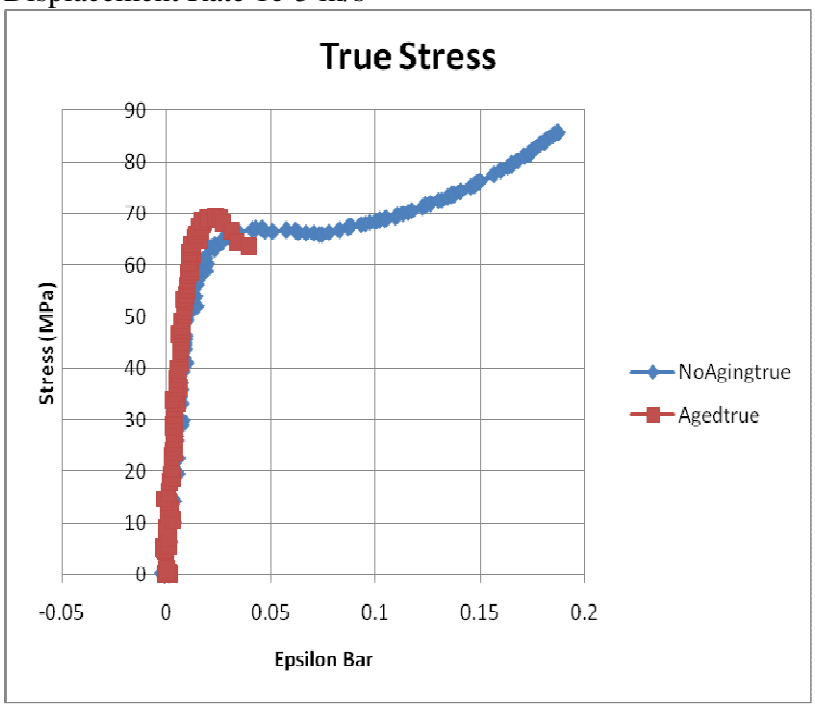

Fig. B-59

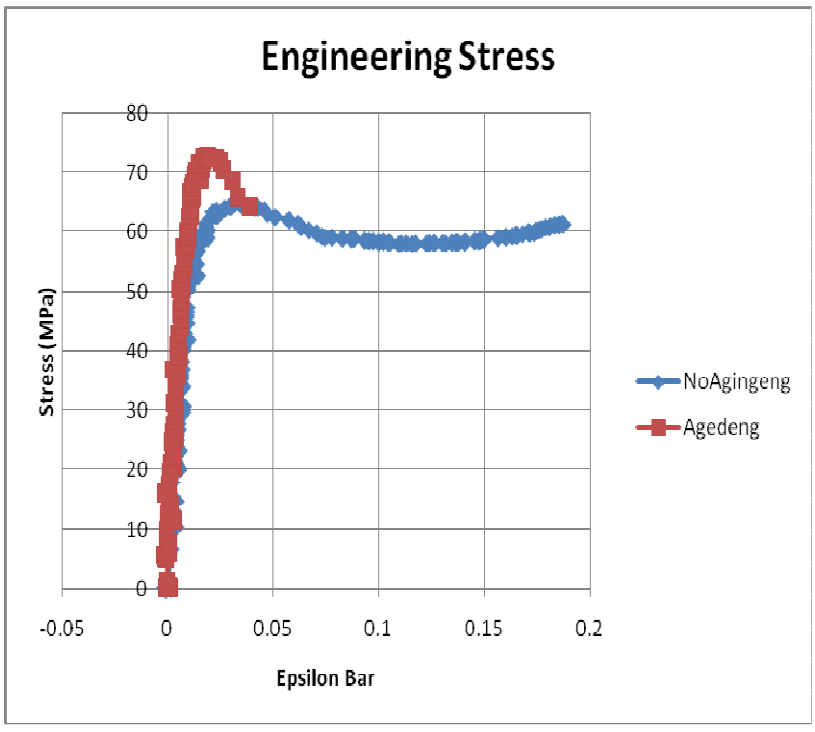

Fig. B-60

APPENDIX C

NOTCH RADIUS COMPARISON DATA

I. Room Temperature
   a. No Aging
      i. Displacement Rate 1e-1 in/s

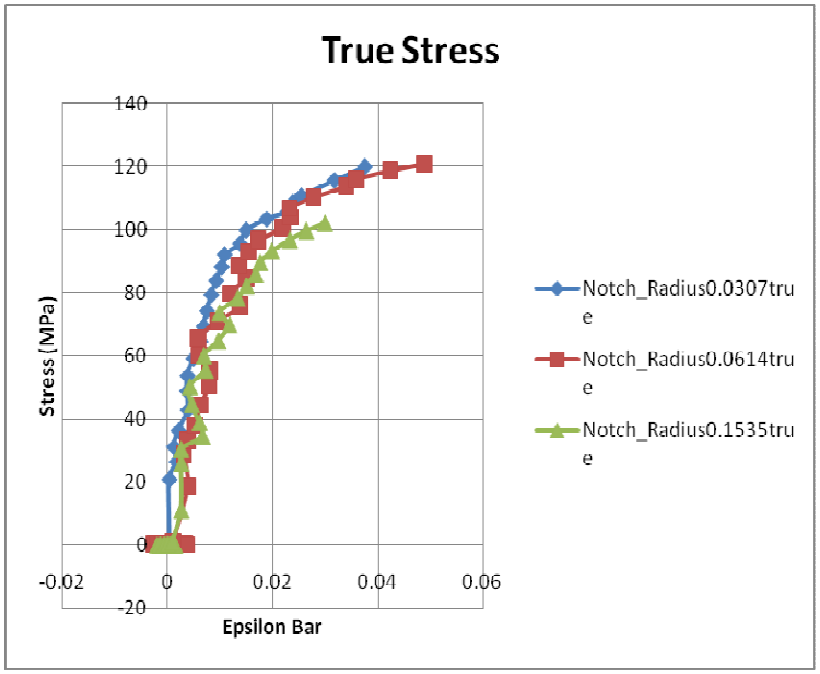

Fig. C-61

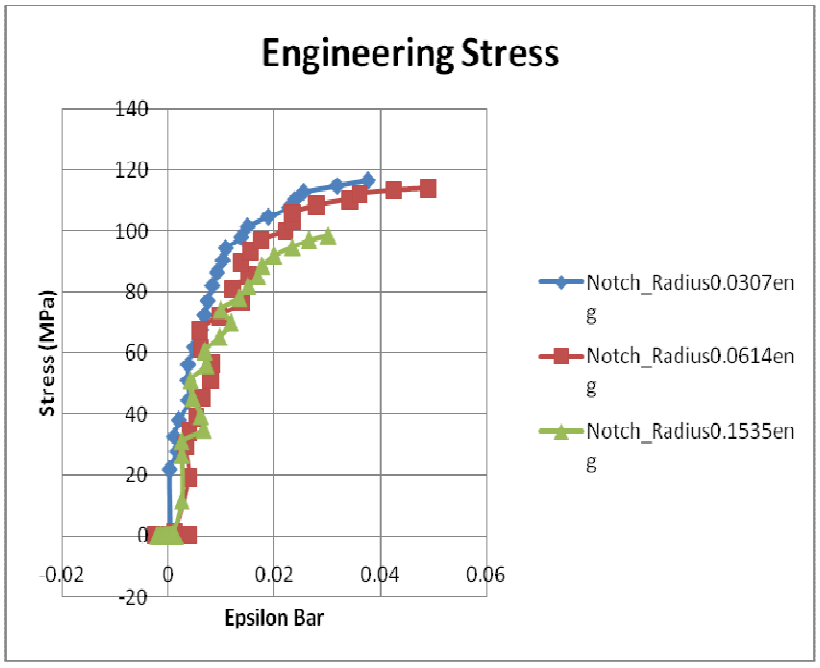

Fig. C-62

ii. Displacement Rate 1e-3 in/s

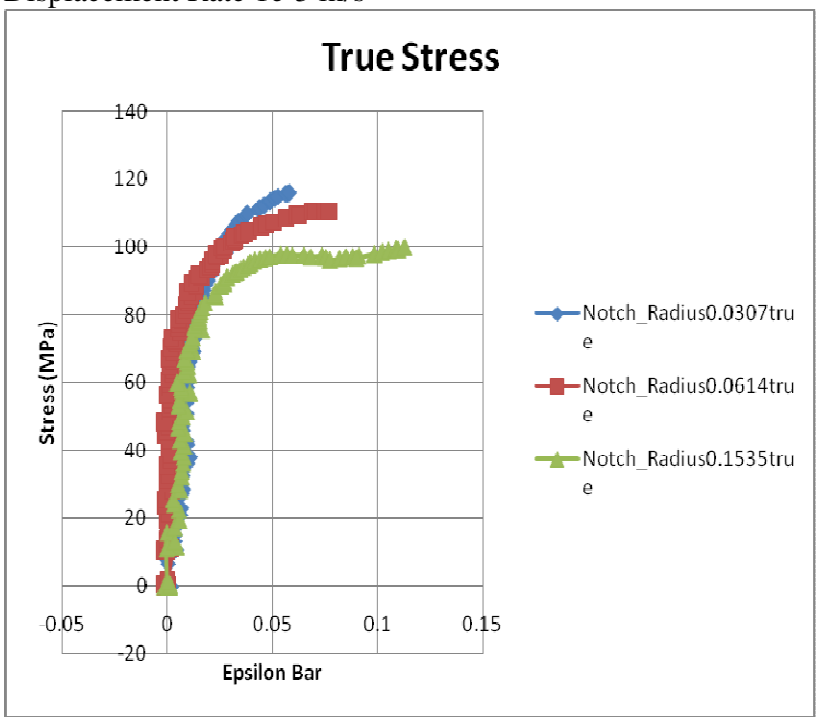

Fig. C-63

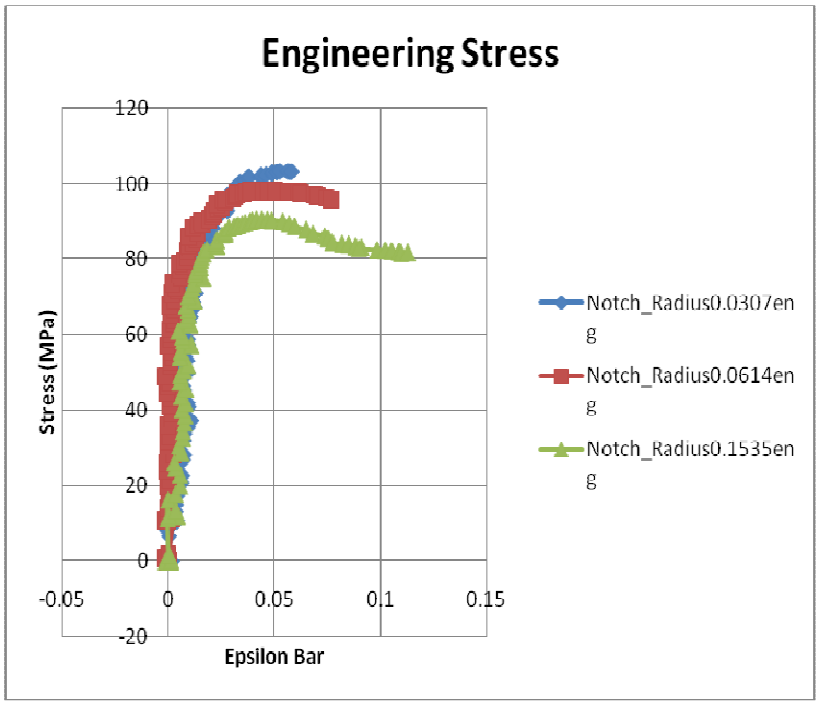

Fig. C-64

iii. Displacement Rate 1e-5 in/s

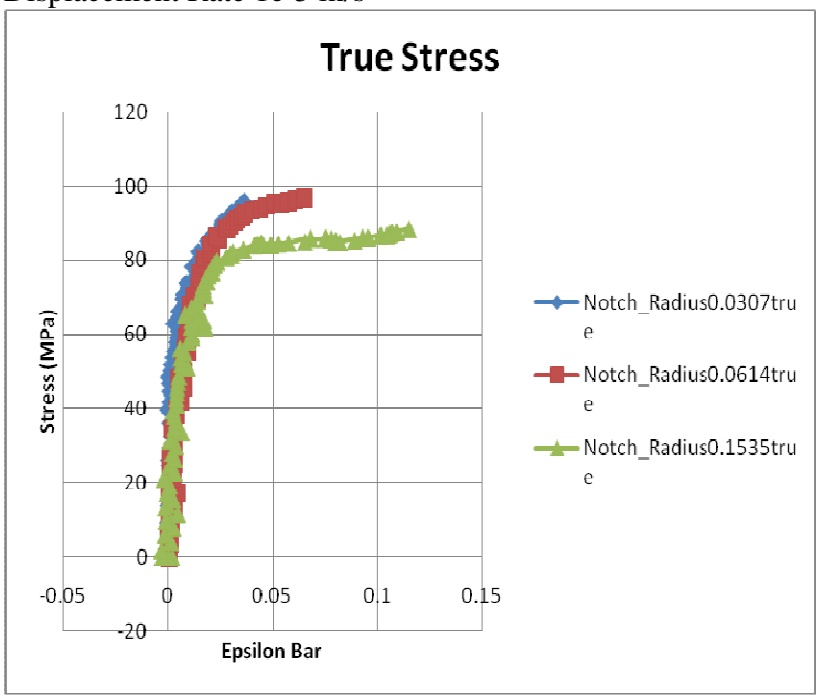

Fig. C-65

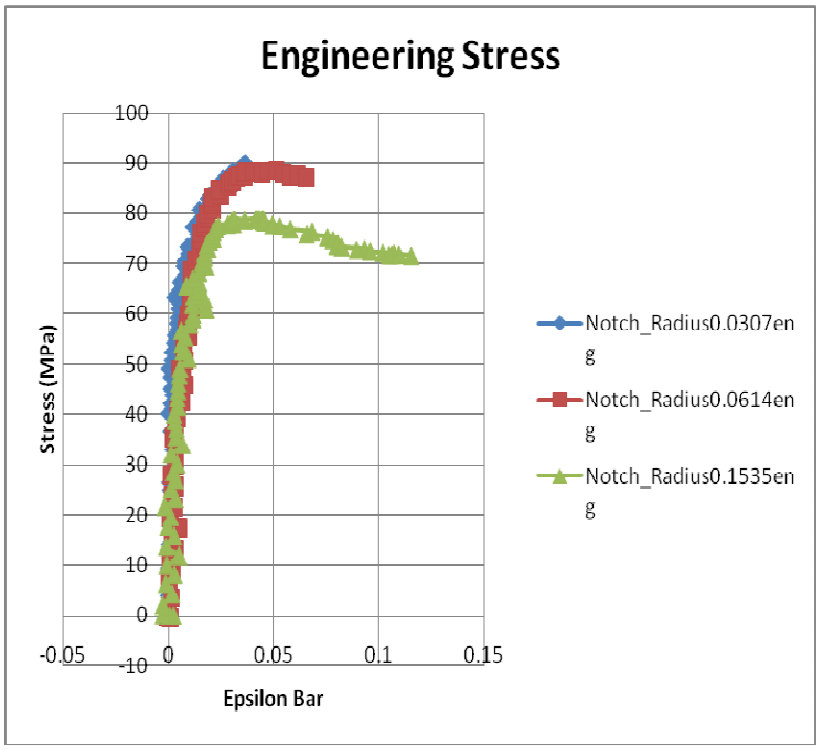

Fig. C-66

b. Aged

i. Displacement Rate 1e-1 in/s

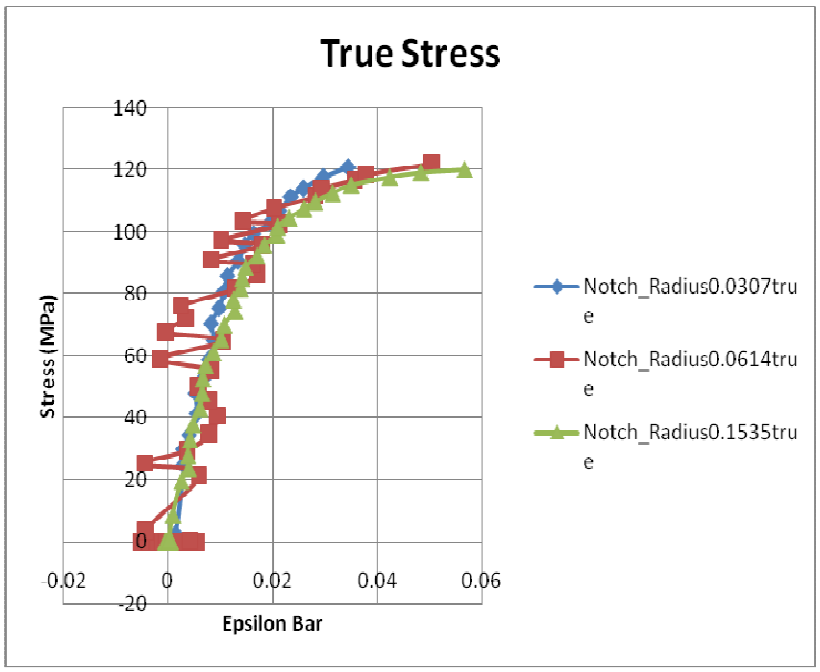

Fig. C-67

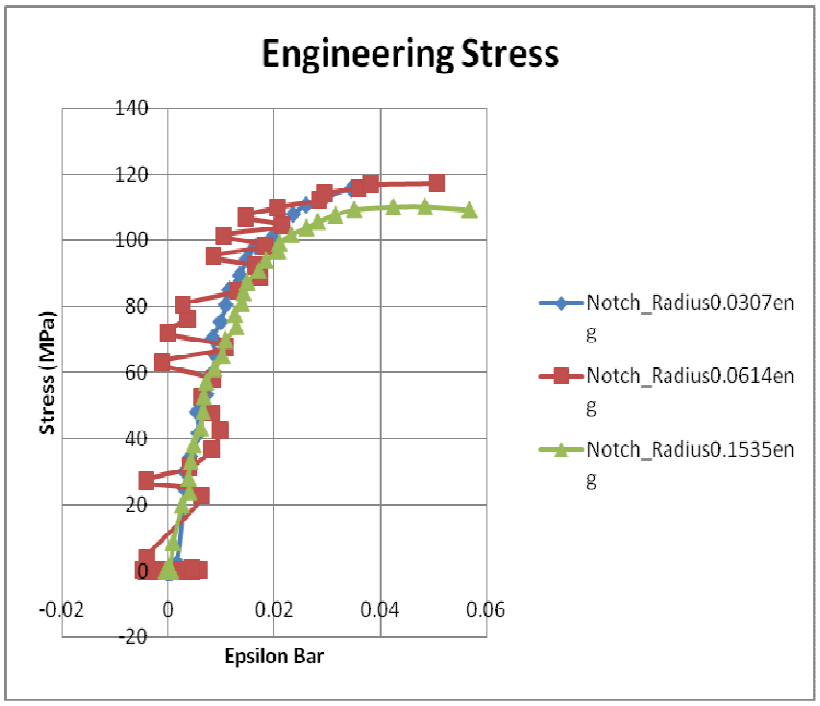

Fig. C-68

ii. Displacement Rate 1e-3 in/s

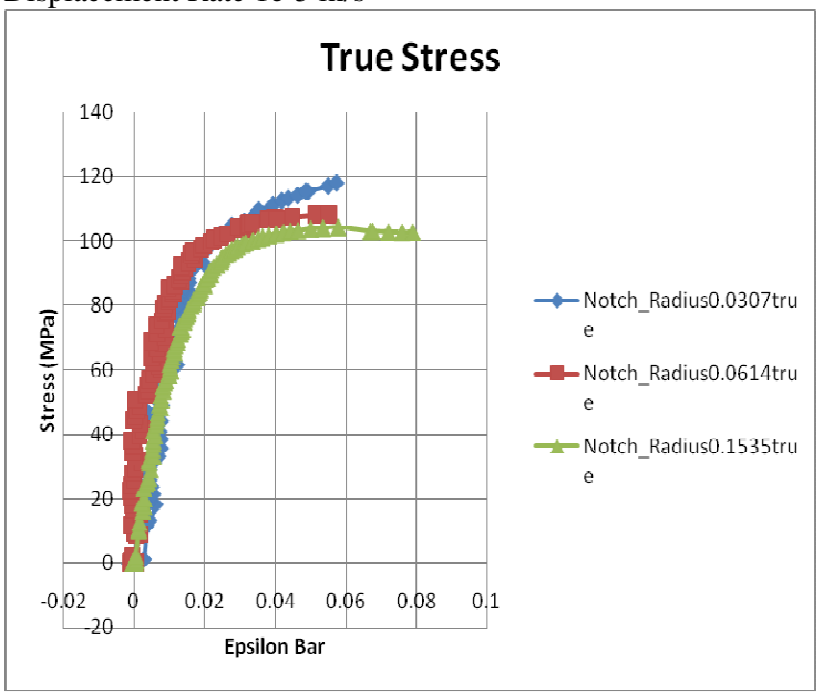

Fig. C-69

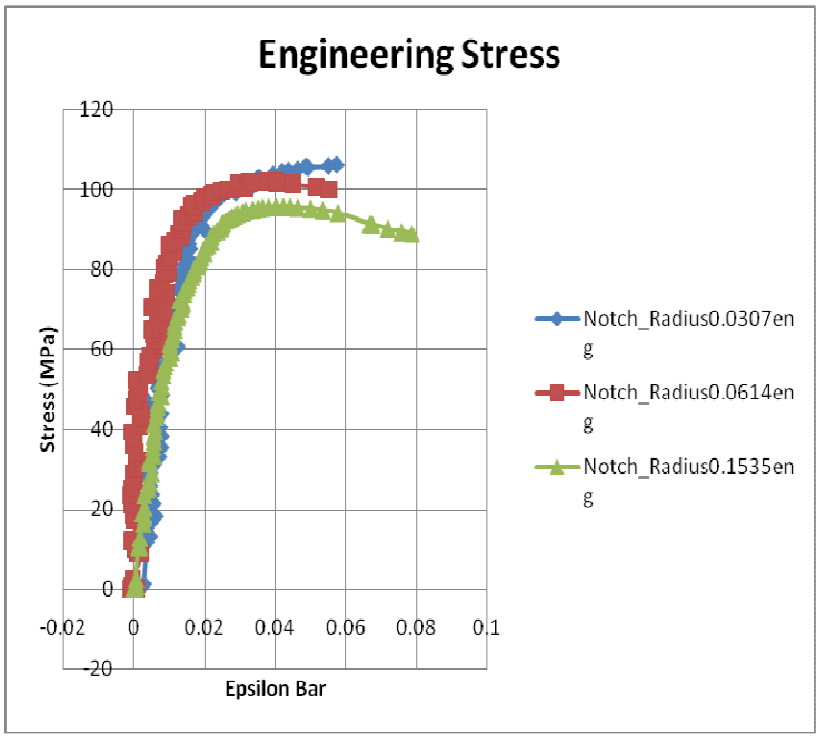

Fig. C-70

iii. Displacement Rate 1e-5 in/s

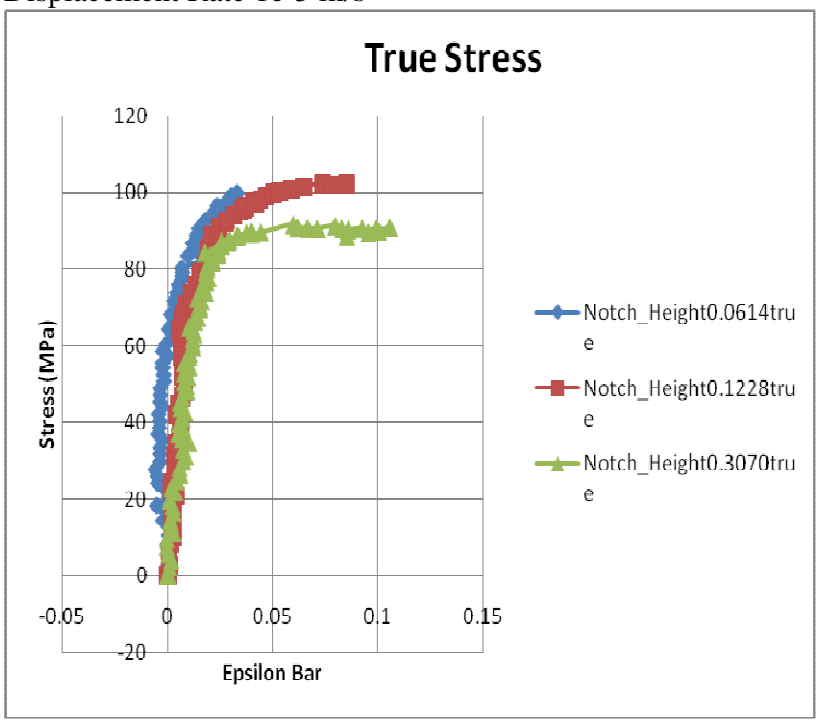

Fig. C-71

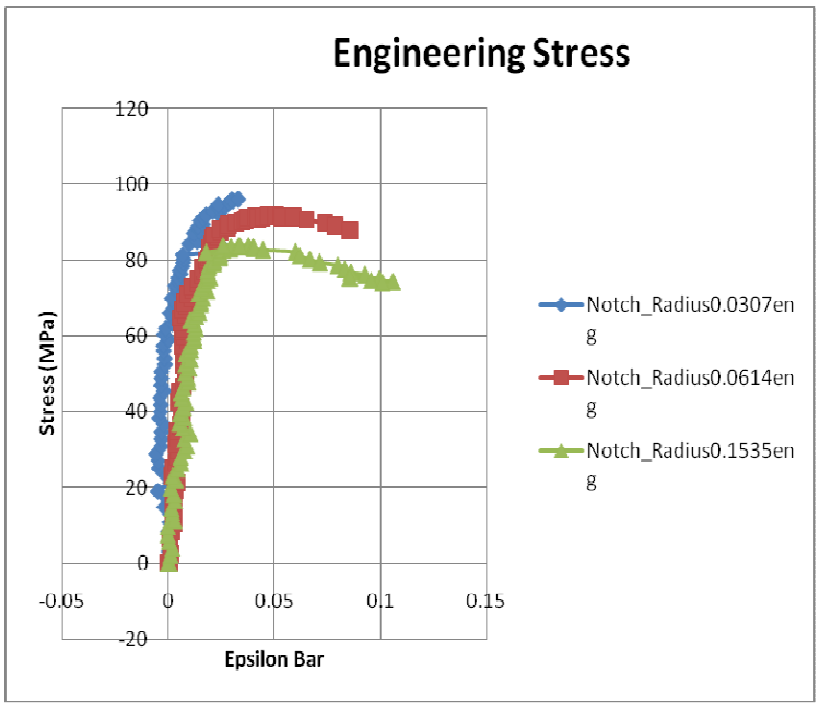

Fig. C-72

II. 50 C
   a. No Aging
      i. Displacement Rate 1e-1 in/s

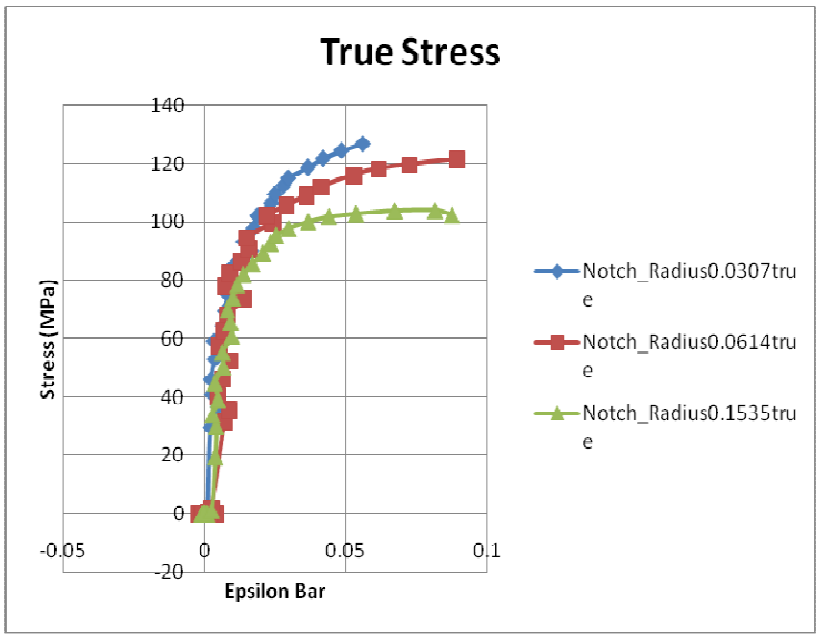

Fig. C-73

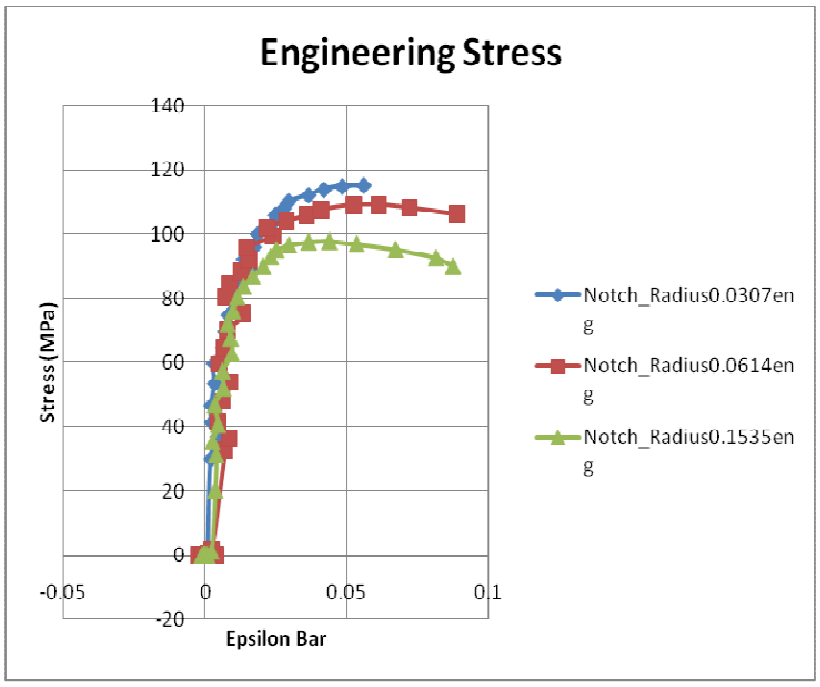

Fig. C-74

ii. Displacement Rate 1e-3 in/s

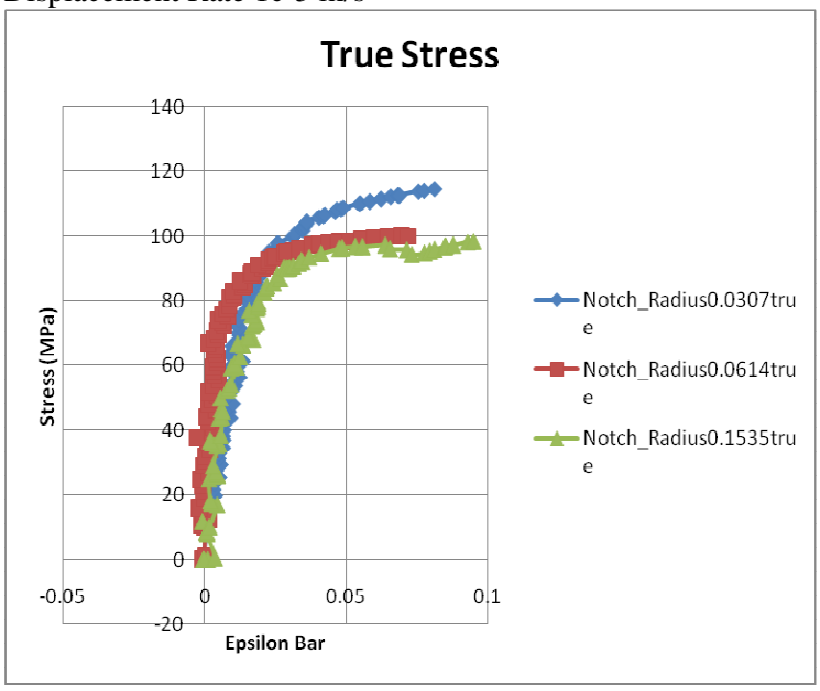

Fig. C-75

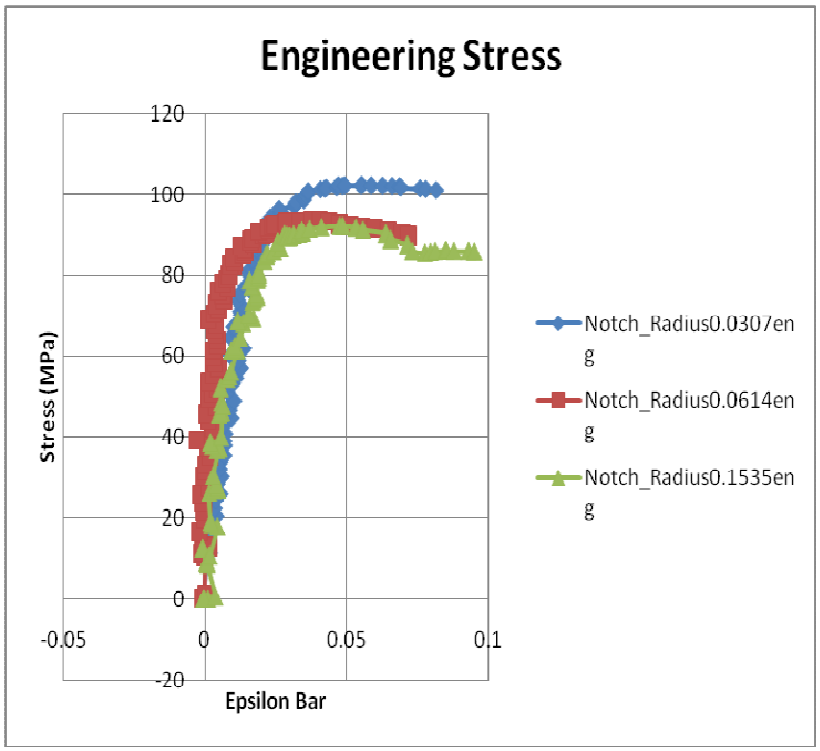

Fig. C-76

b. Aged

i. Displacement Rate 1e-1 in/s

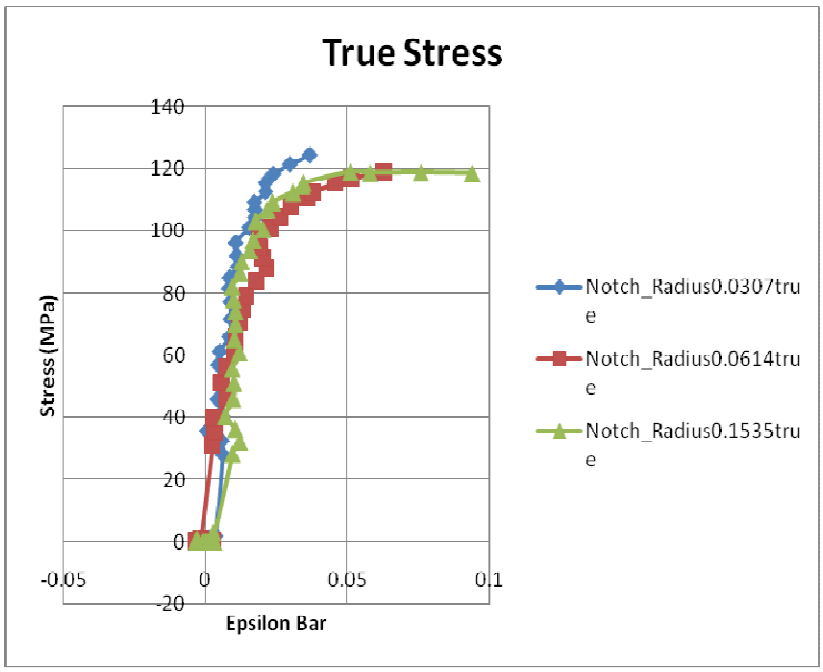

Fig. C-77

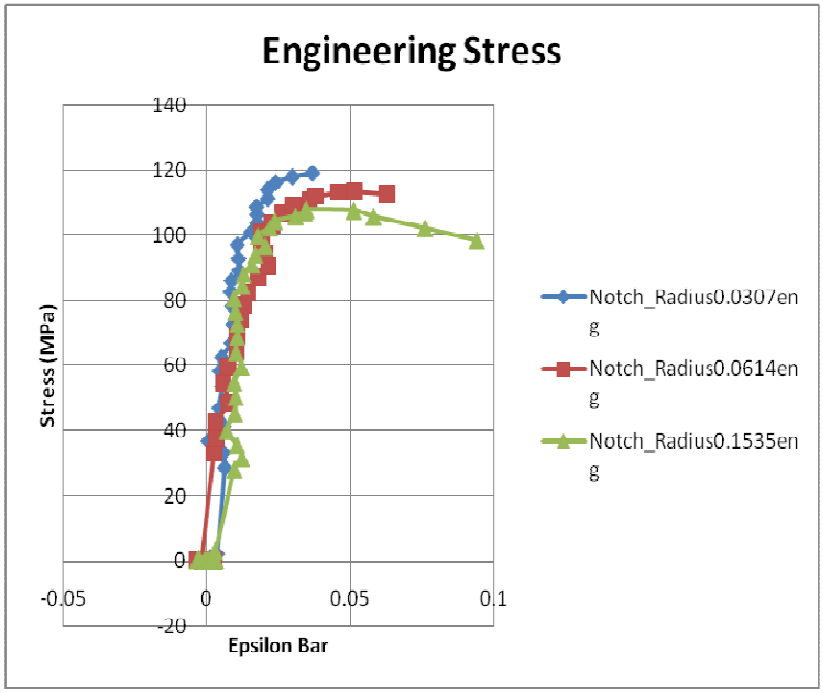

Fig. C-78

ii. Displacement Rate 1e-3 in/s

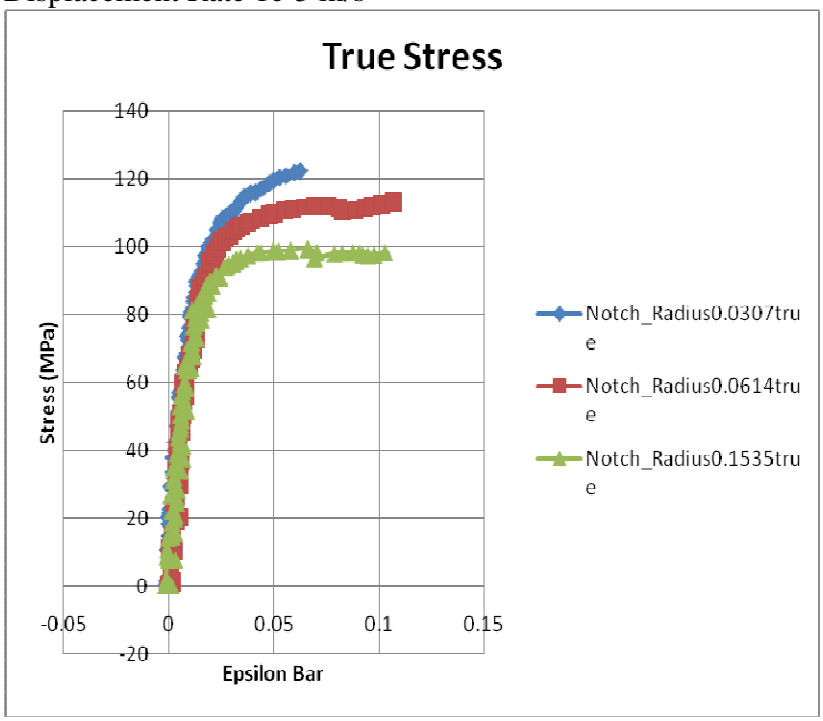

Fig. C-79

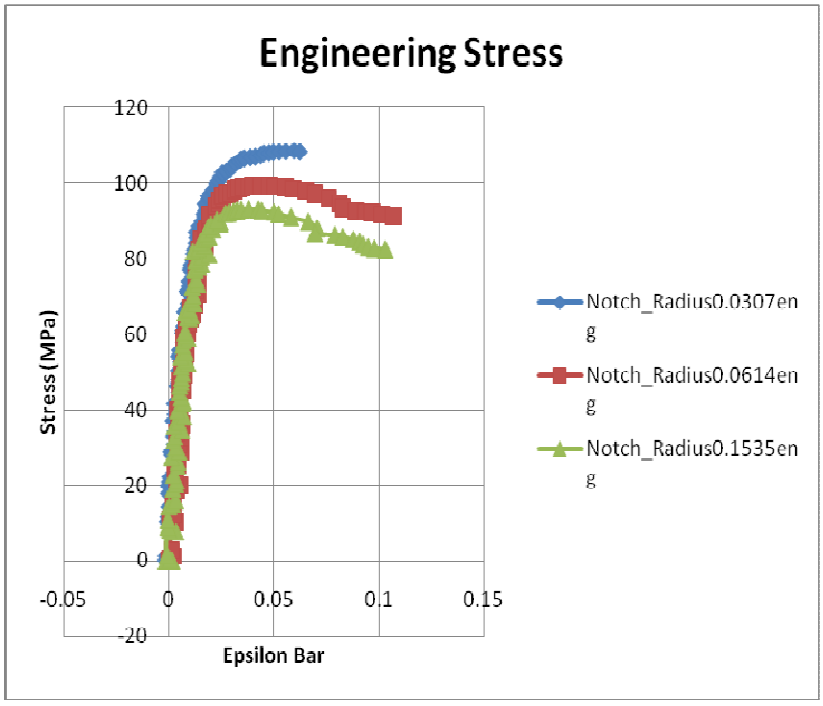

Fig. C-80

III. 80 C

a. No Aging

i. Displacement Rate 1e-1 in/s

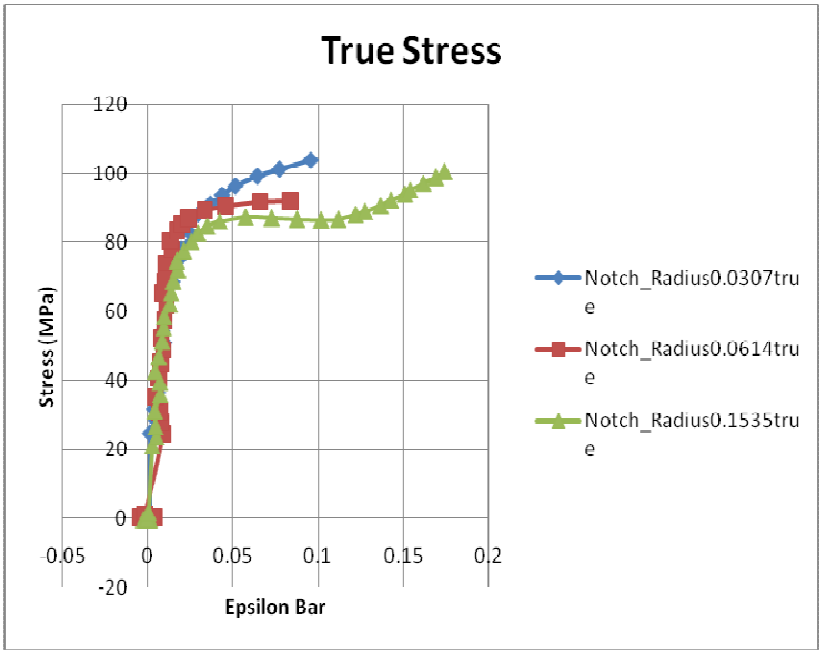

Fig. C-81

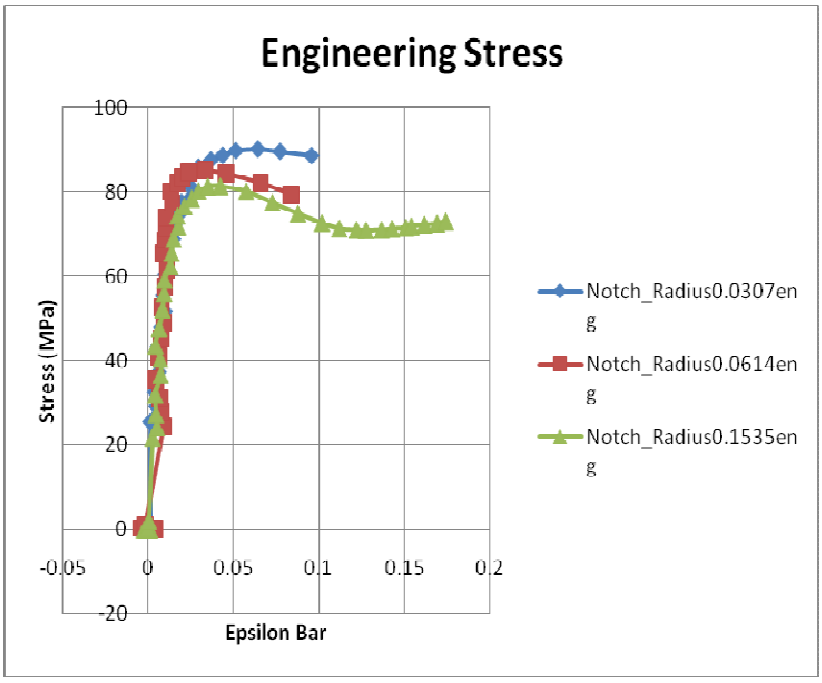

Fig. C-82

ii. Displacement Rate 1e-3 in/s

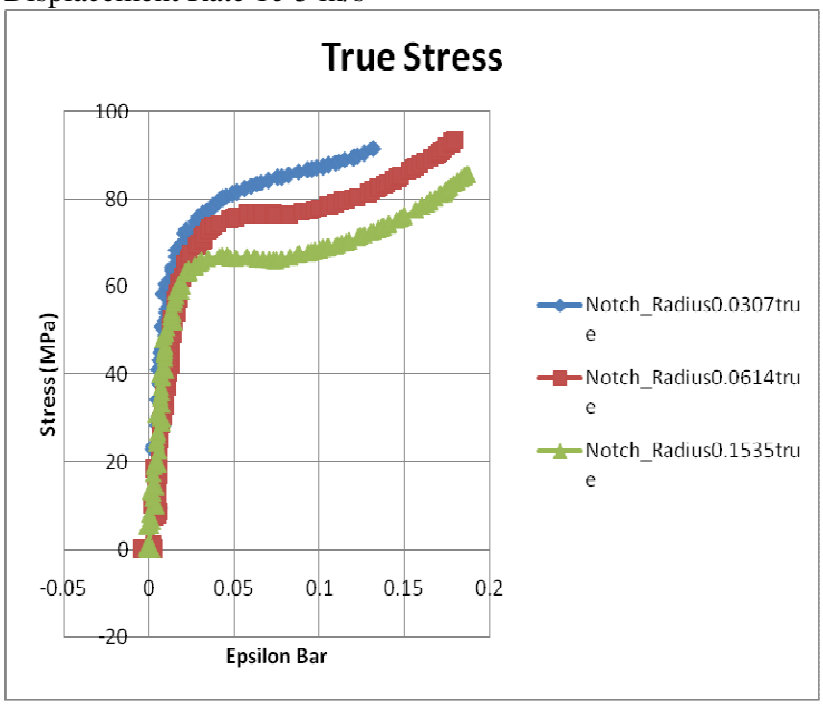

Fig. C-83

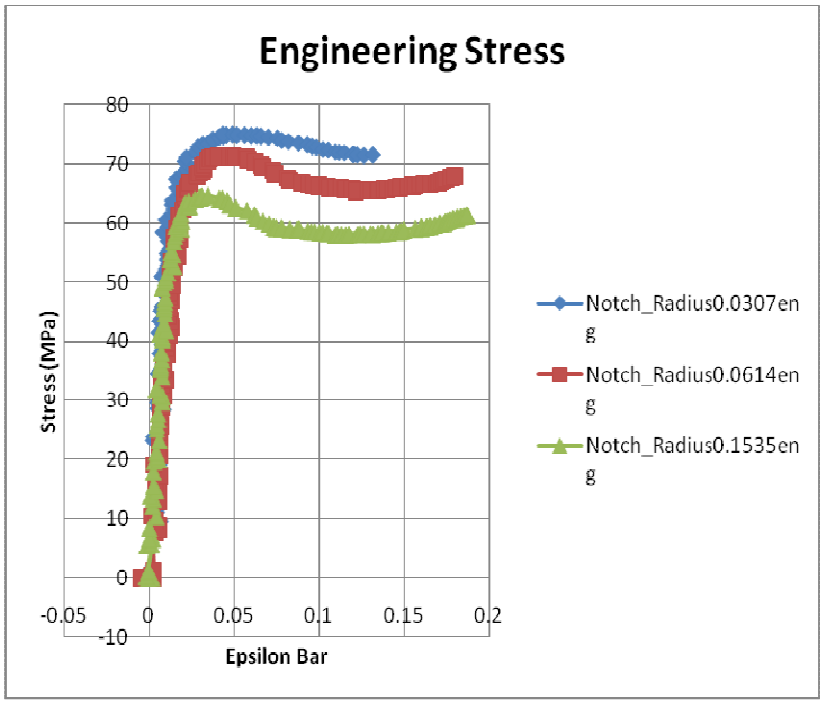

Fig. C-84

b. Aged

i. Displacement Rate 1e-1 in/s

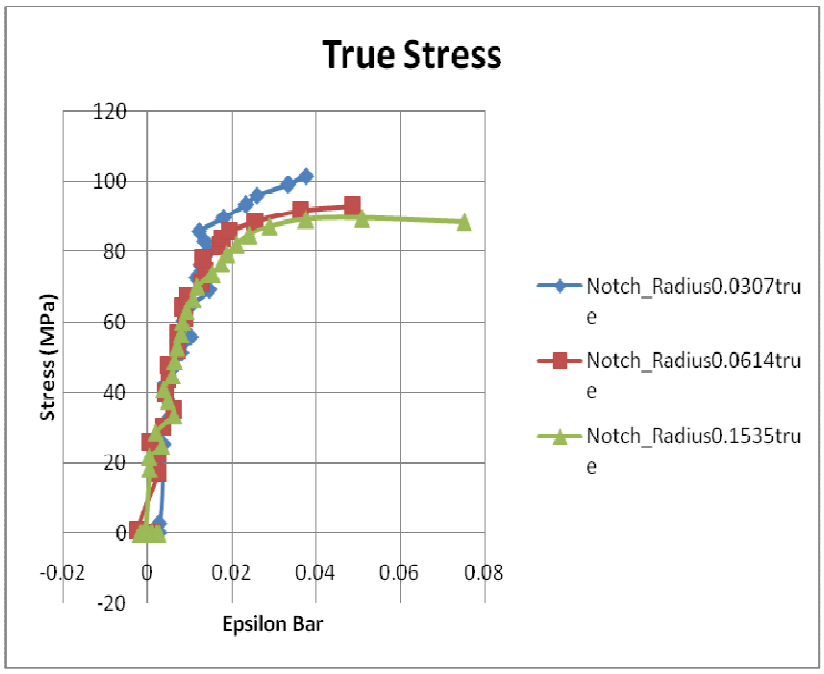

Fig. C-85

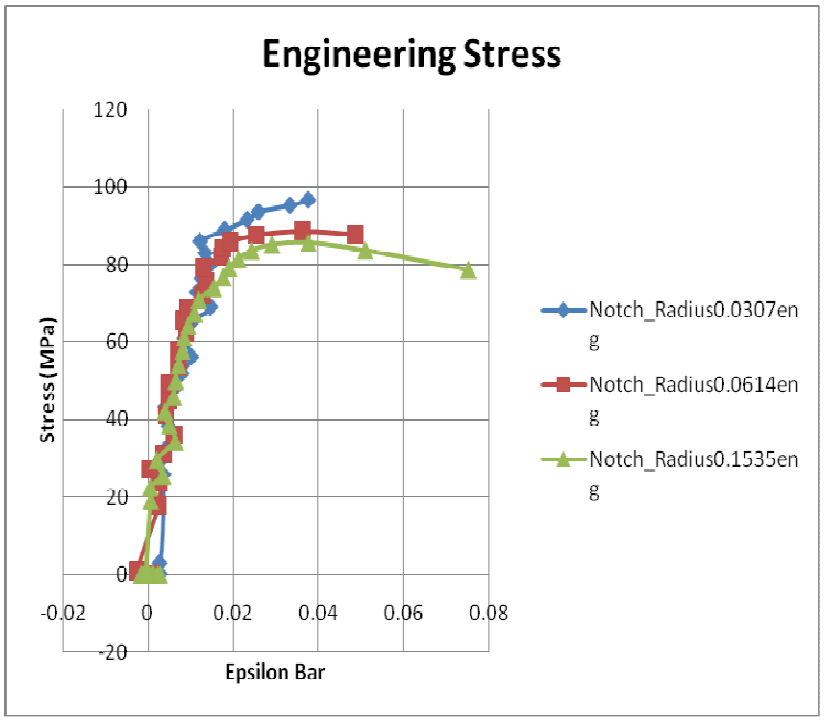

Fig. C-86

ii. Displacement Rate 1e-3 in/s

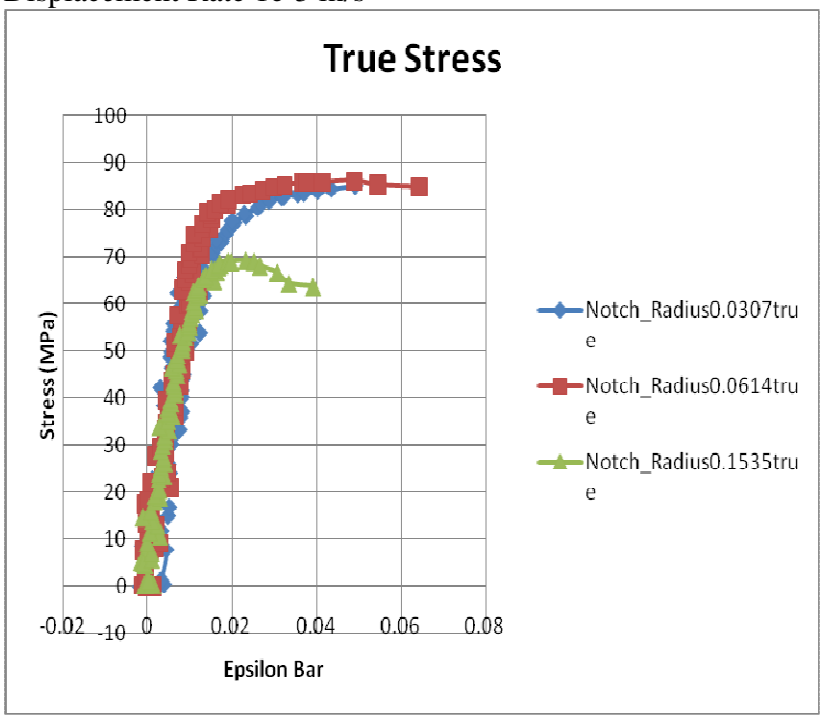

Fig. C-87

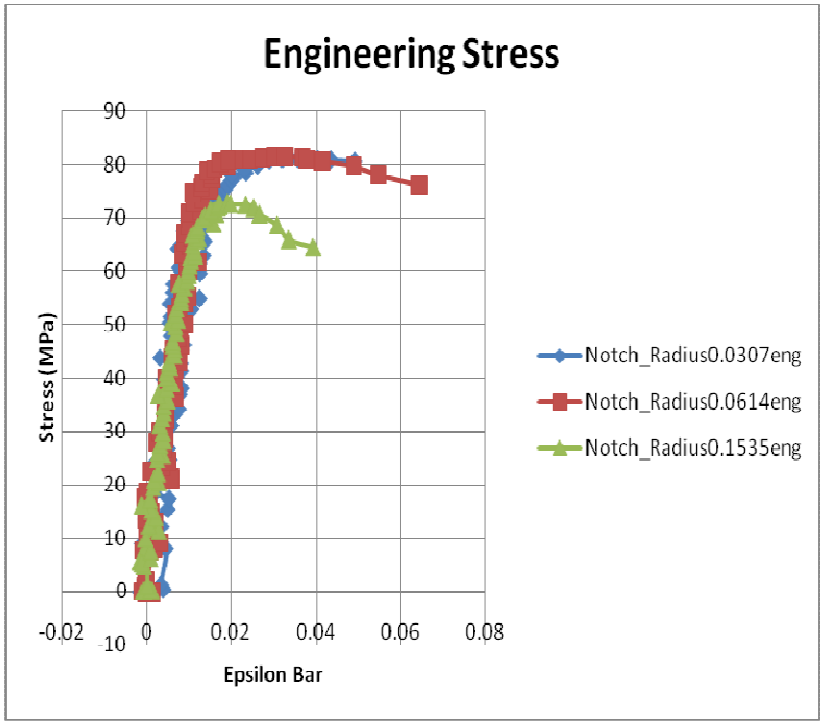

Fig. C-88

APPENDIX D

TEMPERATURE COMPARISON DATA

I. Notch Radius 0.0307 in.
   a. Displacement Rate 1e-1 in/s

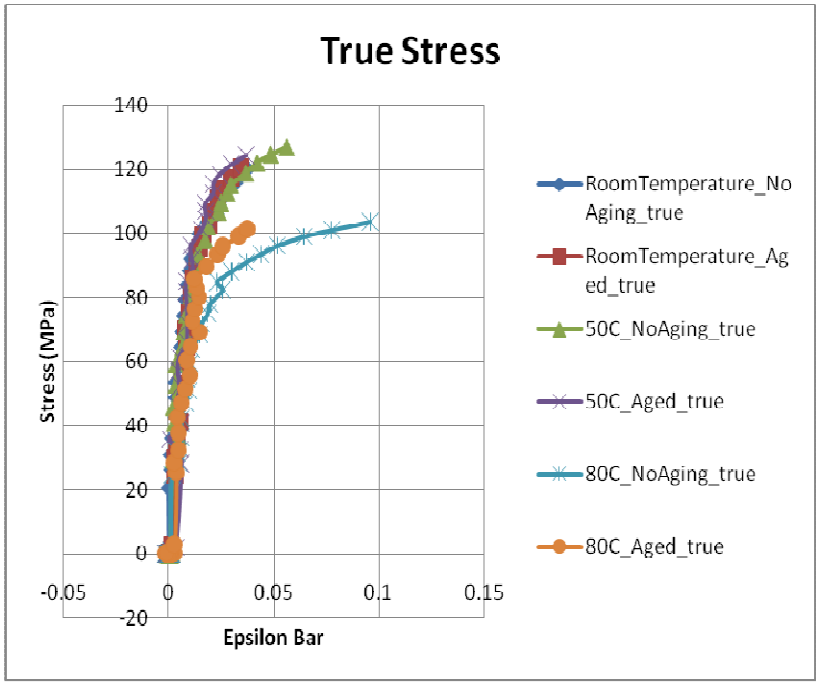

Fig. D-89

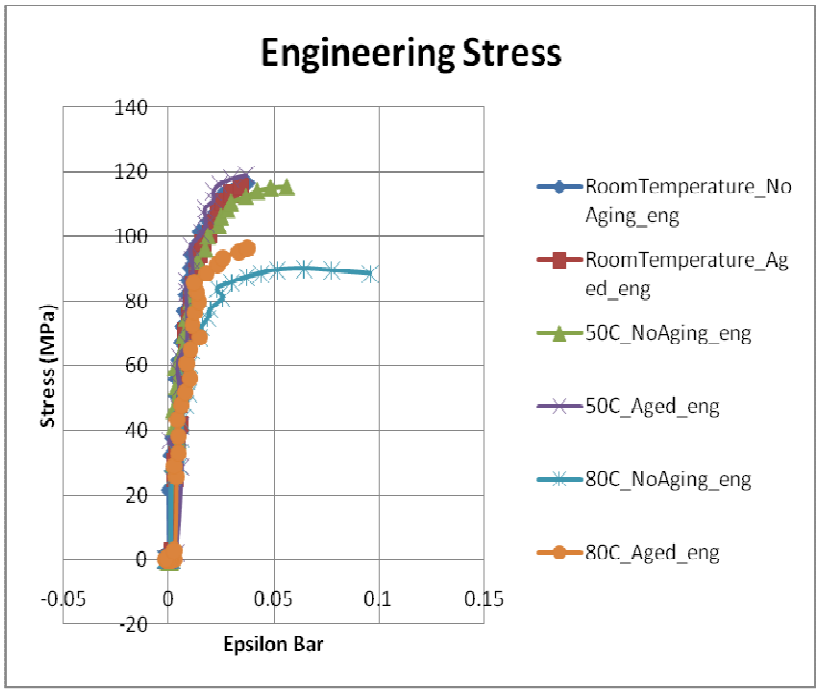

Fig. D-90

b. Displacement Rate 1e-3 in/s

Fig. D-91

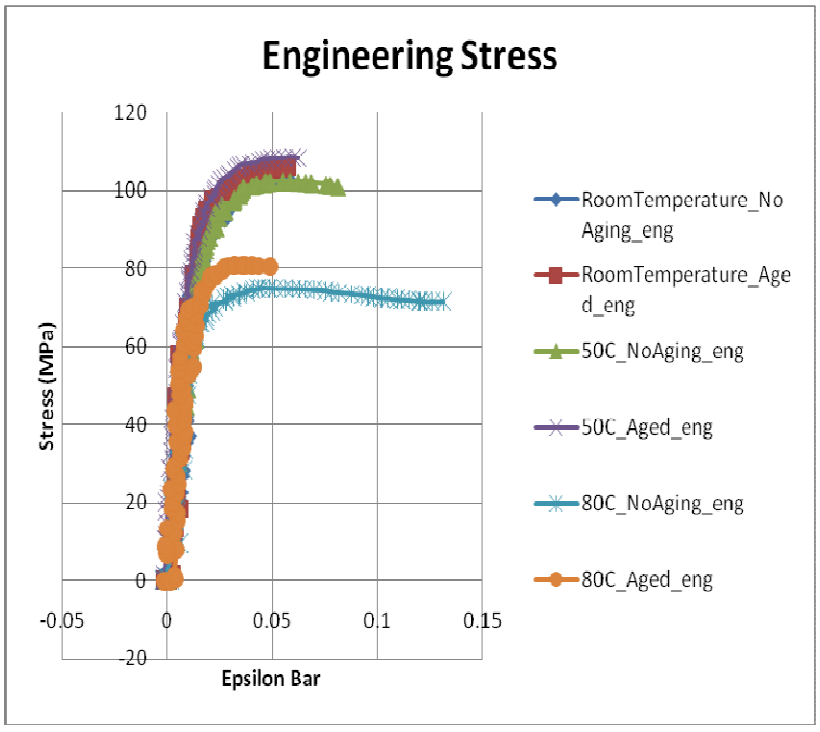

Fig. D-92

II. Notch Radius 0.0614 in.
    a. Displacement Rate 1e-1 in/s

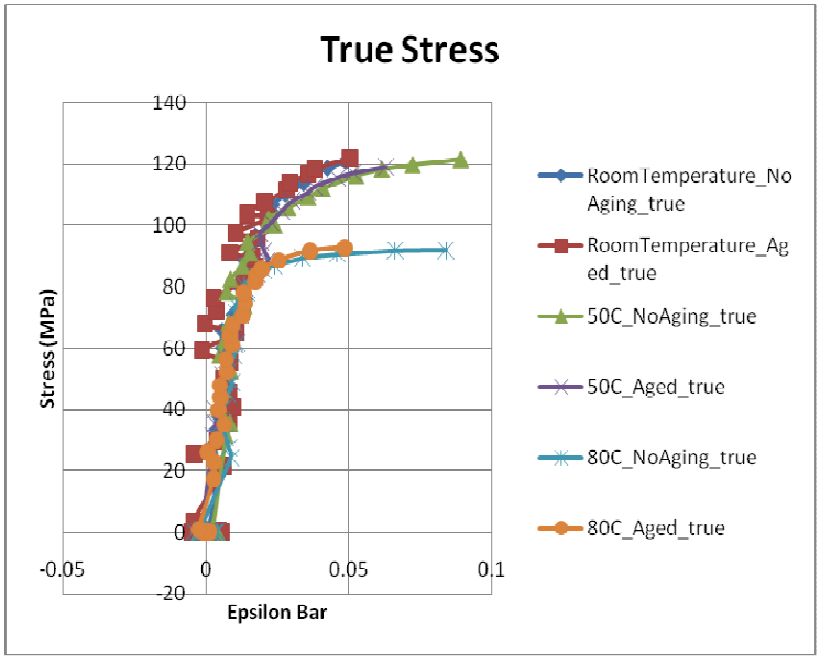

Fig. D-93

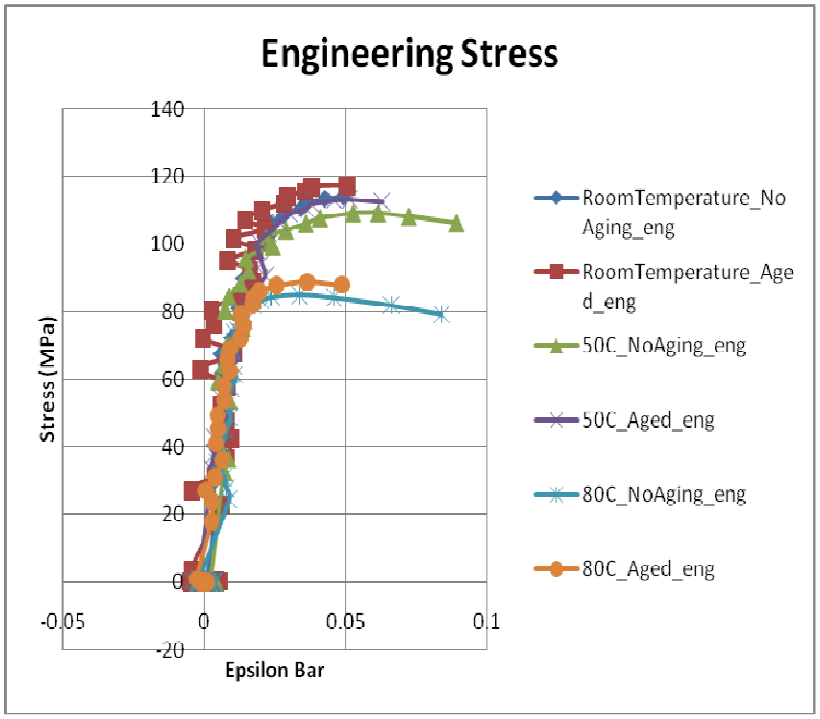

Fig. D-94

b. Displacement Rate 1e-3 in/s

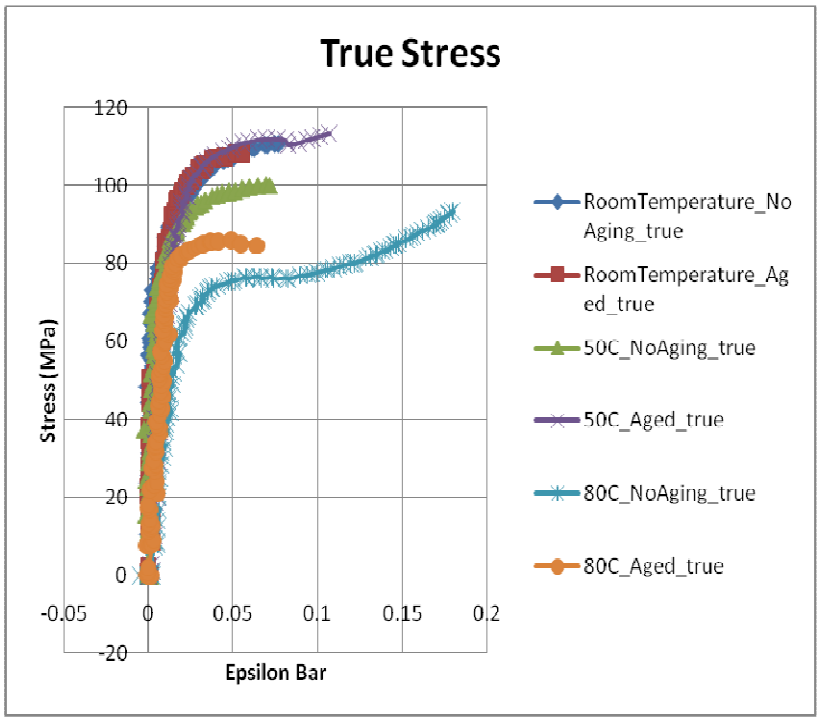

Fig. D-95

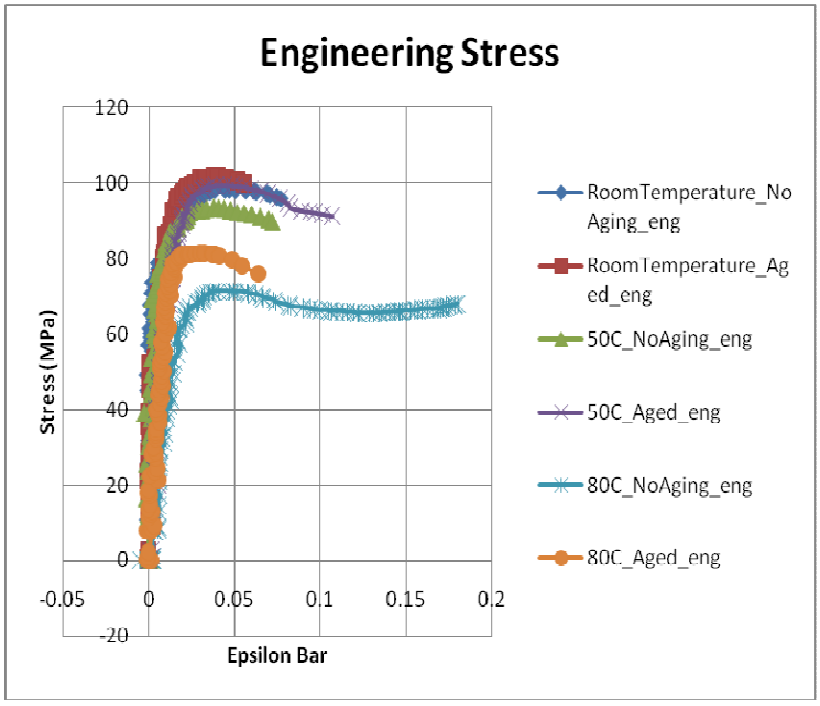

Fig. D-96

III. Notch Radius 0.1535 in.

a. Displacement Rate 1e-1 in/s

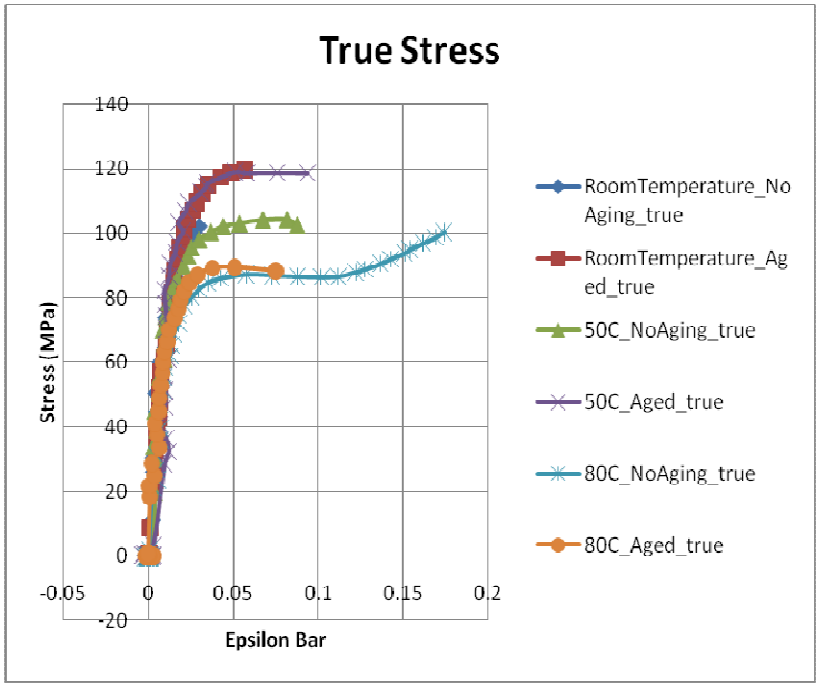

Fig. D-97

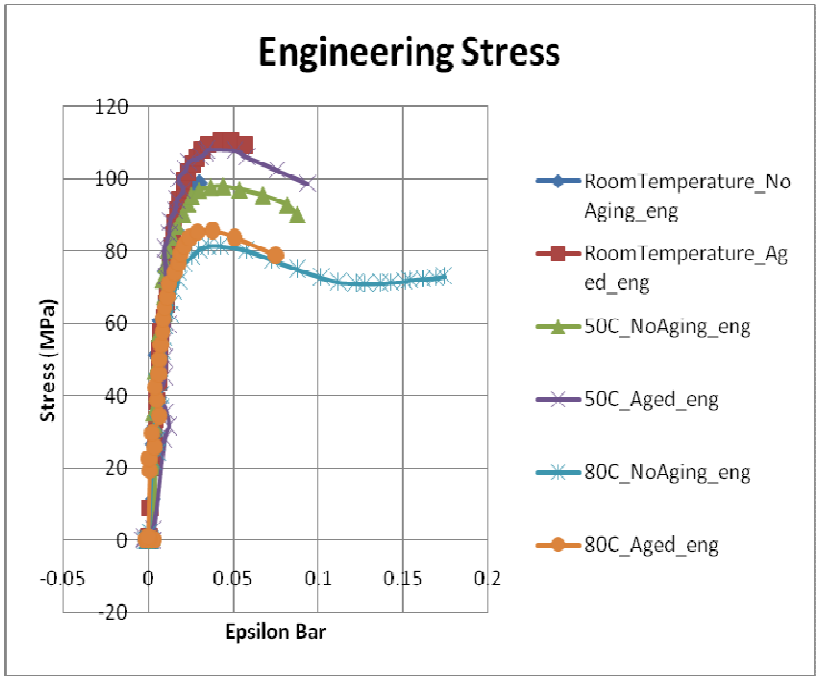

Fig. D-98

b. Displacement Rate 1e-3 in/s

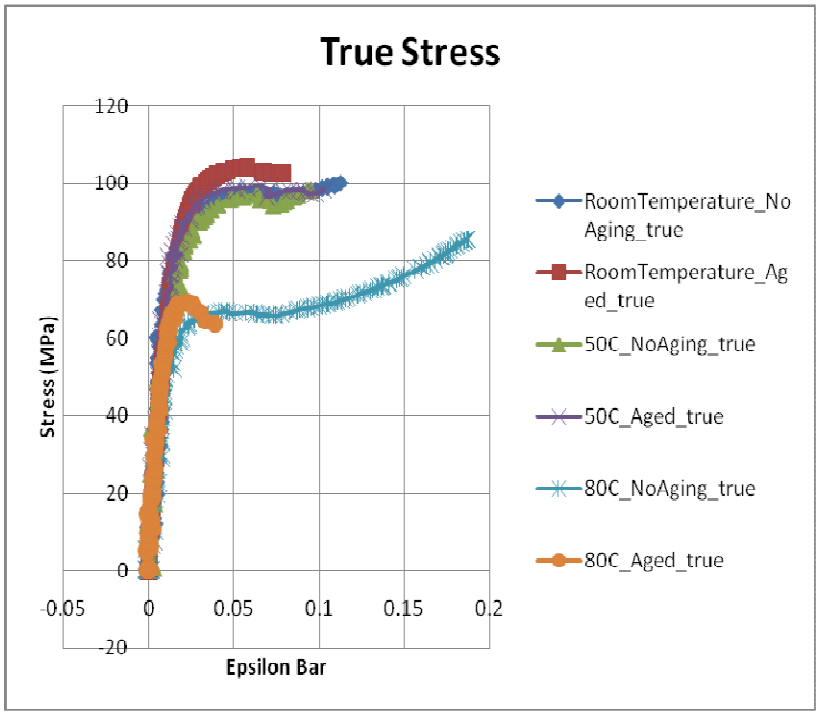

Fig. D-99

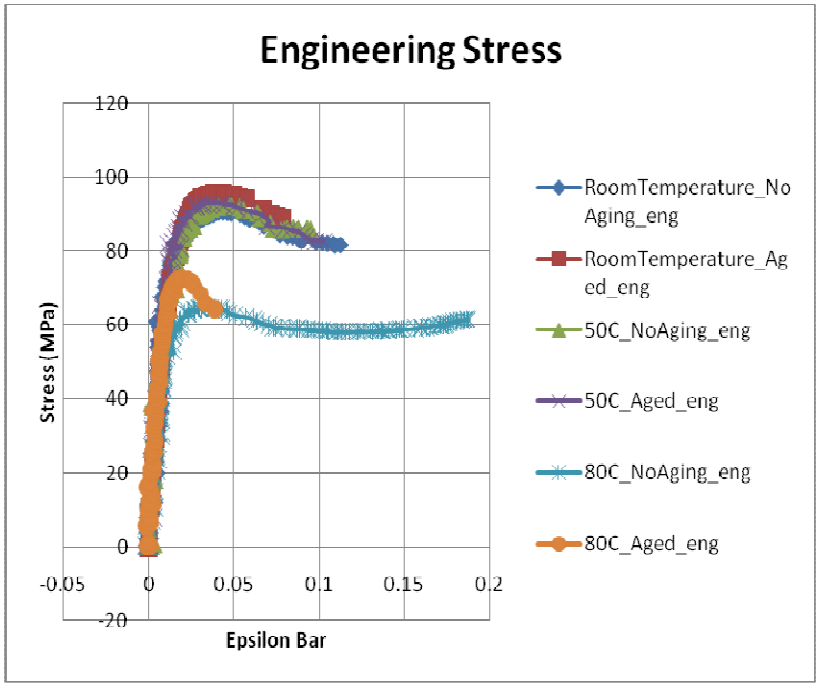

Fig. D-100

APPENDIX E

DISPLACEMENT RATE COMPARISON DATA

I. Room Temperature
   a. No Aging
      i. Notch Radius 0.0307 in.

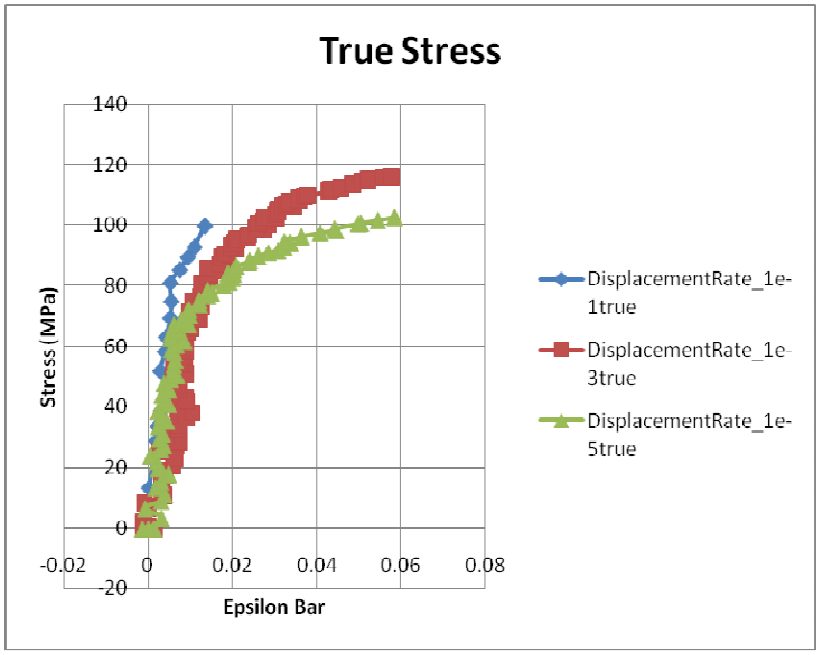

Fig. E-101

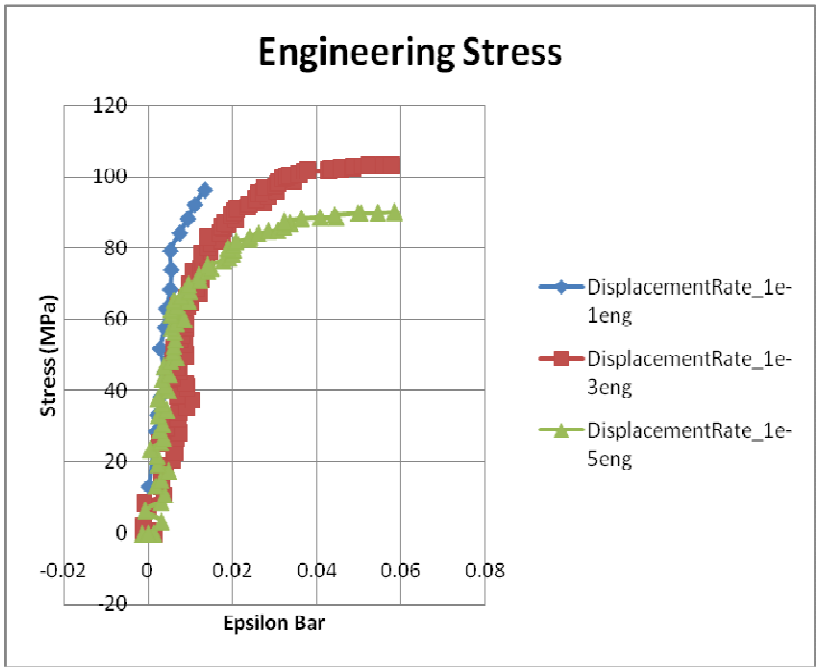

Fig. E-102

ii. Notch Radius 0.0614 in.

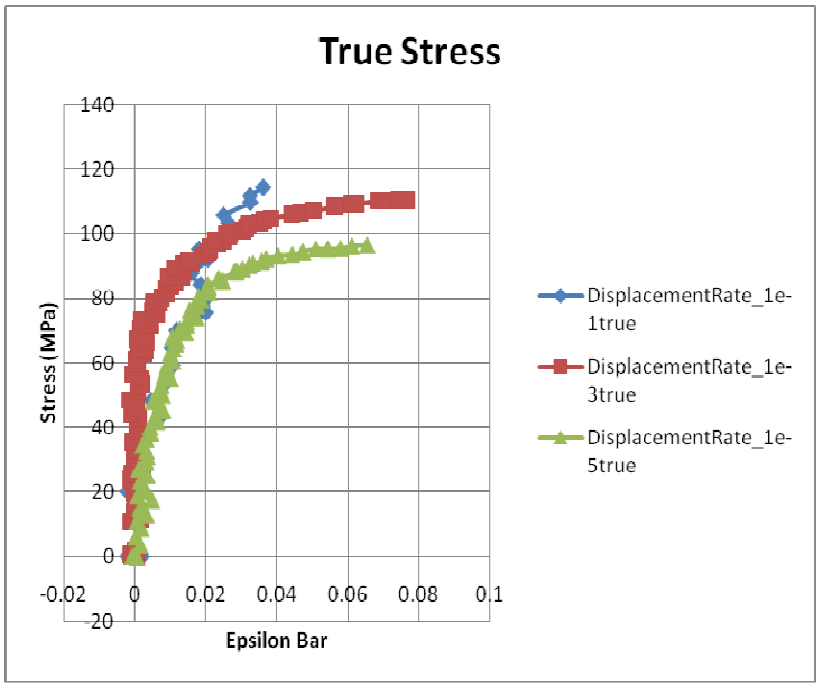

Fig. E-103

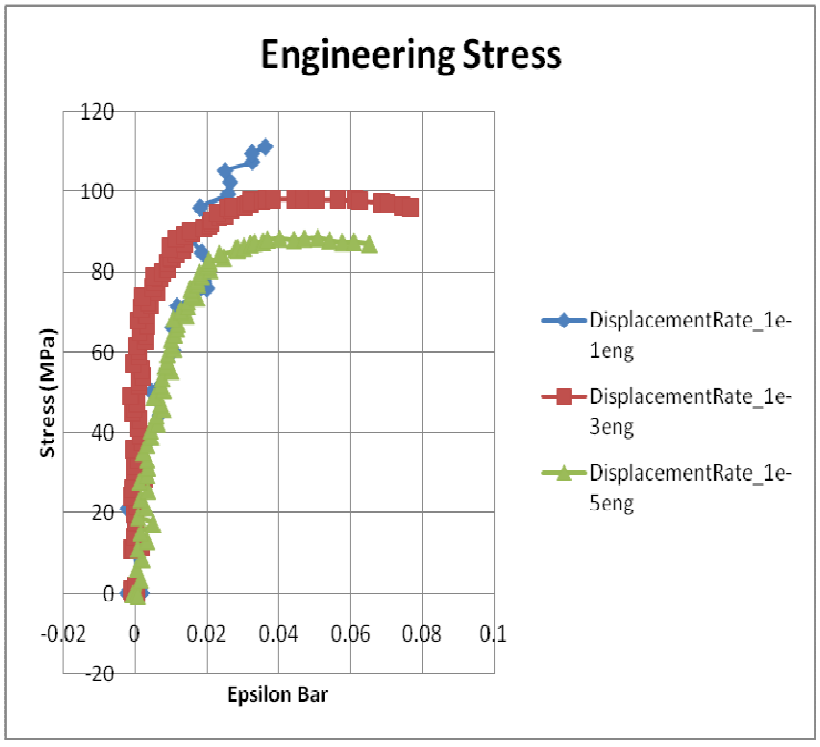

Fig. E-104

iii. Notch Radius 0.1535 in.

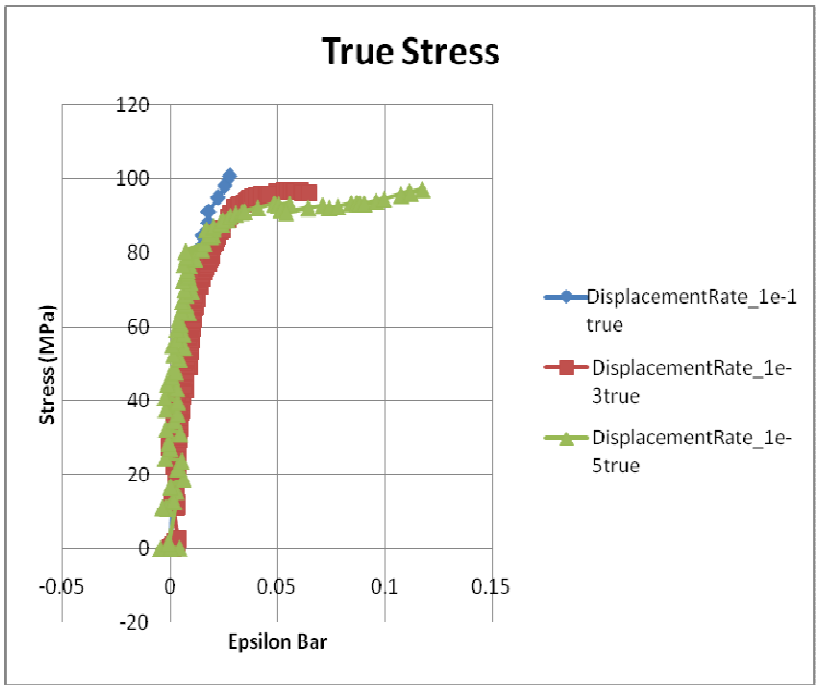

Fig. E-105

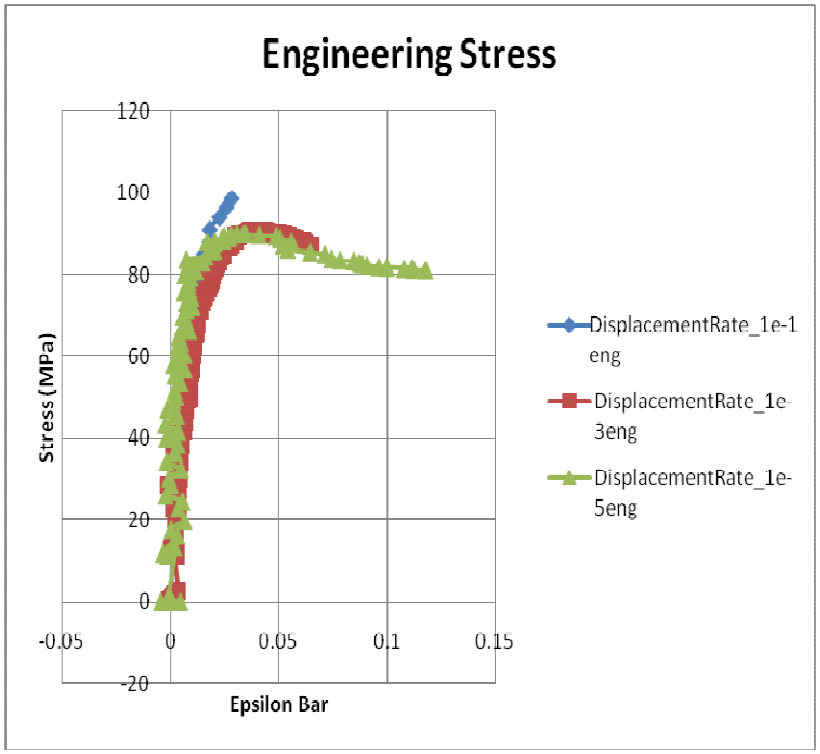

Fig. E-106

b. Aged

i. Notch Radius 0.0307 in.

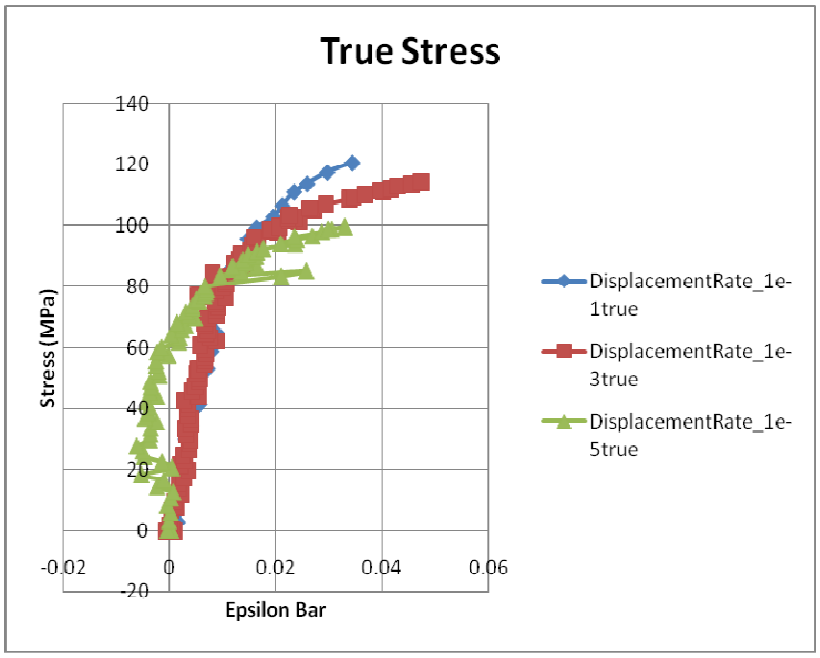

Fig. E-107

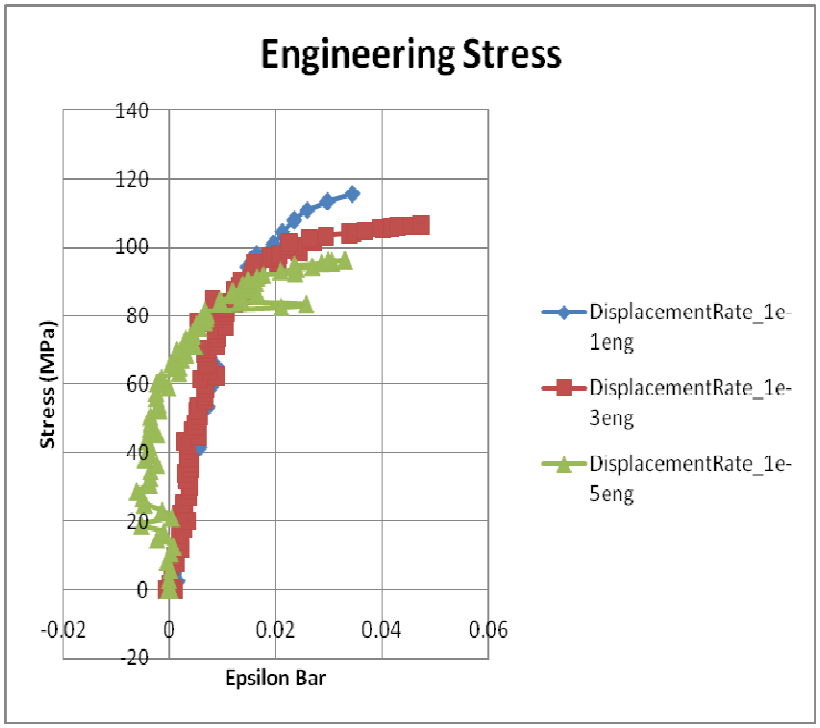

Fig. E-108

ii. Notch Radius 0.0614 in.

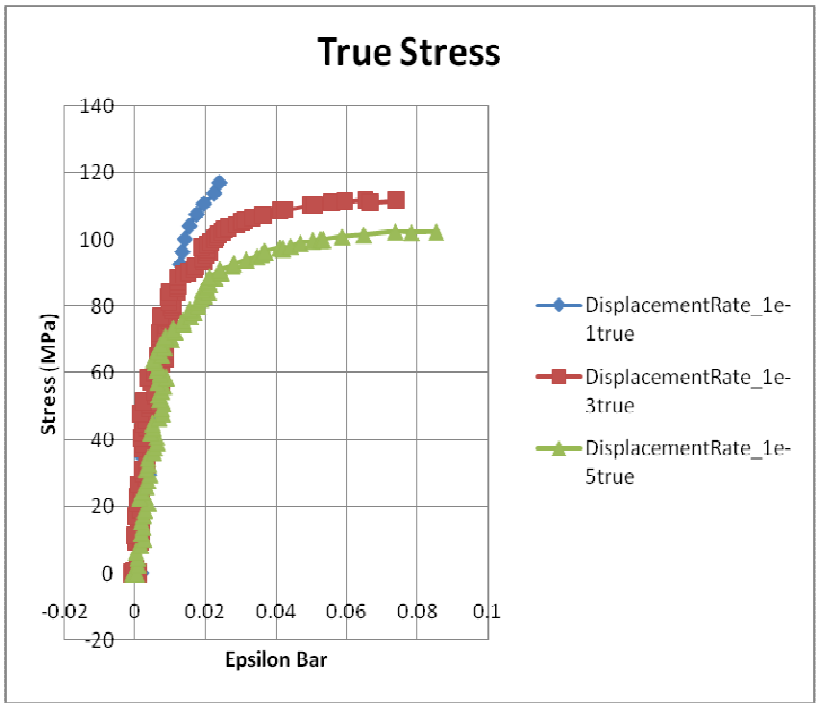

Fig. E-109

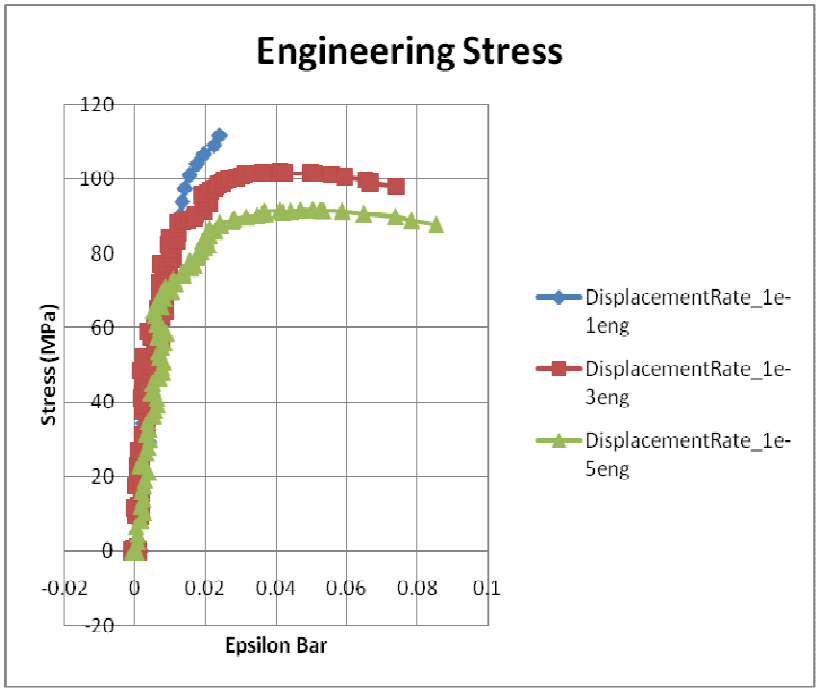

Fig. E-110

iii. Notch Radius 0.1535 in.

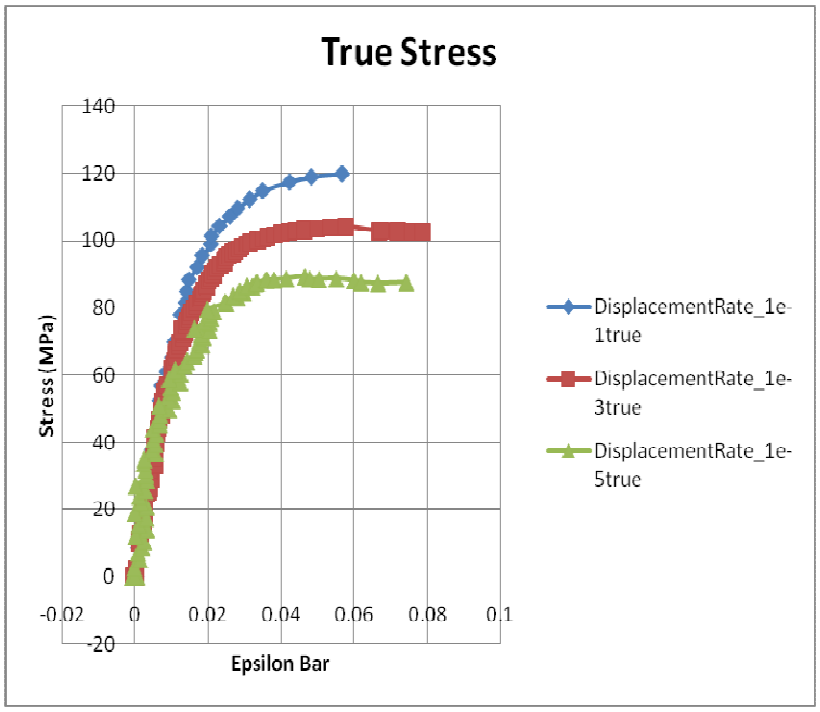

Fig. E-111

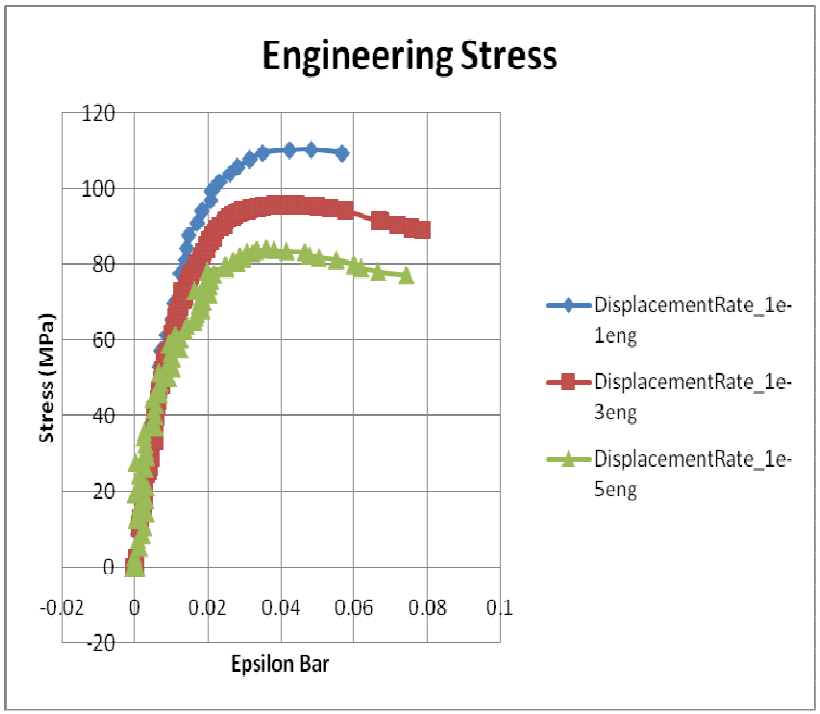

Fig. E-112

II. 50 C
   a. No Aging
      i. Notch Radius 0.0307 in.

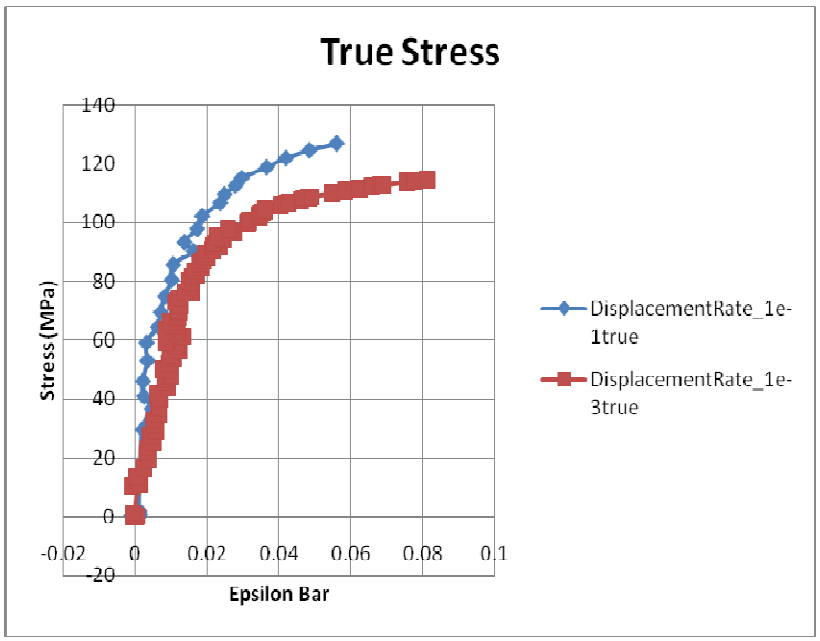

Fig. E-113

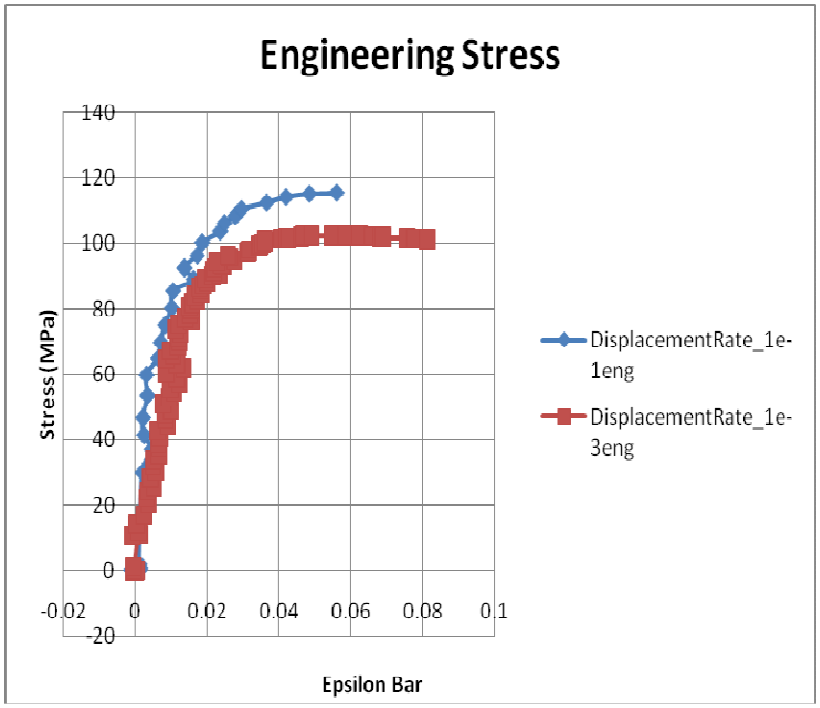

Fig. E-114

ii. Notch Radius 0.0614 in.

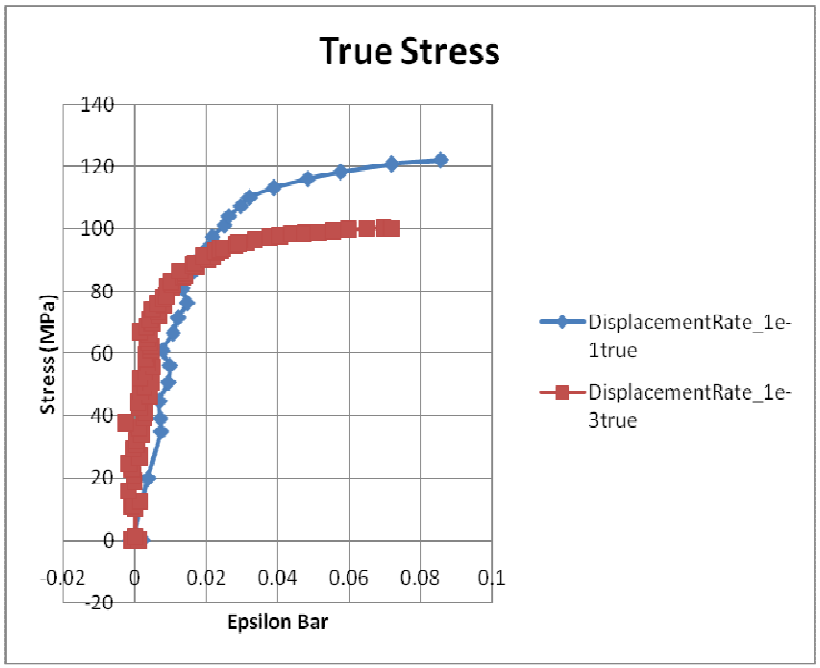

Fig. E-115

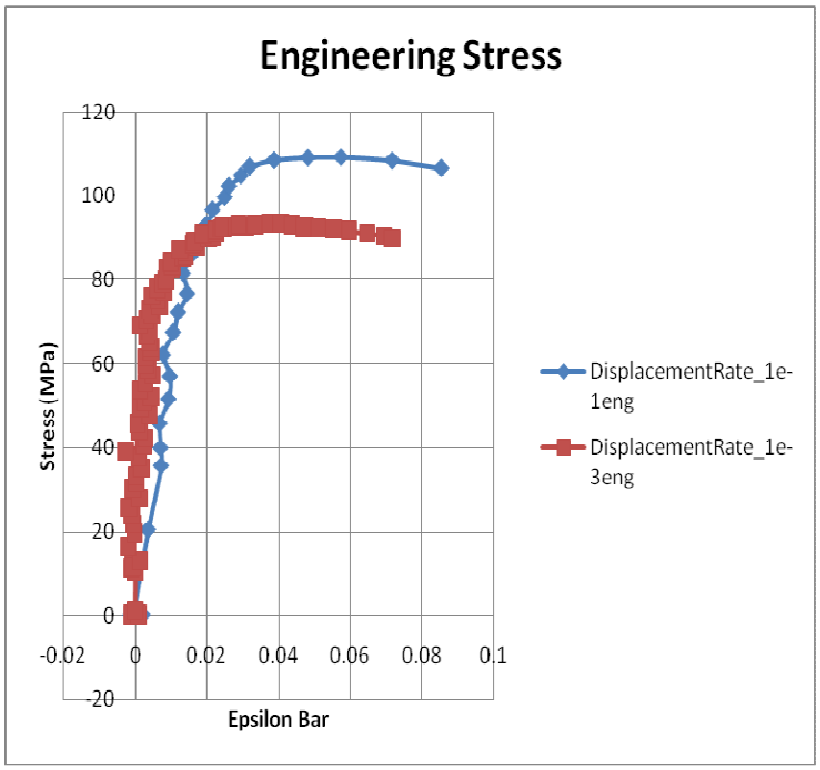

Fig. E-116

iii. Notch Radius 0.1535 in.

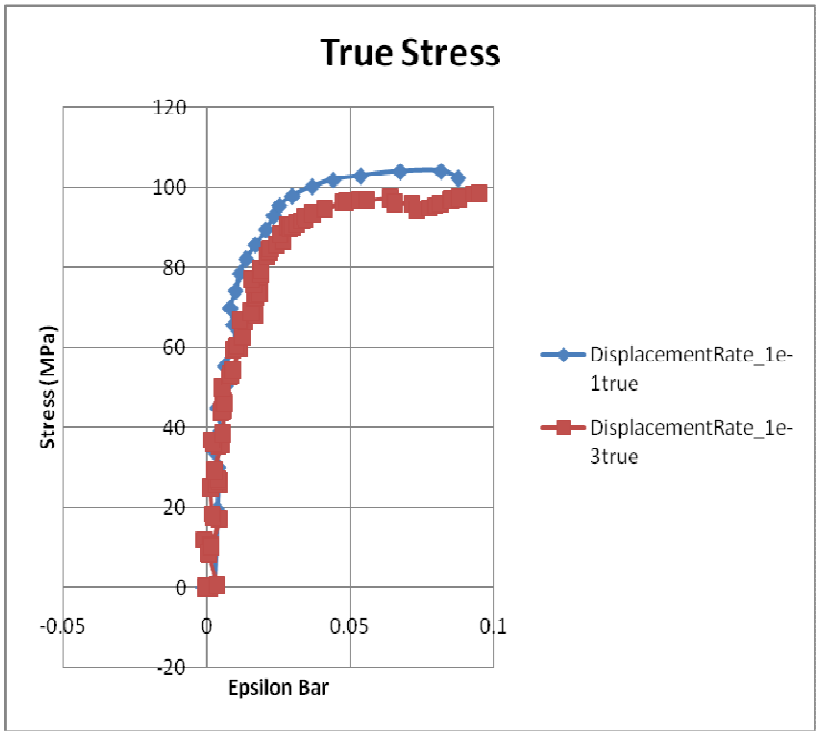

Fig. E-117

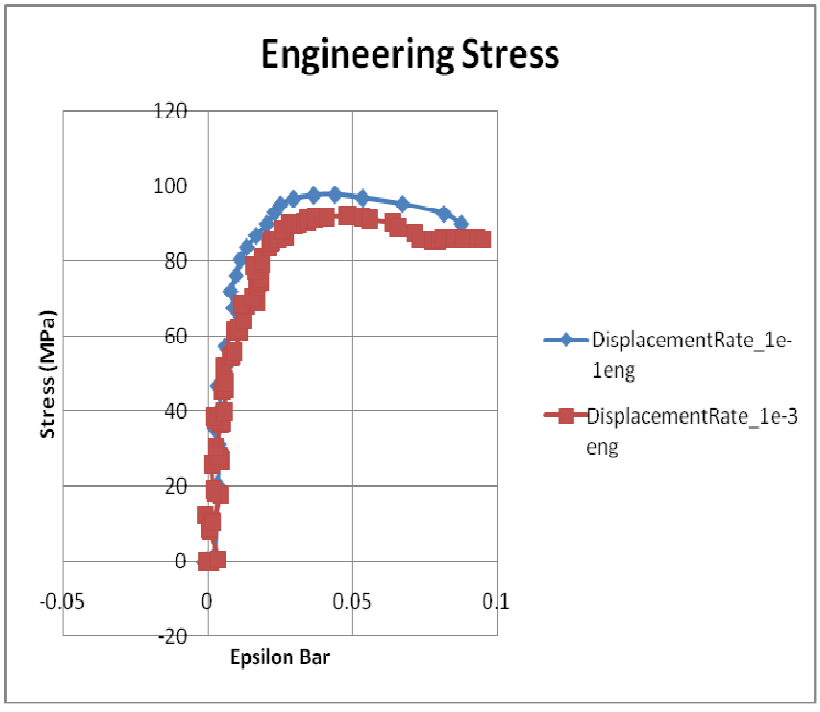

Fig. E-118

b. Aged

i. Notch Radius 0.0307 in.

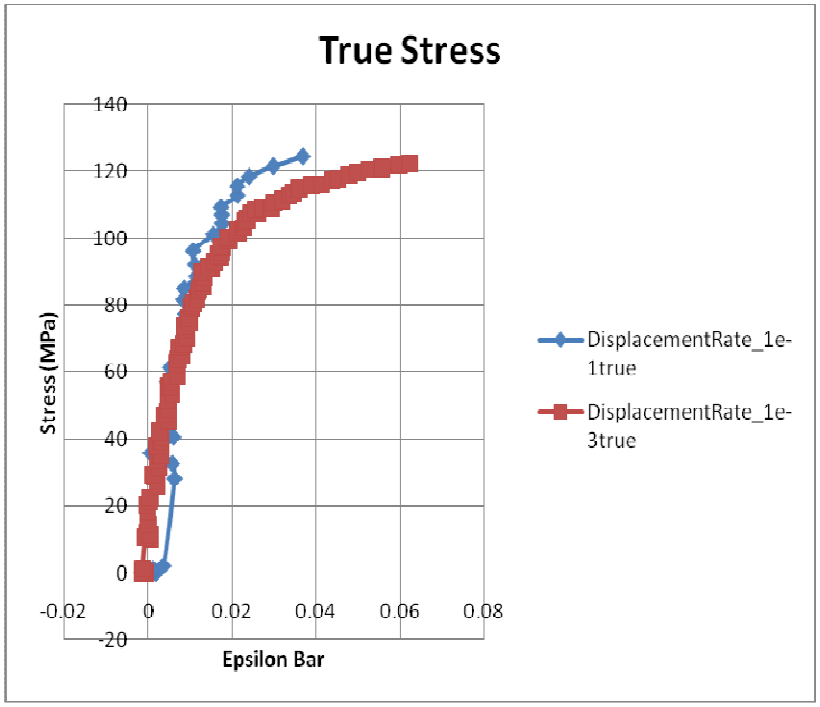

Fig. E-119

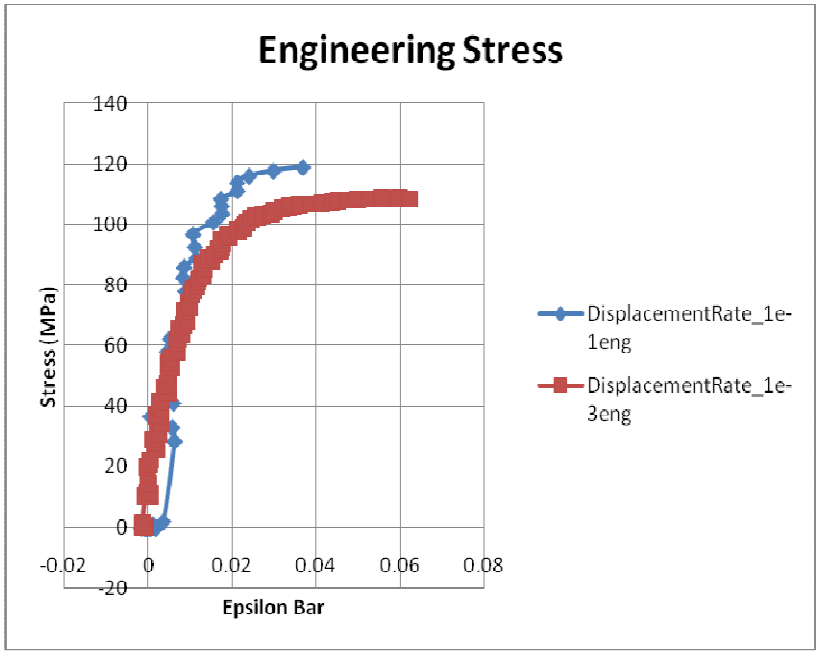

Fig. E-120

ii. Notch Radius 0.0614 in.

Fig. E-121

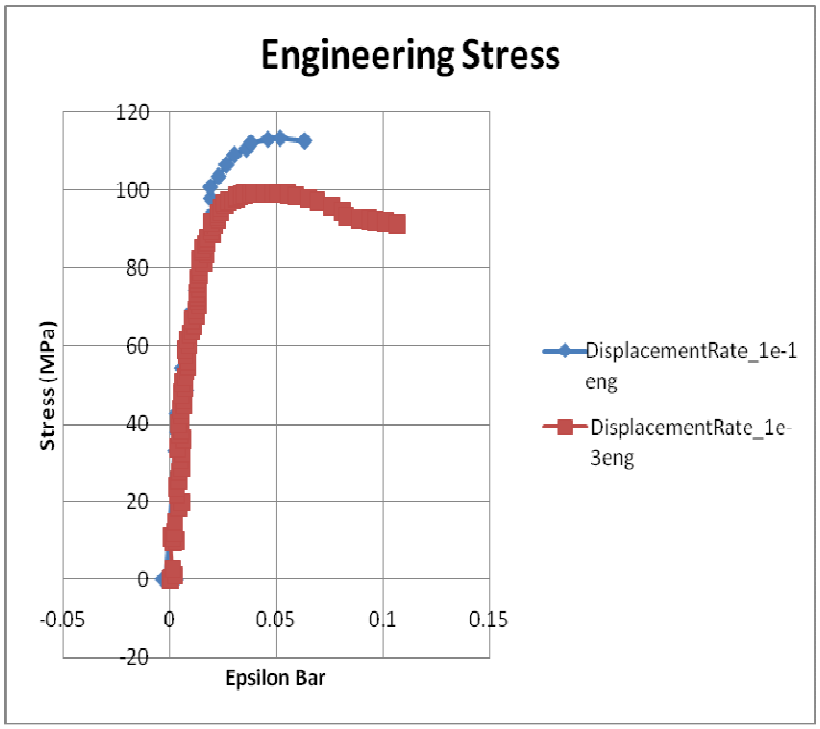

Fig. E-122

iii. Notch Radius 0.1535 in.

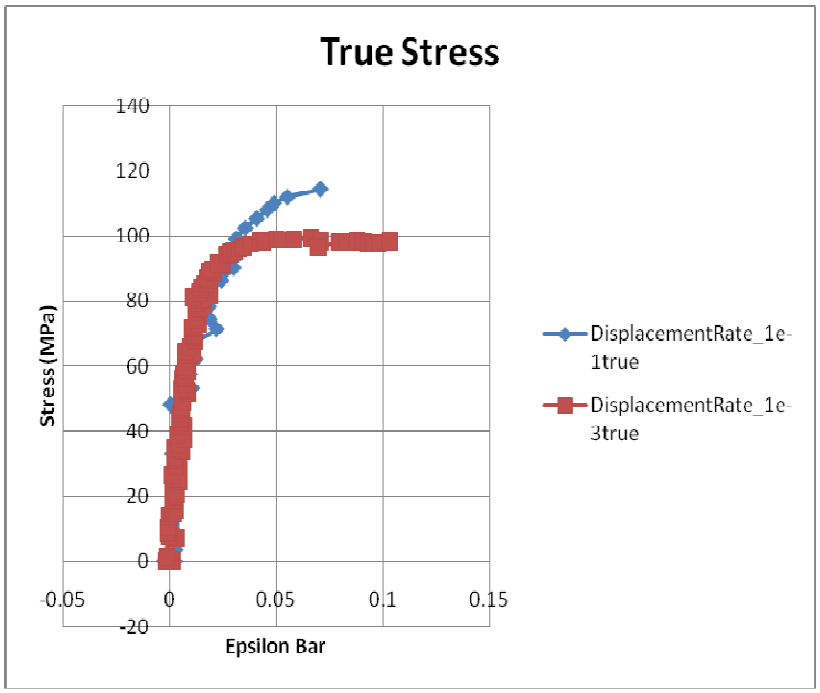

Fig. E-123

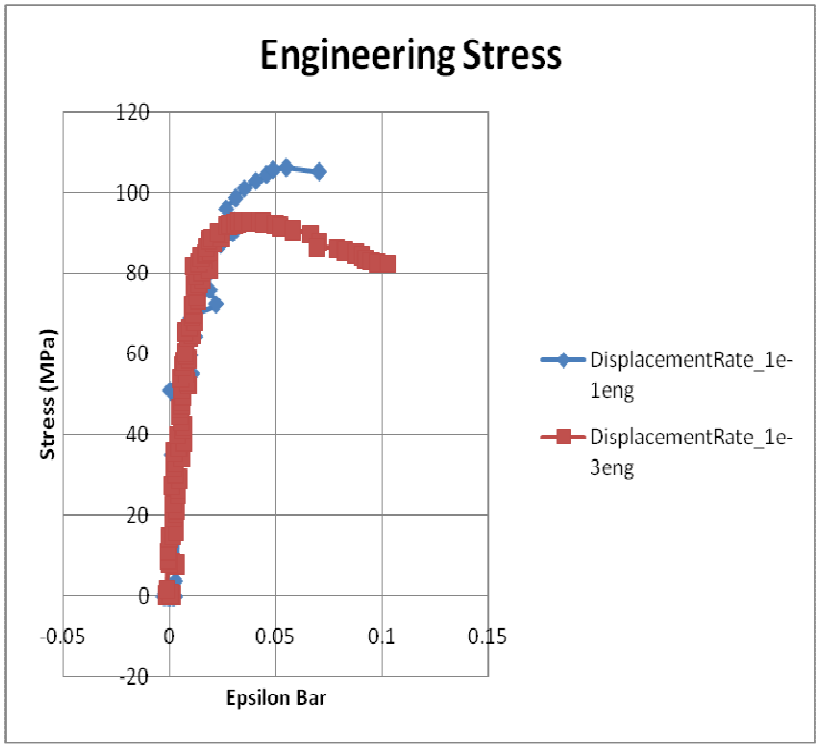

Fig. E-124

III. 80 C

a. No Aging

i. Notch Radius 0.0307 in.

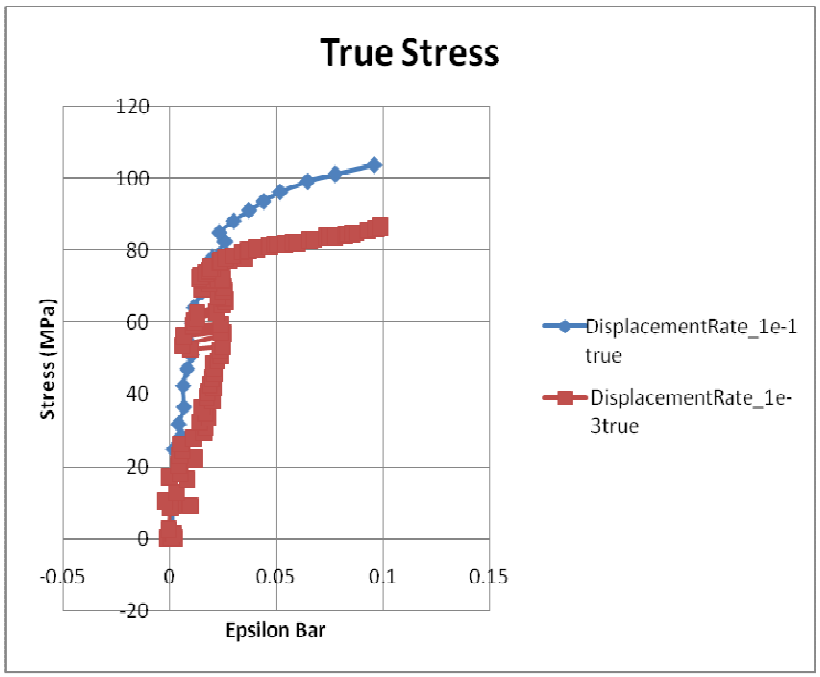

Fig. E-125

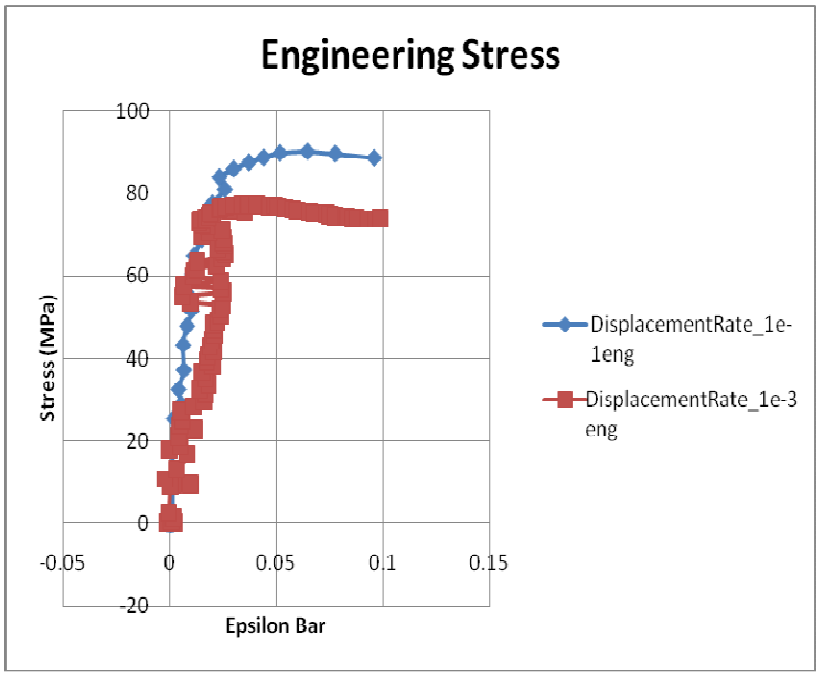

Fig. E-126

ii. Notch Radius 0.0614 in.

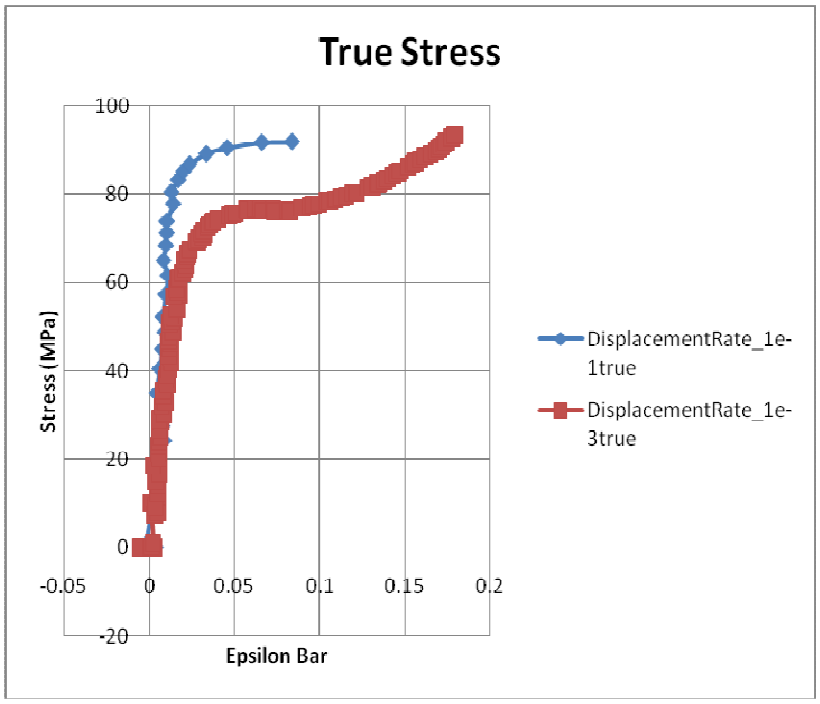

Fig. E-127

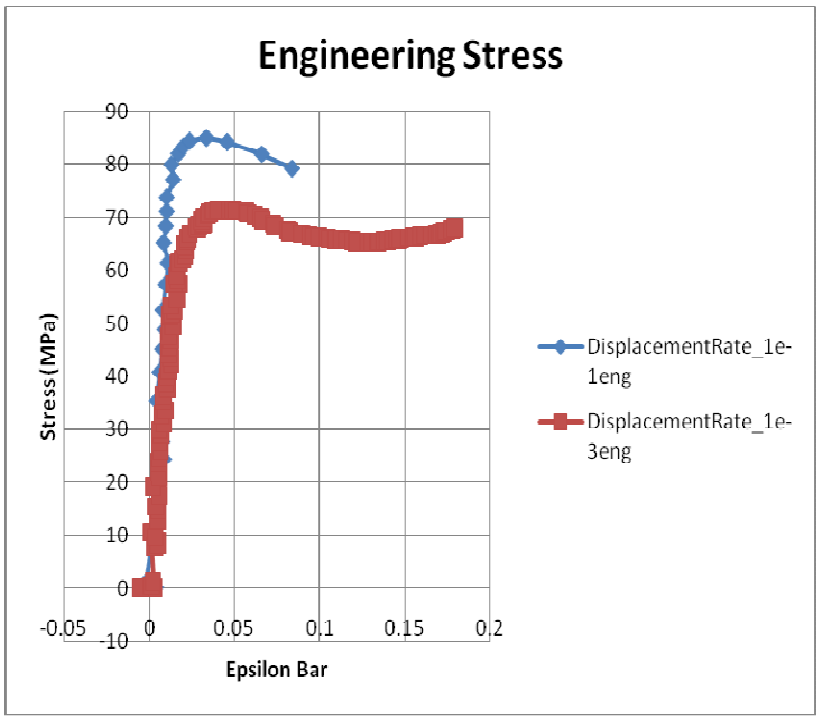

Fig. E-128

iii. Notch Radius 0.1535 in.

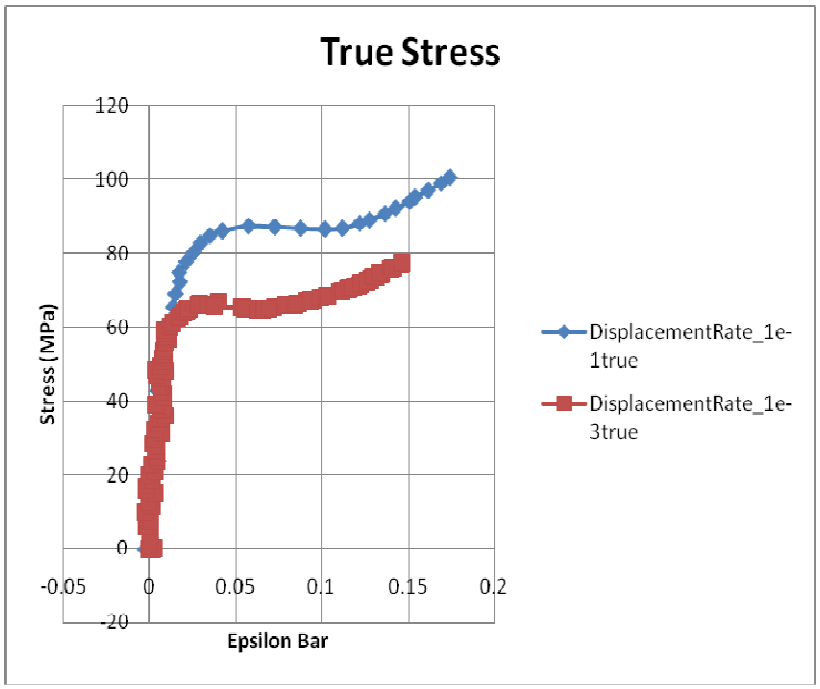

Fig. E-129

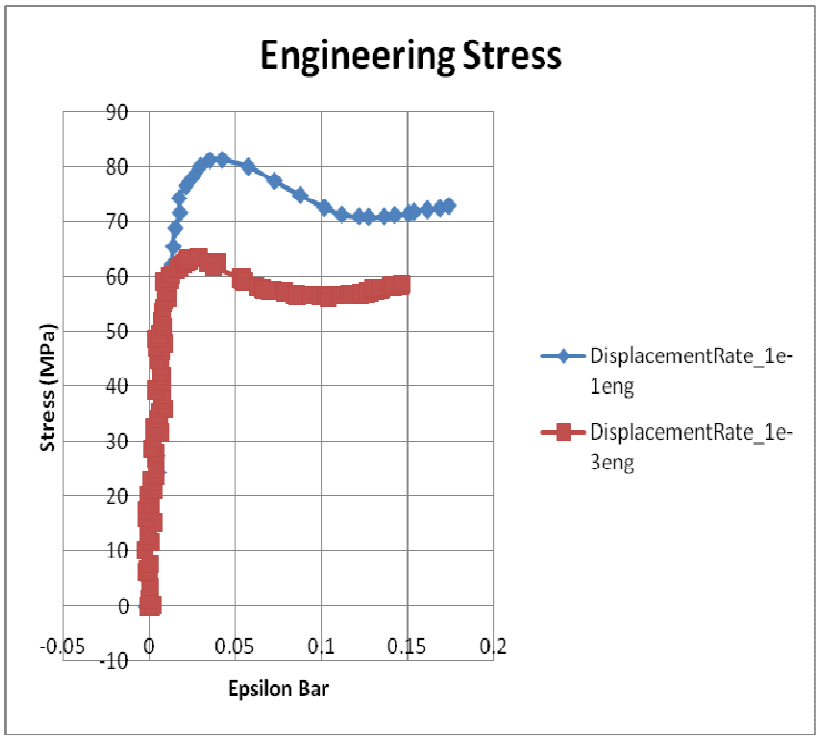

Fig. E-130

b. Aged

i. Notch Radius 0.0307 in.

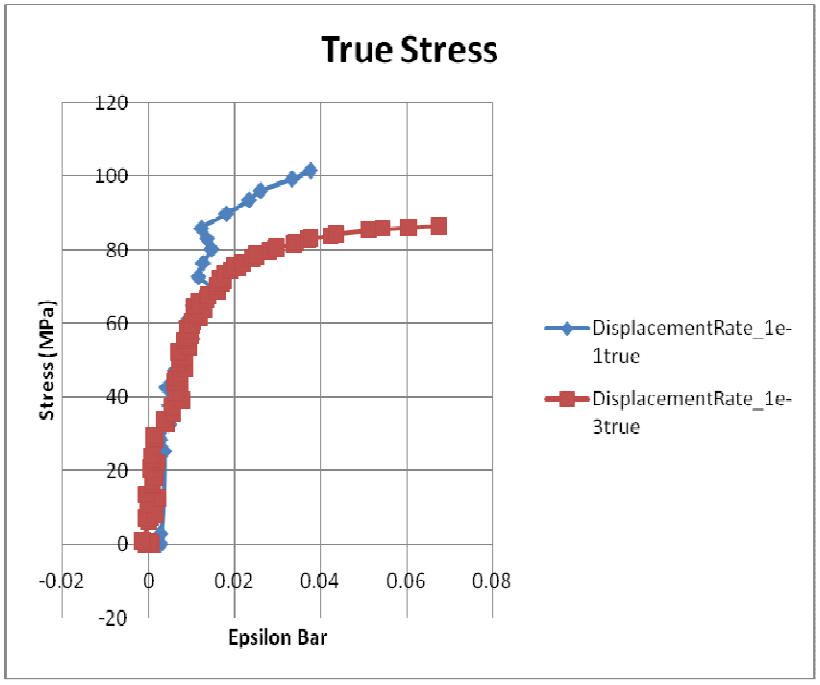

Fig. E-131

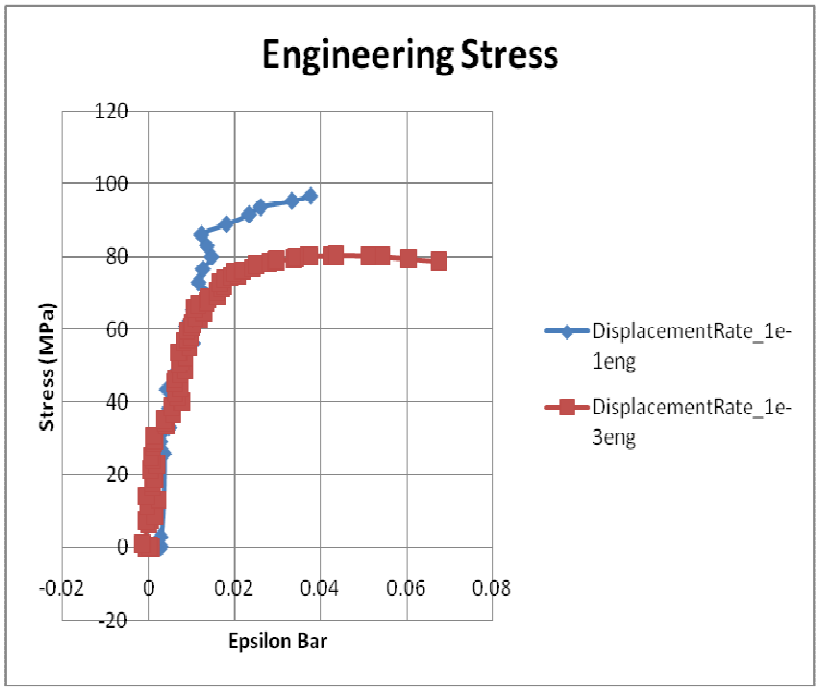

Fig. E-132

ii. Notch Radius 0.0614 in.

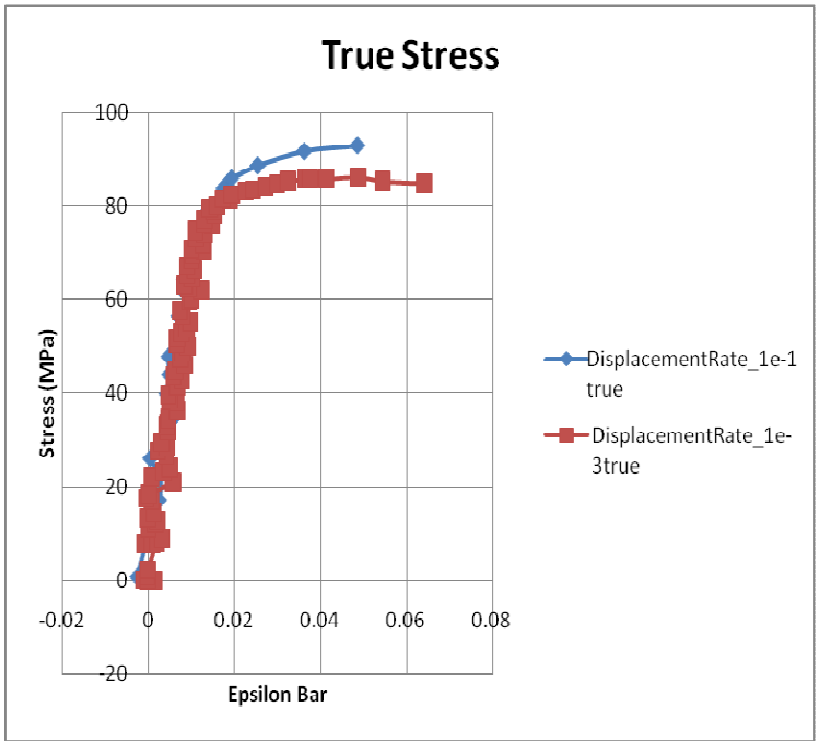

Fig. E-133

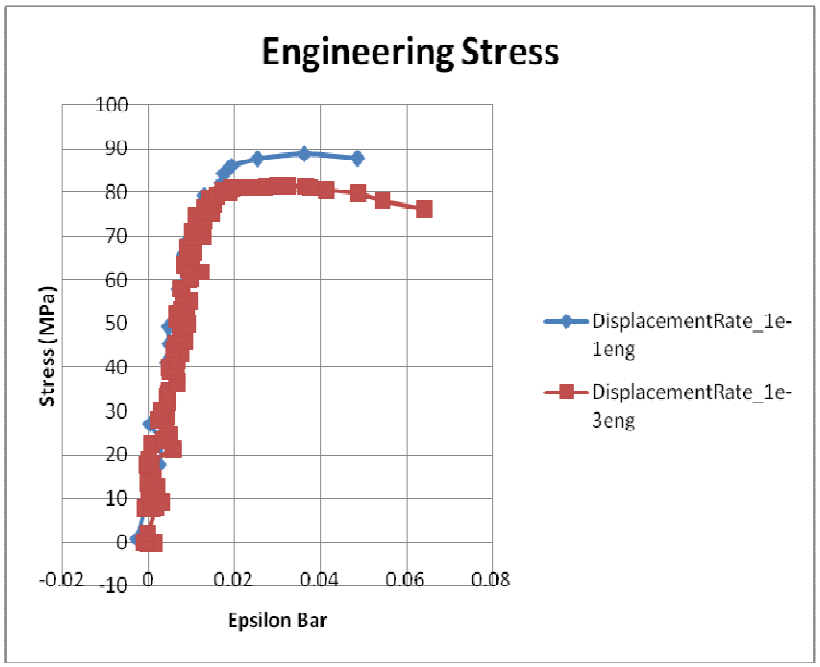

Fig. E-134

iii. Notch Radius 0.1535 in.

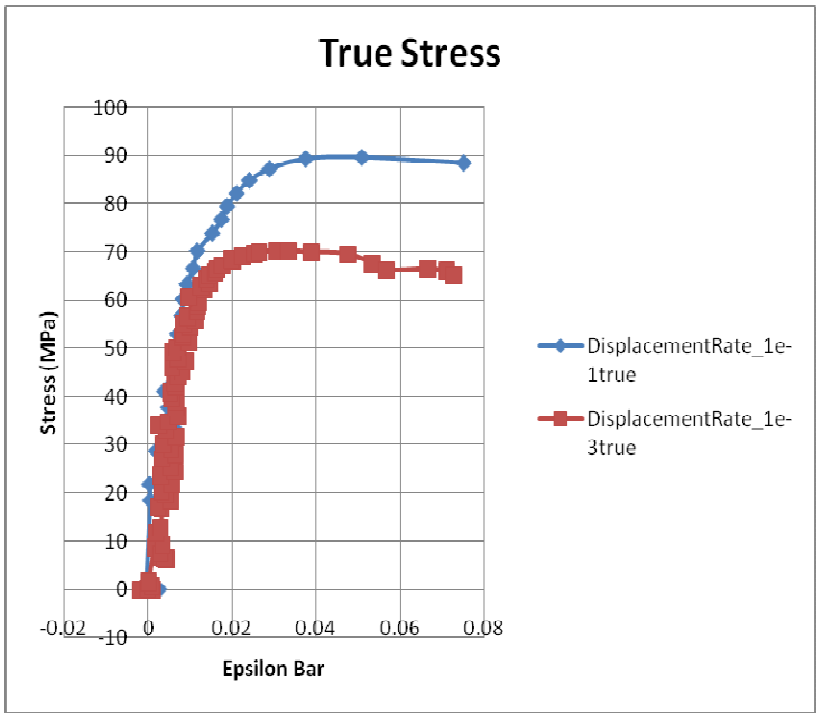

Fig. E-135

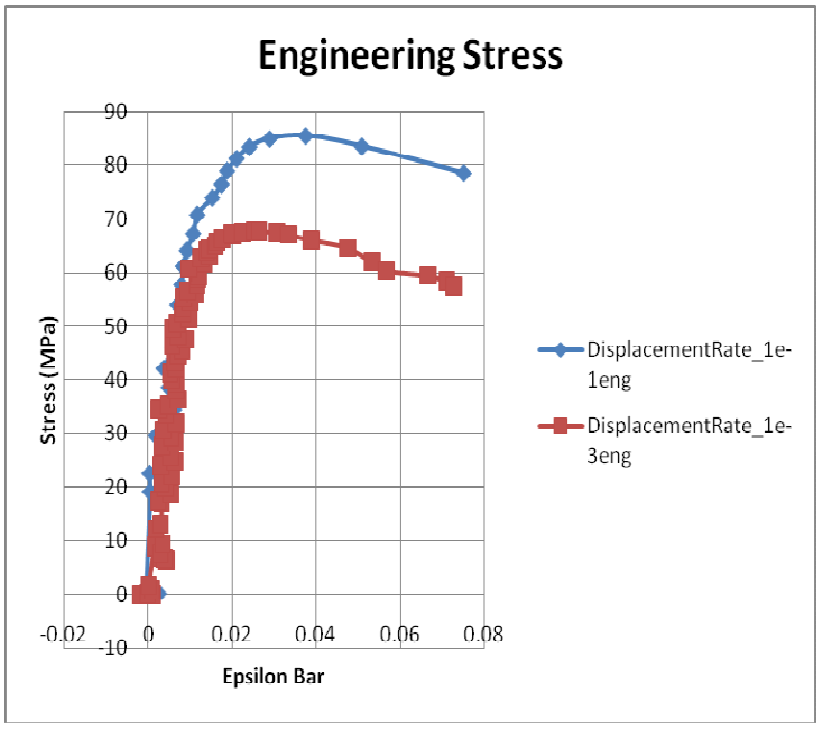

Fig. E-136

CONTACT INFORMATION

Name:	Brad Burgess
Professional Address:	c/o Dr. Amine Benzerga Department of Aerospace Engineering HRBB 702 Texas A&M University College Station, TX 77843
Email Address:	andromeda121885@tamu.edu
Education:	B.S., Aerospace Engineering, Texas A&M University, December 2009 Undergraduate Research Scholar Sigma Gamma Tau Phi Eta Sigma